International Journal of Digital Earth

ISSN: (Print) (Online) Journal homepage: www.tandfonline.com/journals/tjde20

Advances on the Global Human Settlement Layer by joint assessment of Earth Observation and population survey data

Martino Pesaresi, Marcello Schiavina, Panagiotis Politis, Sergio Freire, Katarzyna Krasnodębska, Johannes H. Uhl, Alessandra Carioli, Christina Corbane, Lewis Dijkstra, Pietro Florio, Hannah K. Friedrich, Jing Gao, Stefan Leyk, Linlin Lu, Luca Maffenini, Ines Mari-Rivero, Michele Melchiorri, Vasileios Syrris, Jamon Van Den Hoek & Thomas Kemper

To cite this article: Martino Pesaresi, Marcello Schiavina, Panagiotis Politis, Sergio Freire, Katarzyna Krasnodębska, Johannes H. Uhl, Alessandra Carioli, Christina Corbane, Lewis Dijkstra, Pietro Florio, Hannah K. Friedrich, Jing Gao, Stefan Leyk, Linlin Lu, Luca Maffenini, Ines Mari-Rivero, Michele Melchiorri, Vasileios Syrris, Jamon Van Den Hoek & Thomas Kemper (2024) Advances on the Global Human Settlement Layer by joint assessment of Earth Observation and population survey data, International Journal of Digital Earth, 17:1, 2390454, DOI: 10.1080/17538947.2024.2390454

To link to this article: https://doi.org/10.1080/17538947.2024.2390454

INTERNATIONAL JOURNAL OF DIGITAL EARTH
2024, VOL. 17, NO. 1, 2390454
https://doi.org/10.1080/17538947.2024.2390454

Advances on the Global Human Settlement Layer by joint assessment of Earth Observation and population survey data

Martino Pesaresi [a], Marcello Schiavina [b], Panagiotis Politis [c], Sergio Freire [a], Katarzyna Krasnodębska [d], Johannes H. Uhl [a], Alessandra Carioli [a], Christina Corbane [a], Lewis Dijkstra [e], Pietro Florio [a], Hannah K. Friedrich [f], Jing Gao [g], Stefan Leyk [h], Linlin Lu [i,j], Luca Maffenini[k], Ines Mari-Rivero [l], Michele Melchiorri [a], Vasileios Syrris [m]*, Jamon Van Den Hoek [n] and Thomas Kemper [a]

[a]Directorate for Societal Resilience and Security, European Commission, Joint Research Centre (JRC), Ispra, Italy; [b]NTT DATA, Brussels, Belgium; [c]European Dynamics Belgium S.A., Brussels, Belgium; [d]Institute of Geography and Spatial Organization, Polish Academy of Sciences, Warsaw, Poland; [e]Directorate for Fair and Sustainable Economy, European Commission Joint Research Centre (JRC), Ispra, Italy; [f]School of Geography, Development & Environment, University of Arizona, Tucson, AZ, USA; [g]Department of Geography and Spatial Sciences, & Data Science Institute, University of Delaware, Newark, DE, USA; [h]Department of Geography, University of Colorado Boulder, Boulder, CO, USA; [i]International Research Center of Big Data for Sustainable Development Goals, Beijing, People's Republic of China; [j]Key Laboratory of Digital Earth Science, Aerospace Information Research Institute, Chinese Academy of Sciences, Beijing, People's Republic of China; [k]UniSystems Luxembourg Sàrl, Bertrange, Luxembourg; [l]FINCONS SPA, Vimercate, Italy; [m]European Union Intellectual Property Office (EUIPO), Alicante, Spain; [n]College of Earth, Ocean, and Atmospheric Sciences, Oregon State University, Corvallis, OR, USA

ABSTRACT

The Global Human Settlement Layer (GHSL) project fosters an enhanced, public understanding of the human presence on Earth. A decade after its inception in the Digital Earth 2020 vision, GHSL is an established project of the European Commission's Joint Research Centre and an integral part of the Copernicus Emergency Management Service. The 2023 GHSL edition, a result of rigorous research on Earth Observation data and population censuses, contributes significantly to understanding worldwide human settlements. It introduces new elements like 10-m-resolution, sub-pixel estimation of built-up surfaces, global building height and volume estimates, and a classification of residential and non-residential areas, improving population density grids. This paper evaluates the key components of the GHSL, including the Symbolic Machine Learning approach, using novel reference data. These data enable a comparative assessment of GHSL model predictions on the evolution of built-up surface, building heights, and resident population. Empirical evidence suggests that GHSL estimates are the most accurate in the public domain today, e.g. achieving an IoU of 0.98 for the water class, 0.92 for the built-up class, and 0.8 for the non-residential class at 10 m resolution. At 100 m resolution, we find that the MAE of built-up surface

ARTICLE HISTORY
Received 18 March 2024
Accepted 5 August 2024

KEYWORDS
GHSL; geospatial XAI; built-up surface; population grids; degree of urbanization; building height; built-up volume; urban land use; settlement morphology; built typology; Sentinel-2; Copernicus

CONTACT Martino Pesaresi Martino.PESARESI@ec.europa.eu Directorate for Societal Resilience and Security, European Commission, Joint Research Centre (JRC), Ispra, Italy

*The views in the text are of the author only and do not represent the position of the EUIPO in the matter.

Supplemental data for this article can be accessed online at https://doi.org/10.1080/17538947.2024.2390454.

This article was originally published with errors, which have now been corrected in the online version. Please see Correction (http://dx.doi.org/10.1080/17538947.2024.2404284)

estimates corresponds to 6% of the grid cell area, the MAE for the building height estimates is 2.27 m, and we find a total allocation accuracy of 83% for resident population. This paper consolidates the theoretical foundation of the GHSL and highlights its innovative features for transparent Artificial Intelligence, facilitating international decision-making processes.

1. Introduction

> … The year is 2020. A global symbolic representation of the built environment is available and integrated in the DE. The global human settlement layer (GHSL) is a multi-scale volumetric information layer describing artificial spaces where people live, work and enjoy life … (Craglia et al. 2012)

Human settlements, the epicenters of societal development, require innovative paradigms for comprehensive mapping. More than a decade after the 'Digital Earth 2020' vision (Craglia et al. 2012) anticipated the GHSL concept, we present the 2023 GHSL edition, a result of combined Earth Observation (EO) and population-census data analysis, aiming to map global human settlements' attributes (Figure 1). This manuscript reinforces the theoretical basis of the GHSL processing framework, highlights its innovative features, and summarizes key findings from the latest GHSL data release.

Section 2 consolidates the GHSL theoretical background, explaining unique methodological choices, such as the need for transparent AI in public decision-making. Section 3 overviews the data products, crucial for understanding novelty of the GHSL production. Section 4 details the materials and methods supporting the GHSL production. Section 5 presents the GHSL model predictions' validation and comparative assessment. Currently, we are experiencing a unique momentum with numerous models developed for detecting human settlements from EO data (Table 5). The availability of a large amount of building footprint (BF) vector data allows for a fair comparison of these models' performances (see section 5.1.2). It provides an opportunity to compare the GHSL model with other state-of-the-art realizations and evaluate the effectiveness of Symbolic Machine Learning (SML), extensively utilized by GHSL (Pesaresi et al. 2016a; 2016b).

Section 6 provides the most important thematic findings from the new GHSL data, including shared socio-economic pathways toward 2100. Finally, Section 7 makes explicit the main limitations of the GHSL, indicating the next steps for the research community for an improved assessment of global human settlements.

2. Theoretical background

The 'Human Settlement' (HS) abstraction adopted by GHSL is composed by two essential components: buildings and their inhabitants (see Table 1 – Definitions used in the manuscript). This is predicated by established geographical principles (Stone 1965), town and regional planning practices (Doxiadis 1970), regional science (Isard 1949), and reinforced by recent theoretical advances on urban complex systems (Bettencourt 2021). Therefore, GHSL data expand well beyond a land cover product derived from EO. Figure 2 and Figure 3 show the anatomy of the main GHSL components in Paris (France) and Ho-Chi-Min city (Vietnam), respectively.

The GHSL involves free and open access to data, methods, and results as proposed by the FAIR Data Principles (Wilkinson et al. 2016) and the Group on Earth Observations (GEO) '*full and open*' Data Sharing Principles[1], formalized by the 2019/1024 EU directive.[2] Additionally, GHSL is framed by the *evidence-based output analytics* and the *full repeatability of the measures*[3] principles (National Institute for Standards and Technology 2007). These principles preclude the use of methods that require random iterative searches for inferential solutions, which are commonly employed in frameworks such as Random Forest, Support Vector Machine, and Artificial Neural Network, frequently used in remote sensing applications (Pesaresi 2018). The goal of GHSL is to provide fine-

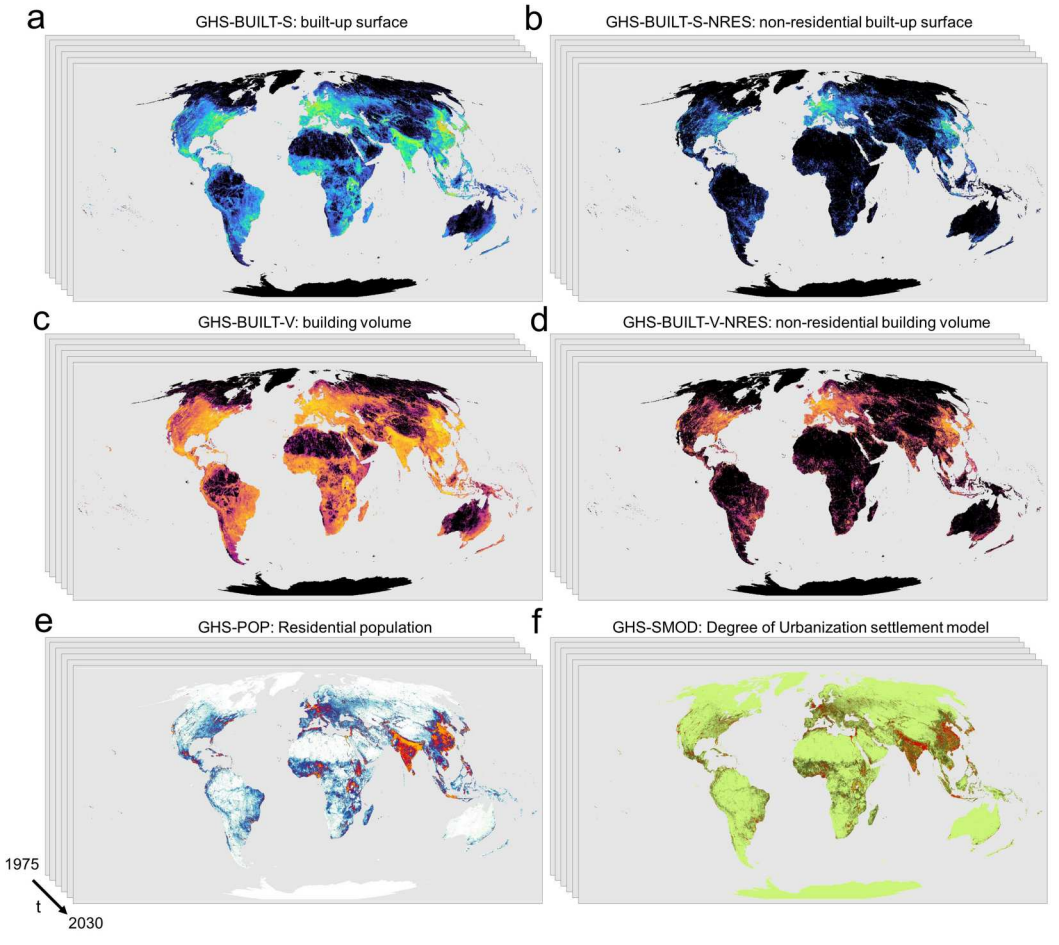

Figure 1. The multi-temporal global data products of the GHSL R2023A data suite (1975-2030). (a) GHS-BUILT-S: Total built-up surface, (b) GHS-BUILT-S-NRES: Surface of dominant non-residential use, (c) GHS-BUILT-V: Total building volume, (d) GHS-BUILT-V-NRES: Dominant non-residential building volume, (e) GHS-POP: residential population distribution, and (f) GHS-SMOD: Degree of urbanization settlement model. All data products (a) – (e) are available at a spatial resolution of 100 m, except (f) which is available at 1 km spatial resolution. In the visualizations shown here, all datasets were aggregated to blocks of 20 km × 20 km.

scale, globally consistent measurements that focus on human settlements, essential for international comparability and to support public decision-making (Pesaresi 2018; Pesaresi et al. 2016b), which require simple and easily interpretable assumptions, thereby discouraging the use of over-parametrized models (Bo 1976).

Furthermore, in line with the *actionable metrics* objectives (Mach et al. 2020), GHSL is designed as an integrated spatiotemporal information system, allowing for causal hypothesis testing across socio-environmental scopes (Gao et al. 2022). It is crucial to identify computationally simple model solutions that facilitate the multilateral democratization of information production and the principles of collective knowledge building (Pesaresi 2018). This is also key to promoting the environmental sustainability of Artificial Intelligence (AI) systems (van Wynsberghe 2021).

Human settlements challenge simple land cover classification; therefore, spatial information design should consider their physical properties and context complexity, moving away from the standard land use/land cover paradigm toward a modular multiple-abstraction approach (Pesaresi and Ehrlich 2009).

Table 1. Definitions used in the manuscript.

Term	Definition
Building	'Any roofed structure erected above ground for any human use, including structures in slums, informal settlements, and refugees/IDP camps' (Pesaresi et al. 2013) (European Commission. Joint Research Centre. 2023; Pesaresi et al. 2015a).[19]
Building height	'The distance measured from the mean ground level to the mean height of the roof' (Pesaresi et al. 2021).[20]
Built-up surface	'The gross building surface (including the thickness of the walls) bounded by the building wall perimeter' (European Commission. Joint Research Centre. 2023).
Built-up volume	'The product of the gross built-up surface by the building height'.
Residential area	'Area dedicated prevalently for residential use, including mixed with other non-conflicting uses' (European Commission. Joint Research Centre. 2023).[21]
Non-residential area	'Area dedicated exclusively to non-residential use', as typically large industrial or commercial/ retail units, confined animal feeding, indoor farming, hangars, data centers, transportation (ports/airports facilities), large gov. administration or offices units, large sport / leisure indoor facilities, exclusive religious sites and similar (European Commission. Joint Research Centre. 2023).
Place of residence	'The place where a person normally spends the daily period of rest, regardless of temporary absences for purposes of recreation, holidays, visits to friends and relatives, business, medical treatment or religious pilgrimage'[22,23,24] (Freire et al. 2016).
Urban, Suburban/Peri-urban, Rural area	'A specific combination of resident population density or built fabric density and settlement population size observed at a definite spatial generalization scale', according to the degree of urbanization (DEGURBA) methodology (Dijkstra et al. 2021).

Coherently with the modular multiple-abstraction approach, the spatial information provided by the GHSL is organized in three levels, hierarchically ordered from low to high abstraction (Figure 4) in a hierarchical multiple-abstraction meta-model (HAMM). This structure is consistent with the Discrete Field of Image Descriptors (DFID) concept, which was introduced in the early GHSL definition (Pesaresi et al. 2013). Finally, the focus of

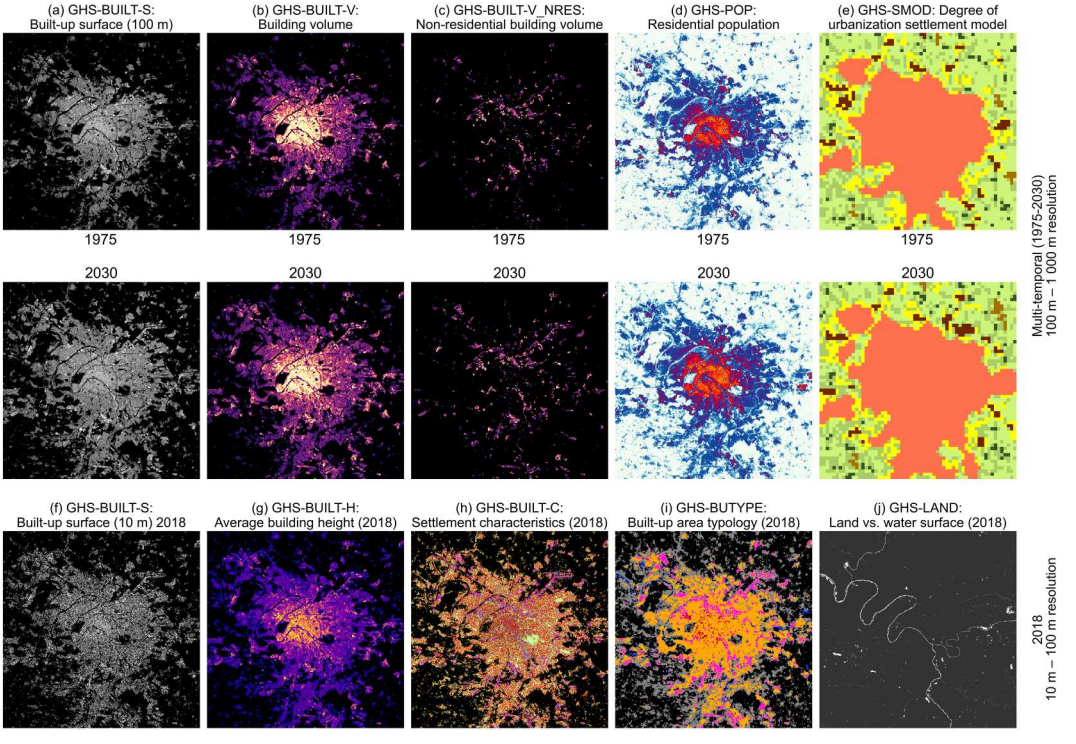

Figure 2. Anatomy of the main GHSL components for the city of Paris, France.

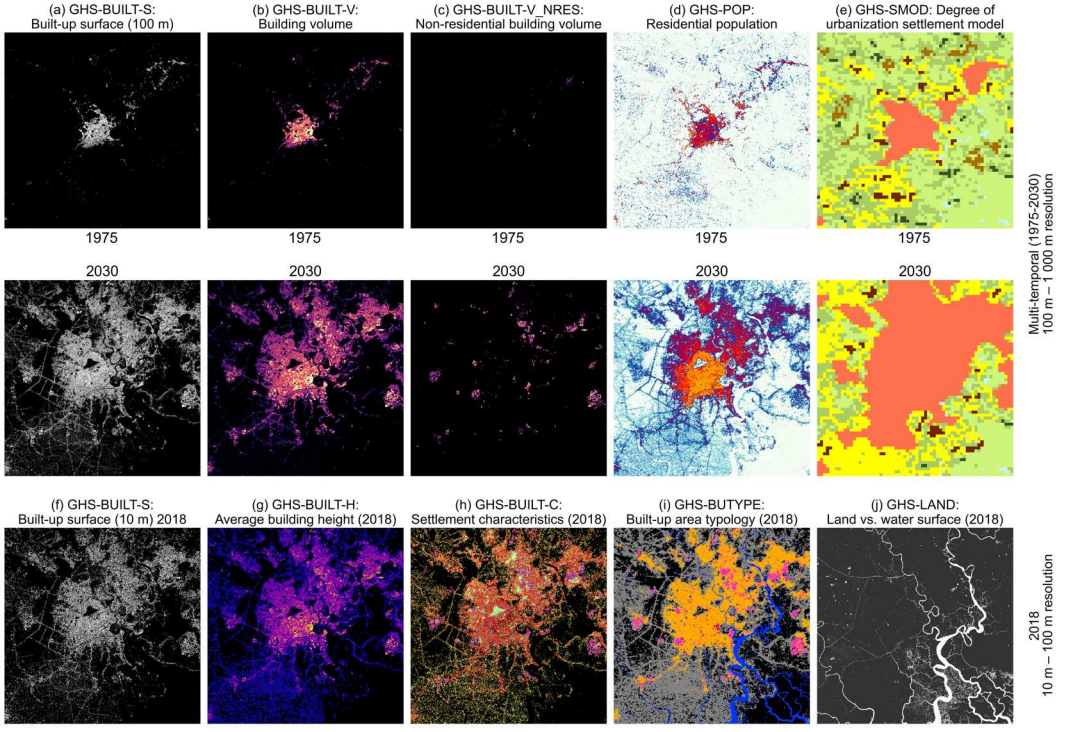

Figure 3. Anatomy of the main GHSL components for the Ho Chi Min city, Vietnam.

GHSL information is *continuous quantitative*, centered on the presence of buildings (built-up surface and building volume per spatial unit) and their inhabitants (number of residents per spatial unit).

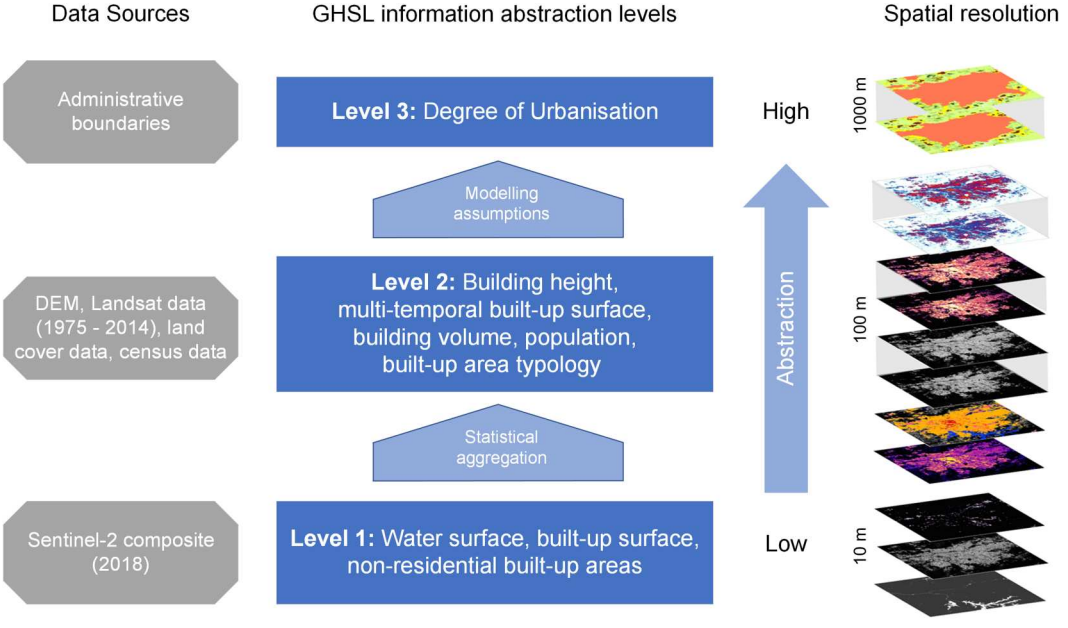

Figure 4. The GHSL hierarchical multiple-abstraction meta-model (HAMM) for spatial information production.

3. Information products: background

In this chapter we provide an overview of the principles behind the development of GHSL modules (Table 2).

3.1. Land vs. water surface

Water surface data is crucial for understanding ecosystem impacts, resource vulnerability, and hydro-geological hazards. The sub-pixel water surface fraction (fWATER) layer provides land vs. water surface fractions per 10 m resolution grid cell that is used in several other GHSL production modules (Figure 7). The automatic detection of built-up and water classes using 10 m resolution Sentinel-2 image input was demonstrated in 2016 (Pesaresi et al. 2016a) using SML. Today, only few global products predict water class from 10 m resolution Sentinel-2 image data, including ESA World Cover (Zanaga et al. 2021), ESRI Land Use Land Cover (Karra et al. 2021), and Dynamic World (Brown et al. 2022). However, none of these products predict continuous sub-pixel surface fractions of water and land. The fWATER module was first introduced in GHSL R2022 (Pesaresi and Politis 2022) applying SML.

3.2. Built-up surface

Since the late 1990s, mixture models have been utilized in remote sensing for precise land cover estimation (Ichoku and Karnieli 1996). These models reduce the dependency of surface estimates on sensor resolution, a key requirement for the quantitative approach of the GHSL. The EO-derived classification of the urban environment, with its fine scale and mix of materials[4] (Small 2003), greatly benefits from these models. The first global attempt to produce sub-pixel built-up surface fraction (fBU) estimates was based on Φ semantic extracted from Landsat imagery and fuzzy

Table 2. Acronym data table of the GHSL modules and products.

Module	Description	Product	Epoch	Link
BU-S MT	Multi-temporal total built-up surface estimation	GHS-BUILT-S R2023	1975-2030	https://doi.org/10.2905/9F06F36F-4B11-47EC-ABB0-4F8B7B1D72EA
BU-S-NRES MT	Multi-temporal non-residential built-up surface estimation	GHS-BUILT-S-NRES R2023	1975-2030	https://doi.org/10.2905/9F06F36F-4B11-47EC-ABB0-4F8B7B1D72EA
BU-H	Building height estimation	GHS-BUILT-H R2023	2018	https://doi.org/10.2905/85005901-3A49-48DD-9D19-6261354F56FE
BU-V MT	Multi-temporal built-up volume estimation	GHS-BUILT-V R2023	1975-2030	https://doi.org/10.2905/AB2F107A-03CD-47A3-85E5-139D8EC63283
BU-V-NRES MT	Multi-temporal non-residential built-up volume estimation	GHS-BUILT-V-NRES R2023	1975-2030	https://doi.org/10.2905/AB2F107A-03CD-47A3-85E5-139D8EC63283
MSZ	Morphological Settlement Zone delineation and inner classification	GHS-BUILT-MSZ R2023	2018	https://doi.org/10.2905/3C60DDF6-0586-4190-854B-F6AA0EDC2A30
FUN	Residential vs. non-residential functional classification of the built domain	GHS-BUILT-FUN R2023	2018	https://doi.org/10.2905/3C60DDF6-0586-4190-854B-F6AA0EDC2A30
POP MT	Multi-temporal resident population count estimation	GHS-POP R2023	1975-2030	https://doi.org/10.2905/2FF68A52-5B5B-4A22-8F40-C41DA8332CFE
SMOD MT	Multi-temporal settlement typology classification	GHS-SMOD R2023	1975-2030	https://doi.org/10.2905/A0DF7A6F-49DE-46EA-9BDE-563437A6E2BA
DUC MT	Multi-temporal classification of administrative units by Degree of Urbanization[25]	GHS-DUC R2023	1975-2030	https://doi.org/10.2905/DC0EB21D-472C-4F5A-8846-823C50836305
fWATER	Sub-pixel permanent water surface fraction estimation	GHS-LAND R2022	2018	https://doi.org/10.2905/AB7AD451-5ED5-44A6-A4D0-9F7A4E848CEE
fBU	Sub-pixel built-up surface fraction estimation	GHS-BUILT-S R2023 (E2018)	2018	https://doi.org/10.2905/9F06F36F-4B11-47EC-ABB0-4F8B7B1D72EA
BUTYPE	Built-up typology classification	N/A	2018	Introduced in this manuscript
MTUC	Multi-temporal urban centers vector data base	N/A	1975-2030	Introduced in this manuscript

logic (Pesaresi et al. 2016b). This model was abandoned owing to lack of reference data for global evaluation. Later research on processing Sentinel-2 composite imagery (Corbane et al. 2020a) led to an SML-driven prototype GHS-BUILT-P (2019) used as internal prototype, and a CNN-driven product, GHS-BUILT-P (2020) (Corbane et al. 2021), both expressing the built-up semantic in a probabilistic continuous approach. In 2020, research focused on obtaining fBU from filtering and rescaling of GHS-BUILT-P (2020) predictions. However, anomalies in the resulting data led to the rejection of this model. In 2021, a consolidated model was developed by improving the training data sampling schema of the GHS-BUILT-P (2019). The GHS-S R2023 is the first global dataset estimating continuous sub-pixel BU surface fraction, at a 10 m resolution (see Appendix section C). The fBU technical specifics demonstrated in the GHSL R2023, are part of the exposure mapping component into the Copernicus Emergency Management Service (CEMS) (Melchiorri and Kemper 2023).

3.3. Residential vs. non-residential built-up class

Regional analysis and planning require the categorization of human settlements into functional areas such as residential (RES) and non-residential (NRES). This classification is vital for various domains, and it is also instrumental in modeling spatially explicit resident population density, which can be further differentiated into night-time vs. day-time population density for a more accurate disaster exposure assessment (Freire 2010).

Despite the huge benefits of classifying built-up areas into residential and non-residential categories, there is no comprehensive and publicly available global dataset. To date, the available information layers focus solely on assessing a single abstraction class for built-up areas; whereas built-up areas functional mapping projects are either locally focused or use hybrid human – and machine-driven data classification procedures.[5] This limits the possibility of scaling these projects to produce globally consistent information products. The first framework for a global delineation of commercial areas was addressed in early GHSL work (Pesaresi et al. 2016b), but it was later abandoned due to insufficient data to support a global validation. The application of SML for discriminating NRES built-up areas was demonstrated on a Europe-wide EO data classification exercise (Corbane et al. 2020b). The limiting factor of this approach at the global scale was the incompleteness and geographical bias of the available land use information. The new approach developed for the GHSL R2023 overcame these limitations by alternating deductive and inductive automatic inference, leading to the augmentation of the available training set (see Appendix section D).

3.4. Height of buildings

Global building height estimates are crucial for population disaggregation, detection of overcrowding and affordability, construction volume and cost, disaster risk reduction, and monitoring progress towards Sustainable Development Goals.

The initial GHSL R2016 pioneered the concept of spatially explicit estimation of vertical components of built-up areas at a sub-kilometre scale, achieved through direct filtering of global DEM data (Pesaresi et al. 2016b). This approach was later enhanced by applying multiple linear regression to the filtered DEM data (Goch et al. 2023; Pesaresi et al. 2021). Currently, there are several globally available options. These include direct filtering of Tandem-X data (Esch et al. 2022), filtering of Alos3D DEM at a 30 m resolution (He et al. 2023), and direct filtering of Sentinel-1 radar imagery at a 20 m resolution (Li et al. 2022; Zhou et al. 2022).

In the GHSL R2023, we calculated the average height of the buildings at a resolution of 100 m for the year 2018. This was achieved by application of a robust ensemble modeling approach, introducing a multiple-objective, univariate linear regression mechanism and an update mechanism based on locally-adaptive linear regression from filtered Sentinel-2 image composite for building shadow

marker detection. The GHS-H R2023 is the first global building height layer derived through the integration of DEM with Sentinel-2 (see Appendix, section D).

3.5. Multi-temporal dynamics of built-up surfaces and volumes

GHSL (Pesaresi et al. 2016b) pioneered the classification of global, multi-temporal built-up areas by utilizing decametric-resolution satellite imagery. This was achieved with a static learning set derived from 500 m resolution MODIS data, which led the way in describing urban land use on a global scale (Schneider, Friedl, and Potere 2010). This was enabled by two innovations: the inter-scale learning classification paradigm (Gueguen and Pesaresi 2014) and SML (Pesaresi, Syrris, and Julea 2015; 2016a), facilitating cost-effective, robust classification of global, high-resolution EO data. Recent advances have allowed the production of multi-temporal built-up land cover layers from Landsat data. All these layers measure change in terms of categorical land cover counts, dependent on sensor resolution.[6] In 2021, the first GHSL MT prototype merged Landsat and Sentinel data, following a similar logic to previous GHSL releases R2016, R2019 and supporting the public release R2022. However, this unsupervised binary change mechanism overestimated change rates in rural areas due to the increased sensitivity to scattered settlements of the new Sentinel sensor. This led to a new model (Pesaresi et al. 2024), resulting in the GHS-BUILT-S R2023 and GHS-BUILT-V R2023 releases. The GHSL R2023 introduces two innovations: continuous surface change prediction[7] through SML-based linear regression ensemble, and integration of Landsat data with Sentinel-2 EO data at 10 m resolution. GHSL R2023 is the first instance of a multi-platform and multi-temporal dataset, combining Landsat and Copernicus data (see Appendix section F). The integration of population census data enables to estimate human population distribution over the whole time series (Figure 5).

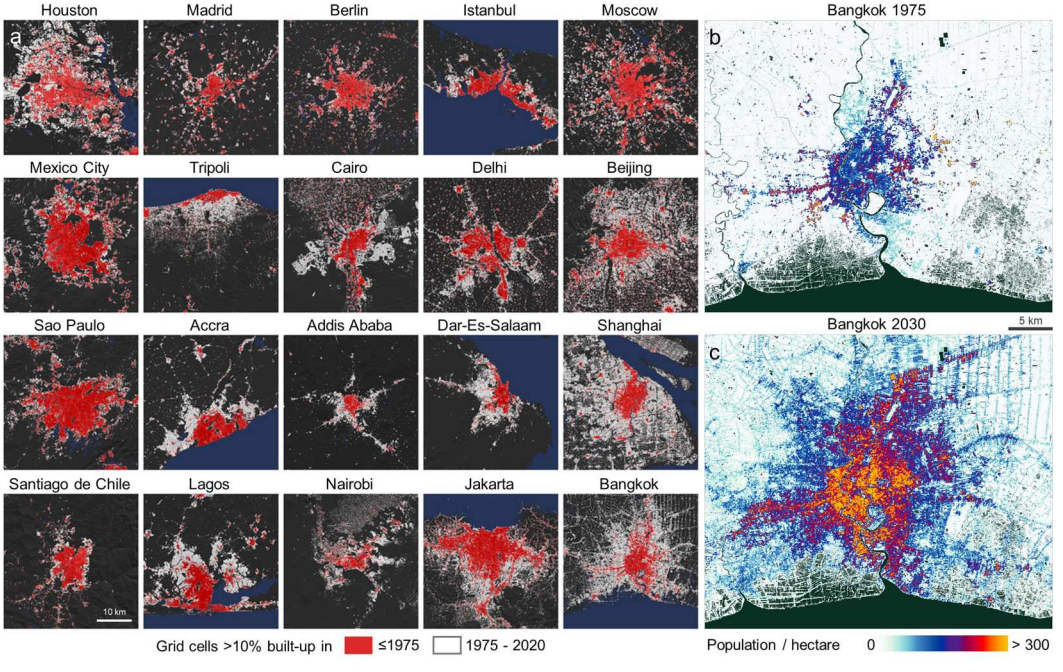

Figure 5. Assessing urbanization through the lens of the GHSL. (a) Examples of the 100 m GHS-BUILT-S R2023 multitemporal built-up surface estimates for characterizing urban growth, shown for a global sample of metropolitan areas, depicting high-density areas (i.e. > 10% built-up surface) in 1975 and in 2020. Each map covers 40 km × 40 km and is shown in the local UTM projection. Cities are arranged in an approximate geographic space, i.e. upper left = Northwest, lower right = Southeast; Right part: Example of GHS-POP R2023 at 100 m resolution for Bangkok (Thailand) (b) in 1975 and (c) extrapolated to 2030.

3.6. Inner morphological characteristics of human settlements

Surface, height and volume of buildings are essential features in urban analysis to understand urban forms (Oliveira 2019) associated with population density, urban expansion/densification trajectories (Angel et al. 2021; Angel and Lamson-Hall 2020), and urban Local Climate Zones (Angel et al. 2021; Angel and Lamson-Hall 2020; Bechtel et al. 2018; Conzen 1960; Kropf 2018; Oliveira 2019; Salat 2011). Urban morphology significantly influences the Urban Heat Island phenomenon and enhances Earth system modeling (Balsamo et al. 2018; Huang et al. 2017; Ratti, Baker, and Steemers 2005) with implications for air pollution dispersion (Ratti et al. 2002), building energy consumption, solar potential assessment, construction costs, and vulnerability to natural hazards. Despite its importance, global data on urban morphology is scarce. GHSL first introduced an experimental inner taxonomy of human settlements as 'built-up areas characteristics' (Pesaresi et al. 2016b), and later, the Morphological Settlement Zone (MSZ) (Pesaresi and Politis 2023a). This manuscript introduces the 'Built Typology' (BUTYPE) taxonomy. Both MSZ and BUTYPE empirically support Conzen's 'morphotope'[8] notion at the 10 m resolution and 100 m resolution levels of the GHSL (Figure 6).

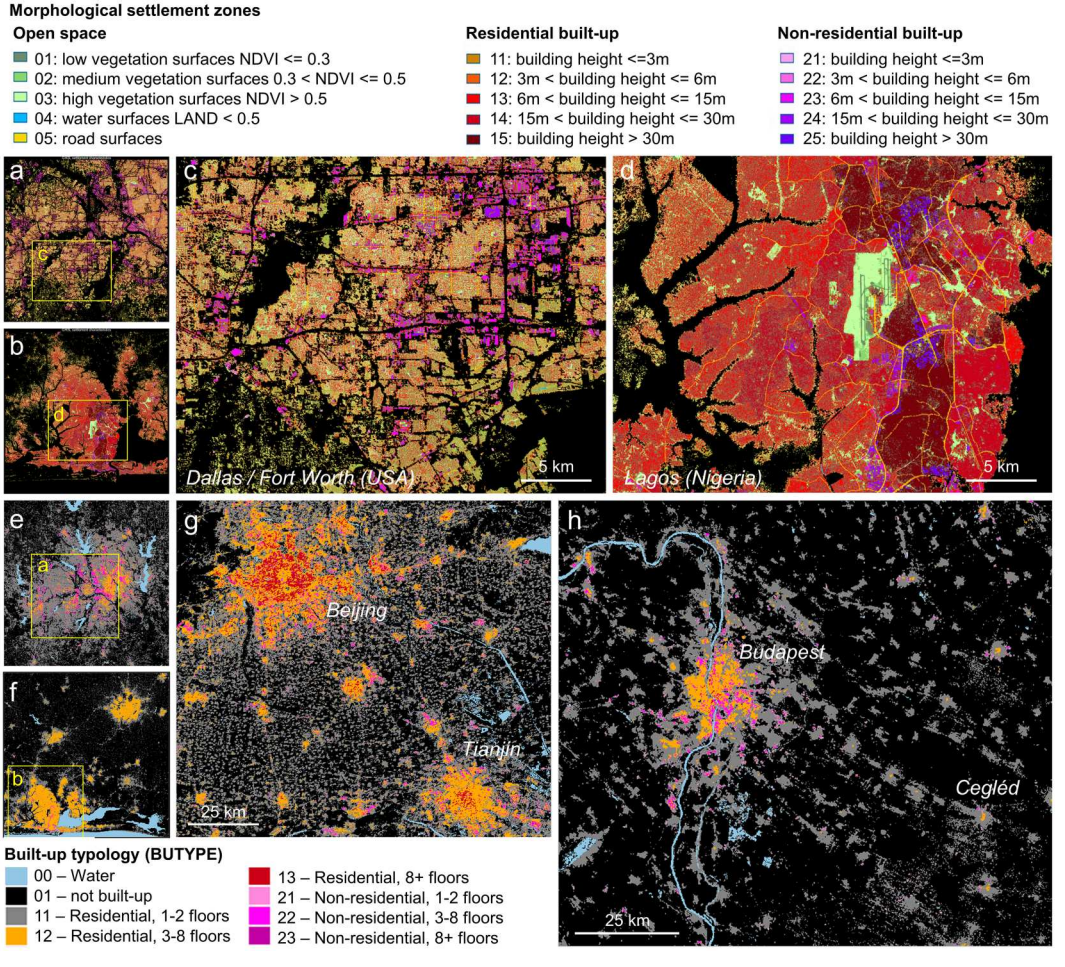

Figure 6. GHSL taxonomies at 10 and 100 m resolution. The Morphological Settlement Zones (MSZ) at 10 m resolution of (a) Dallas / Fort Worth (USA) and (b) Lagos (Nigeria), with enlargements of the same cities in (c) and (d), correspondingly. The Built-up Typology (BUTYPE) at 100 m resolution for (e) Dallas / Fort Worth and (f) Lagos. The BUTYPE is also shown in the regions of (g) Beijing (China), and (h) Budapest (Hungary).

3.6.1. The morphological settlement zone

The Morphological Settlement Zone (MSZ) provides a qualitative representation of the characteristics of human settlements and is defined at the most detailed level of the GHSL HAMM (Figure 4). This level corresponds to the highest spatial resolution (10 m) allowed by the current EO sensors supporting the GHSL. The primary aim of this representation is to facilitate the visual inspection of the GHSL integrated data at 10 m resolution. The MSZ taxonomy was constructed using a hierarchical symbolic methodology, where the size of symbols does not directly correspond to the area represented by the underlying spatial variables, but it is influenced by a hierarchical semantic significance and a collection of spatial generalization rules.

3.6.2. The built typology

The Built Typology (BUTYPE) purpose is to stratify the GHSL information at the intermediate level of the HAMM (Figure 4), where the key components of the GHSL are integrated to generate added value. BUTYPE is designed to answer queries about built-up areas. It provides data on built up surface and volume as well as on building type, the average population, the average density or floor area per person, and the spatial distribution of building types, such as proximity to city centers.

3.7. The population distribution

The POP MT module aims to create a fine-scale, global population distribution representation for policymaking by integrating official statistics with Earth Observation (EO) information. It aligns with the UN World Population Prospects 2022 estimates (United Nations, Department of Economic and Social Affairs, Population Division 2022), enabling both temporal and international comparisons. The GHSL R2016 initially introduced fine-scale, multi-temporal population grids, utilizing the same inferential engine for downscaling census data since its inception. This approach is based on linear dasymetric mapping, which is proportional to predicted built-up intensity. Prior to 2022, GHSL releases relied on total built-up surface for population downscaling. However, the R2023 releases introduced residential built-up volume as a predictor, thereby focusing the model on nighttime population presence, aligning with the definition of 'place of residence' (Table 1).

3.8. The settlement model and the degree of urbanization

The GHSL Settlement Model (SMOD) and the GHSL Degree of Urbanization Classification (DUC) are global, multi-temporal implementations of the Degree of Urbanization (DEGURBA), a population-based geospatial classification method of the urban-rural continuum (Dijkstra et al. 2021; European Commission. Statistical Office of the European Union. 2021). Introduced by the European Commission and refined by multiple international organizations[9], DEGURBA was endorsed by the UN Statistical Commission for classifying settlements beyond the traditional urban-rural dichotomy (UN. Statistical Commission (UNSC) 2020, paras. i-j). This harmonization overcomes biases from heterogeneous national definitions, aiding in monitoring national policies. The modular HAMM design of GHSL (Pesaresi et al. 2013; 2015a; Pesaresi and Ehrlich 2009) ensures information gathering at lower abstraction levels remains independent from the top-level class abstraction definition (Figure 4). This facilitates discussions of alternative urban-rural definitions among stakeholders based on an agreed spatial and thematic baseline to enable an internationally accepted methodology.

4. Information products: materials and methods

4.1. General overview

Figure 7 illustrates the GHSL R2023 information production workflow. The techniques employed to generate the GHSL information adhere to the principles outlined in the theoretical background

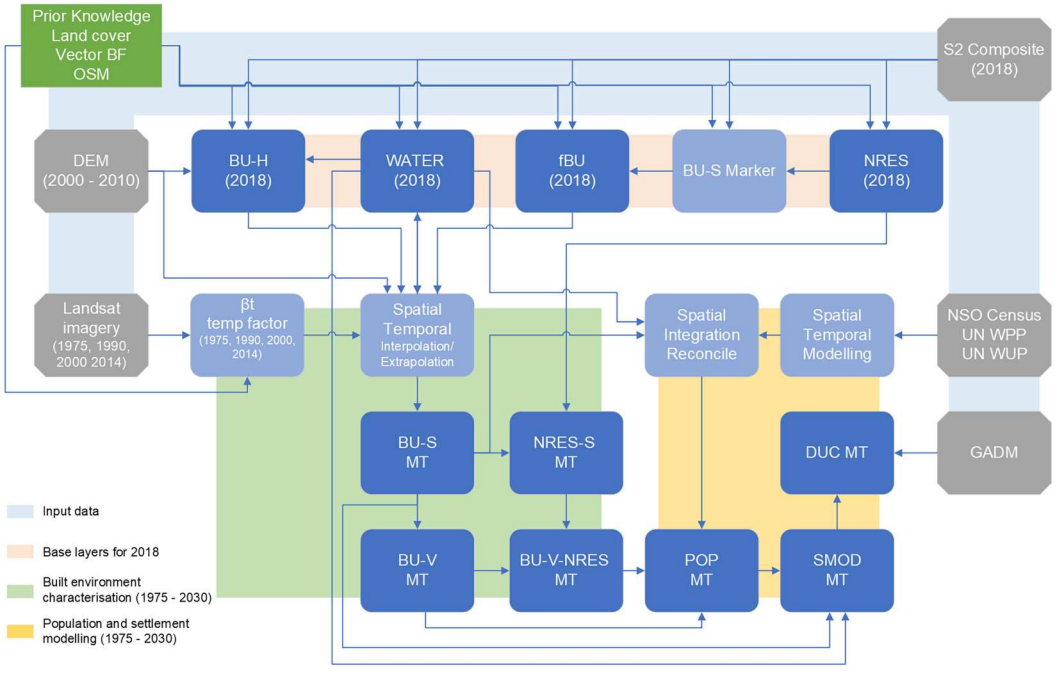

Figure 7. General workflow of the GHSL production. The primary input data are emphasized in grey, while the pre-existing knowledge prior to the process is depicted in green. The initial intermediate products are indicated in light blue, and the ultimate output products, also known as 'production modules', are represented in dark blue.

(Section 2) and include: multi-scale morphological and textural filtering, SML, univariate multiple-objective linear regression, univariate linear dasymetric mapping, and ensemble modeling. Notably, most of the information extracted from EO data in the GHSL, apply SML to discover a static set of associative rules, linking data with semantics. This contrasts with the current approaches that dominate the EO data field (Boden 2008), such as Artificial Neural Networks and random-iterative over-parametric inferential solutions.

It is worth noting that from the beginning, the GHSL was designed as a *self-evolutionary* information production system, achieved through the introduction of multi-scale learning and classification (Gueguen and Pesaresi 2014), coupled with SML (Pesaresi, Syrris, and Julea 2015; 2016a). The GHSL system enhances its predictions by learning from approximate semantic solutions that are available prior to adding new data (Figure 8).

4.1.1. Symbolic machine learning

Symbolic Machine Learning (SML) is a novel supervised classification framework designed to address big geo-spatial data challenges (Corbane et al. 2017; Pesaresi et al. 2015a; Pesaresi et al. 2016a; 2016b). It operates on two primary processes: (i) input image data reduction and sequencing, and (ii) association analysis. In the sequencing phase, the input data is transformed into a series of symbols (called data *sequences*), creating a compact and multidimensional sparse representation. The association analysis phase then constructs rules that link these data sequences with a high-abstraction information layer, also referred to as the reference set, training set or supervisory signal.

The term 'symbolic' in SML refers to the representation of input data as a finite set of symbols, forming the alphabet of sequences. The concept of machine learning is used in its general sense, referring to the ability of computers to learn without explicit programming.

SML shares similarities with data analytics tools used in other fields, such as genetic association techniques in bioinformatics. These techniques are used to discover significant associations between different genes or between environmental factors and gene expression. Similarly, the

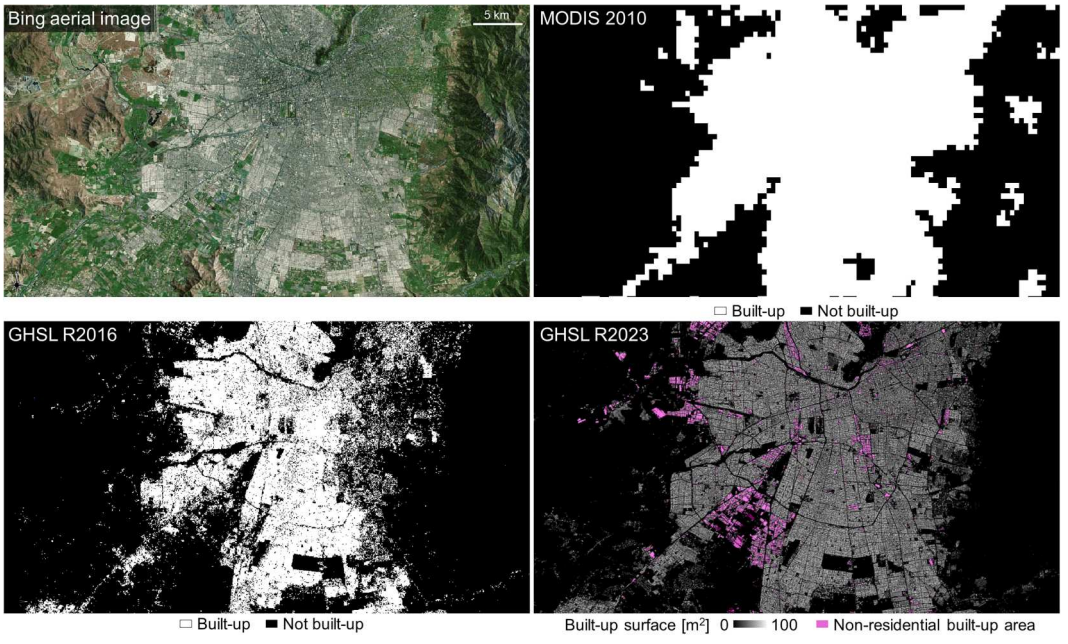

Figure 8. Self-evolutionary GHSL information production system. Santiago de Chile, satellite image (Microsoft ™ Bing © 2024, Earthstar Geographics), MODIS-derived prior knowledge available before the GHSL, the Landsat-derived GHSL BU information generated by using MODIS as SML learning set, and the Sentinel-2-derived information using the Landsat GHSL (R2016 R2019) as SML learning set.

SML association classifier seeks to find meaningful, systematic relationships between sequenced image data instances and supervisory (spatial) information encoded in selected reference sets (Pesaresi et al. 2015a).

The use of SML to produce GHSL layers allowed for a gradual refinement of thematic information, from the initial MODIS binary data at 500 m resolution available in 2010, to the current Sentinel-2-derived continuous prediction of BU surfaces at 10 m resolution.

SML is favored in the GHSL information production for several reasons:

- It uses a frequentist statistical approach, which is parameter-free and can efficiently handle large amounts of noise in the training data set (up to 50%) (Pesaresi, Syrris, and Julea 2015);
- It discovers a finite set of explicit static rules linking data with class abstraction, making classification criteria explicit and facilitating human inspection and discussion of results (Pesaresi, Syrris and Julea 2016b);
- It is computationally low-cost, facilitating the democratization of information production and classification, minimizing the need for model transfer (Pesaresi, Syrris and Julea 2016b).

In subsequent sections, the 'semantic Φ' measures the association between a combination of quantized EO data (a 'data sequence') and a given semantic, such as BU or Non-BU (NBU) classes. We adopt a generalization of SML to multiple quantization. In multiple-quantization SML, a hierarchical pyramid of inferences is created by iteratively applying single quantization SML to a list of quantization parameters. The inferential pyramid is scanned from bottom to top (small to large quantization parameters), and the first SML inference with a given minimal empirical support is selected. Two basic parameters govern the classifier function: the vector of quantization parameters Q^l and the minimal support MinSupp, set as $Q^l = 2^{[0..6]} = [1, 2, 4, 8, 16, 32, 64]$ and MinSupp $= 10$, respectively. To ensure the repeatability of the measurements, they are kept constant across all image data and all semantics processed in the study. The two parameters were determined based

on computational efficiency considerations for the available 64-bit computational machines, and empirical considerations regarding the necessary generalization for the given classification tasks.

4.2. Information from 10 m resolution sentinel-2 data

In this section, we outline the methods used to extract information directly from the 10 m resolution imagery captured by the Sentinel-2 satellite sensor using a data-reduced image composite of nominal year 2018 input (Corbane and Politis 2020), referred to as 'S2CMP'. This represents the bottom level of GHSL HAMM for spatial information production (Figure 4). Specifically, the following information extraction modules are active: (i) fWATER (continuous), (ii) NRES (categorical), and (iii) sub-pixel built-up surface fraction, denoted as fBU (continuous).

4.2.1. Land vs. water surface fraction

Figures 9–11 present the fWATER data in comparison to the available priors before processing and the workflow employed to obtain fWATER respectively Figure 11.

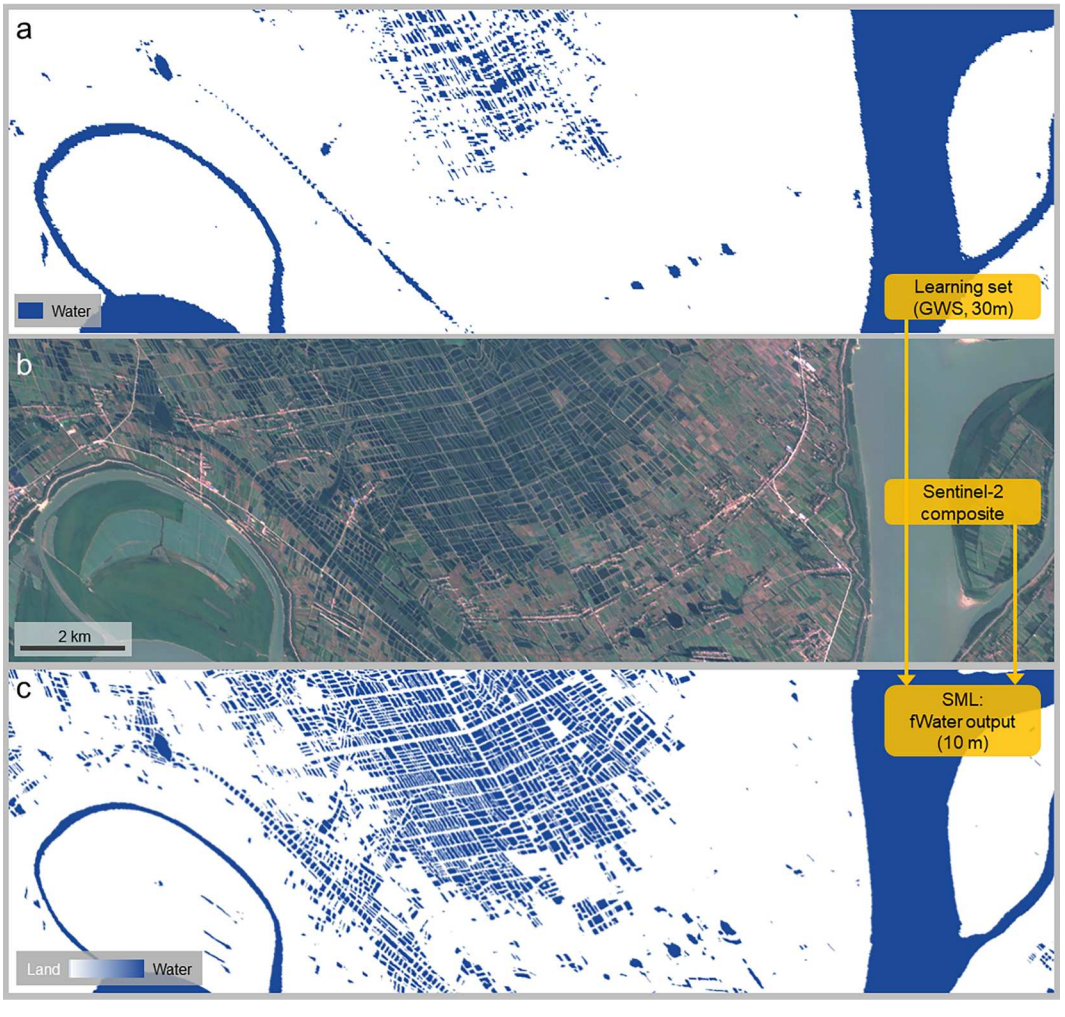

Figure 9. Illustrating the production of fWATER for the region south of Wuhan, west of the Yangtze River, China. (a) Prior information about water presence from the GSW at 30 m resolution as extracted from Landsat data classification, which supports the SML classification of Sentinel-2 data as train set, (b) Sentinel-2 composite imagery, (c) fWATER, the output of the SML classification of 10 m resolution Sentinel-2 imagery. Note the presence of thin fish farm structures that are identified by the SML in the data, despite them largely contradicting the available training set.

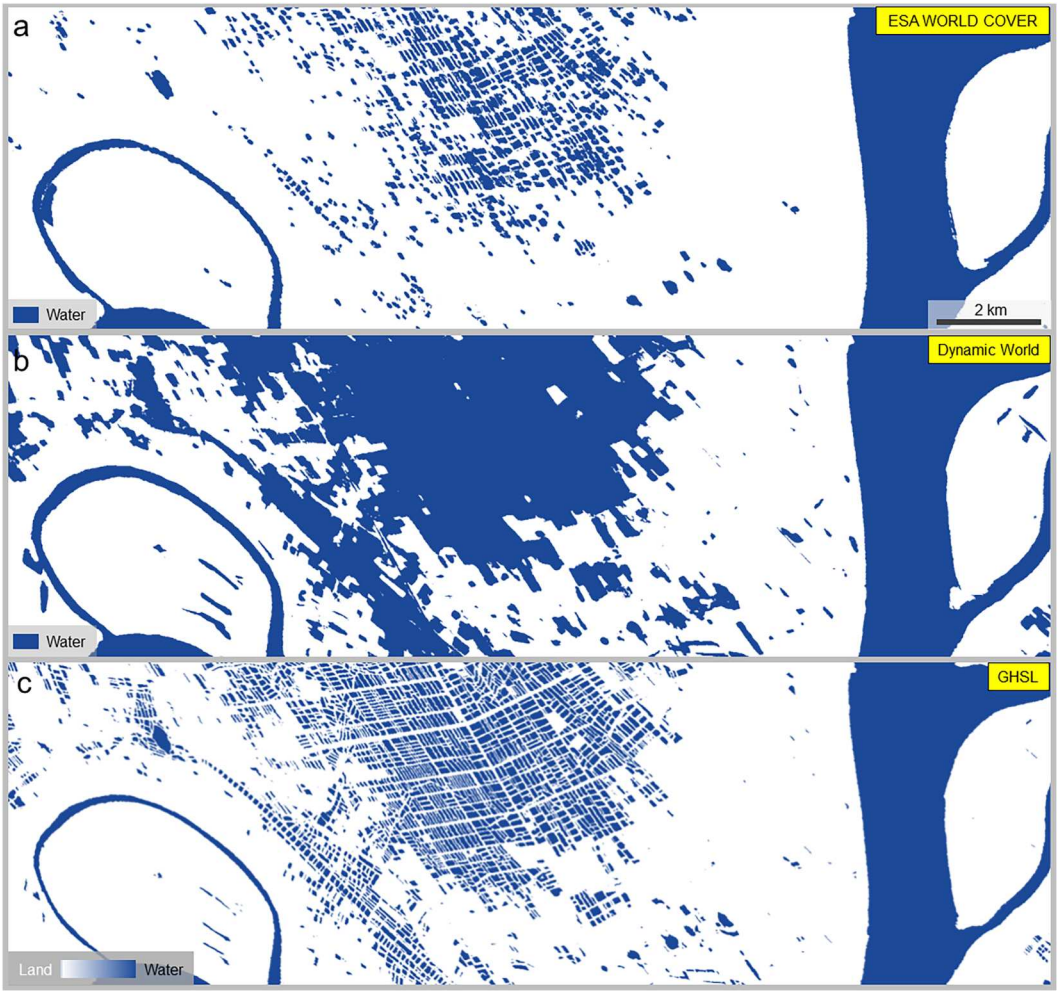

Figure 10. Alternative water data products derived from Sentinel-2 Images for the Region South of Wuhan, West of the Yangtze River, China. (a) 'water' class as per the ESA WORLD COVER classification, (b) 'water' class according to the DYNAMICWORLD 10 m resolution classification, (c) fWATER provided by the SML classification, using the same Sentinel-2 data as in Figure 9 (b).

The combination of quantized reflectance in the S2CMP, DEM-derived slope, and density of built-up surface were associated with the presence of water surface using the SML classifier. The reflectance of water surfaces is similar to shadows in EO images; thus, the DEM slope and the built-up density inputs were included in the SML to allow the model to discover different associative rules in the presence of shadows cast by buildings or mountains. Inputs of the process are the S2CMP, the fBU, and the Copernicus DEM GLO-90 (European Space Agency and Airbus 2022). The fBU module, produced at 10 m resolution, was generalized with a local average filter expressing the density of built-up surface in a kernel of 100 × 100 m. The DEM was used to generate a gridded slope dataset calculated as morphological gradient $s_x = \delta_x - \varepsilon_x$, with δ_x, ε_x representing the grey-scale morphological dilation and erosion (Serra 1982), respectively, of the x DEM data. The SML classifier was applied in a geographically–adaptive approach, learning the associative rules in the data for each 100 × 100 km data tile.

The training set was derived by augmentation and refinement of the available priors supported by unsupervised classification of the S2CMP data. A 30 m resolution water mask was extracted from Global Surface Water (GSW) layer (Pekel et al. 2016) applying a cut-off value of water occurrence of

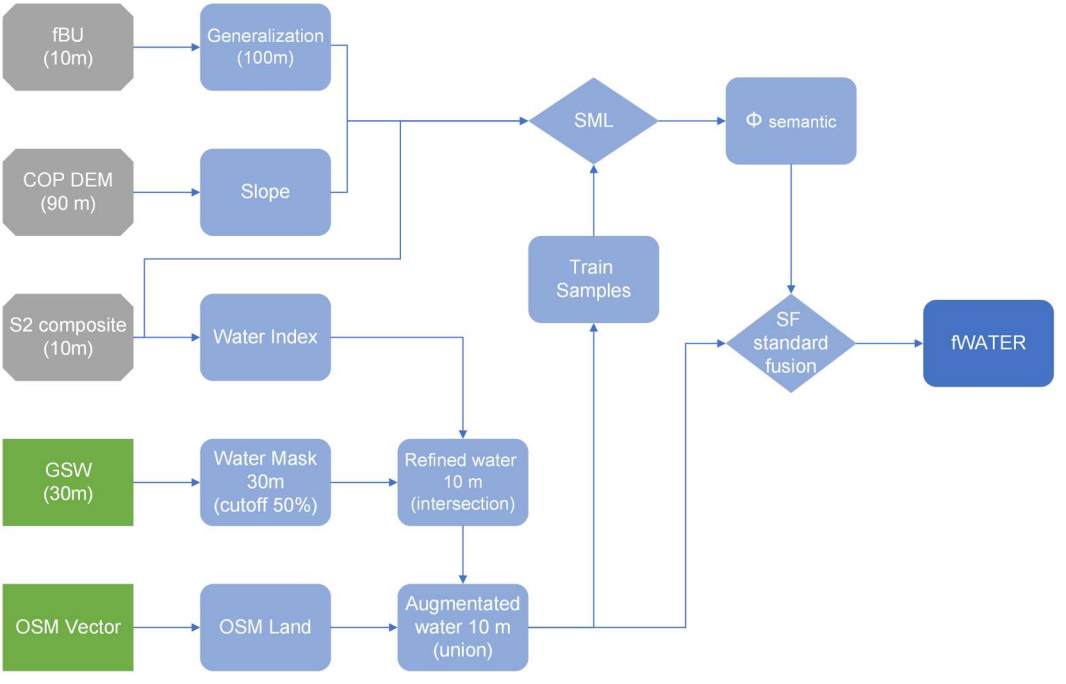

Figure 11. Workflow of the method applied to produce the water-land permanent surface fraction.

50%. The 30 m resolution water mask was further refined by intersecting it with a water presence index ($S2w$) derived from S2CMP data as $W_r = GSW > 50 \cap S2w > 1$. $S2w$ is the ratio between the RGB luminance, and the near-infrared (NIR) signal recorded in the Sentinel-2 composite: $S2w = max(S2_{red}, S2_{green}, S2_{blue})/S2_{NIR}$. Water presence in the image sample induces larger absorption (lower reflection) in the NIR signal reported by the S2CMP. The refined water mask was used to augment the water surfaces as obtained from querying OSM vector data for coastline and stream networks: $W_a = W_{OSM} \cup W_r$. The W_a was used as training set for the SML classifier, in each data tile of 100×100 km, and the water surface fraction fWATER was obtained by linear rescaling the Φ semantic in the interval $[-1, 1]$ to the interval $[0, 1]$. Thus, it is assumed that the water surface fraction is linearly proportional to the semantic Φ associating S2CMP data with the W_a Boolean priors. S2CMP data gaps (e.g. in Antarctica, or extreme Northern latitude, or residual gaps in the Sentinel-2 image data tiles) were filled by injecting the W_a priors to achieve a seamless and complete global data baseline. Visual comparative examples of fWATER are generated for the Venice Lagoon and Yangtze River regions in the Appendix, specifically in sections L.1.1 and L.1.2, respectively.

4.2.2. Built-up surface fraction

Figure 12 illustrates the applied workflow to produce fBU based on SML applied to S2CMP. The Union Of the Positive Prediction (UOPP) was derived from the available thematic products, including the GHS-BUILT-P (2020) probability (Corbane et al. 2021) and the GHS-BUILT R2019, with the objective of maximizing the sensitivity towards the presence of built-up structures while mitigating the problems related to data gaps and under-detection of large industrial buildings and dense urban patterns in the CNN-derived GHS-BUILT-P (2020) that were noticed during the model development (see Appendix section C). The training samples for SML were generated by merging the UOPP with categorical layers. These layers were extracted from the NRES model prediction (A) and from the direct filtering of S2CMP data. Textural filtering was used to detect the hyper-dense BU-S domain (B), which is characterized by open spaces of size 1-2 m, that are significantly smaller

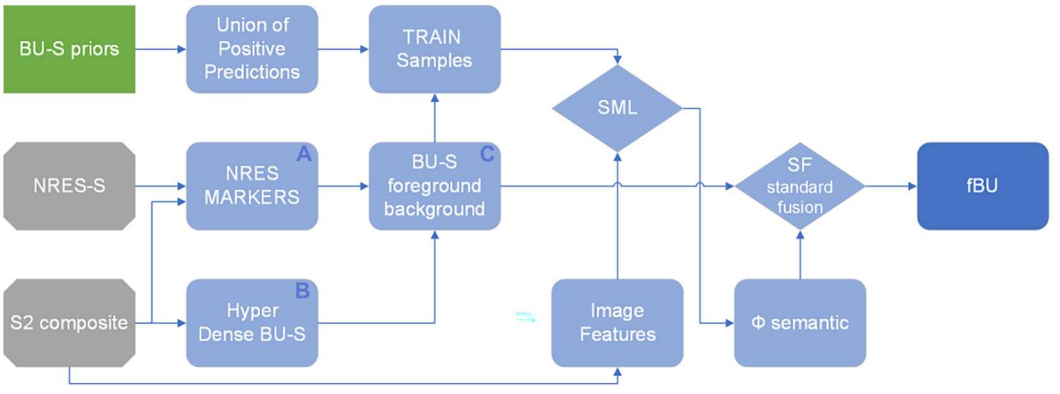

Figure 12. Workflow of the 10 m resolution sub-pixel built-up surface fraction model.

than the 10-meter resolution of the S2CMP sensor. Thus degrading the capacity to infer built-up surface from the image structural characteristics. To differentiate between the foreground and background hypothesis (C), an alternating open/close morphological filtering technique was used. Lastly, a random equalized sampling scheme was implemented. This ensured the collection of an equal number of negative examples in the vicinity of positive examples. More details in the Appendix C: 'Built-up surface fraction (fBU)'. Sampling in the *spatial vicinity of the opposite class* and selecting samples of *equal size* are central criteria for the sampling design to ensure that the SML model can approximate the sub-pixel surface fraction of the BU class. The image-derived features used as inputs in the SML model (see Appendix section C.5): four radiometric channels of the Sentinel-2 image composite[10], plus four multi-scale morphological transforms of the Sentinel-2 image composite[11] (Maragos and Pessoa 1999; Salembier and Serra 1995; Soille and Pesaresi 2002). These properties enable precise prediction of the built-up surfaces in the image, avoiding blurring effects often observed when applying linear convolution filtering, the prevalent method in CNN applications (Ghanbari et al. 2021). Finally, the continuous Φ semantic extracted by SML was subject to post-processing (SF) including rescaling/standardization, and fusion with the semantic foreground vs. background domains as detected by direct image filtering (C). SF was evaluated through a geographically-adaptive approach across 100 × 100 km data tiles. In this step, several parameter options were tested on a reduced set of vector building footprints available during the model development. The best parameter set was selected based on minimization of the RMSE and applied to the whole data Figure 8 illustrates the enhancement in the built-up information, as evaluated by the newly released GHS-BUILT-S R2023 data. This improvement is compared with the previous R2019 release and the information available prior to the production of GHSL. Visual comparative examples of fBU are generated in the Appendix section L.2, titled 'On the fBU Model,' for the following cases: rural Africa, Kenya (L.2.1), Khora Colony in Noida, India (L.2.2), and the Zaatari refugee camp in Jordan (L.2.3).

4.2.3. Residential vs. non-residential class

The method developed for the FUN module (Figure 13), solves the issues of scarcity, incompleteness, and geographical bias present in land use data employed for training. This was achieved through two steps: 1. the available NRES priors were augmented using heuristic rules derived from images, implementing a deductive inference step; 2. the enhanced NRES data was then utilized as a training set for the SML classification, through an inductive inference step. The process was carried out for each 100 × 100 km data tile, allowing the adaptive detection and formalization of local rules, linking image data with the NRES semantics (see Appendix section D.1). Multi-scale textural image features were extracted by applying the *PANTEX* textural contrast measure (Pesaresi,

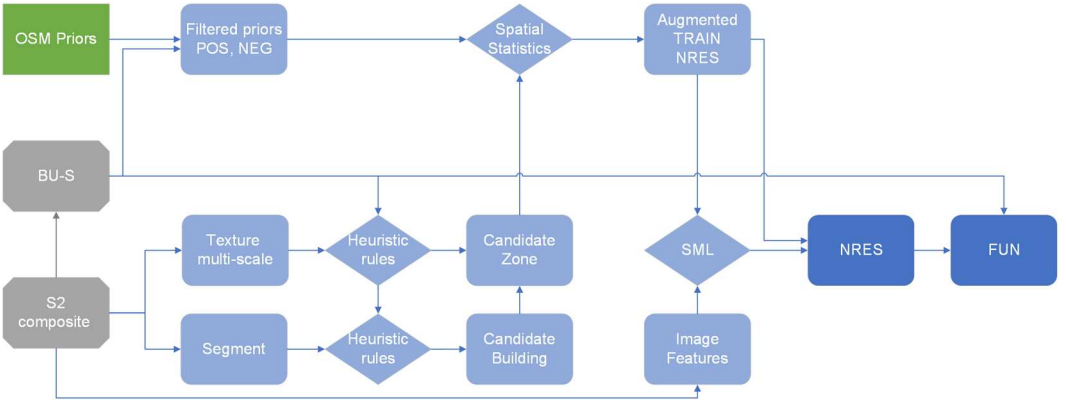

Figure 13. Methodology for the NRES production.

Gerhardinger, and Kayitakire 2008), using different displacement vector distances. The heuristic rules supporting NRES zones were evaluated at the generalization kernels of 100 m size in a fuzzy multi-criteria approach. They include the following criteria: (i) high density of built-up surface, (ii) low response of PANTEX corner detector (Gueguen, Soille, and Pesaresi 2012), (iii) unbalanced response of PANTEX toward larger displacement vectors. The heuristic rules supporting NRES buildings were evaluated at the level of image segments in an object-oriented processing framework. They included the following fuzzy multi-criteria approach: be dominated by built-up surface, high shape compactness, minimal roof size (inscribable diameter disk) of 50 m, and high reflectance in all the RGB bands or a dominant blue component.[12]

The low-level segmentation of the Sentinel-2 image was carried out by a novel method based on the well-known watershed segmentation (Beucher and Meyer 2018; Meyer 1994), here applied to the inverse of the saliency layer in the 'characteristic-saliency-levelling' (CSL) model (Pesaresi, Ouzounis, and Gueguen 2012). This solution allowed to solve the problem of low-level image segmentation using a hierarchical optimized approach, based on the saliency of image-connected-components at different scales (Figure 14).

The candidate zone and buildings determined by Sentinel-2 data unsupervised classification were merged with the filtered priors and are used in the SML as a training set to generate NRES classification at 10 m resolution by applying the semantic ΦNRES > 0 decision. The input image features were the radiometric reflectance in the RGB, and near-infrared bands, augmented by the multiscale morphological decomposition of the luminance in the scales from 10 to 100 m using the DMP (Pesaresi and Benediktsson 2001). The samples where BU-S > 0 and do not belong to NRES are classified as RES. The result of the FUN module was the 10 m resolution GHS-BUILT-FUN R2023 grid, which classifies the built-up domain into residential and non-residential (see Appendix section D).

4.3. 100 m resolution, multiple-source integrated information

In this section, we describe the methods used to construct the GHSL information by integrating various sources: imagery from multiple satellite platforms (such as Sentinel and Landsat), EO-derived information like Digital Elevation Models (DEM), and population count data from census. This represents the intermediate level of the GHSL hierarchical meta-model for spatial information production (Figure 4). Specifically, we generate the 5-year-interval multi-temporal components from historical series of Landsat imagery (BU-S MT, BU-S-NRES MT), the building heights (BU-H), and the derived volumetric prediction (BU-V MT and BU-V-NRES MT), which are also projected in the multi-temporal (MT) domain. Lastly, we produce the multi-temporal population grids (POP MT) by downscaling and re-allocating data derived from census surveys.

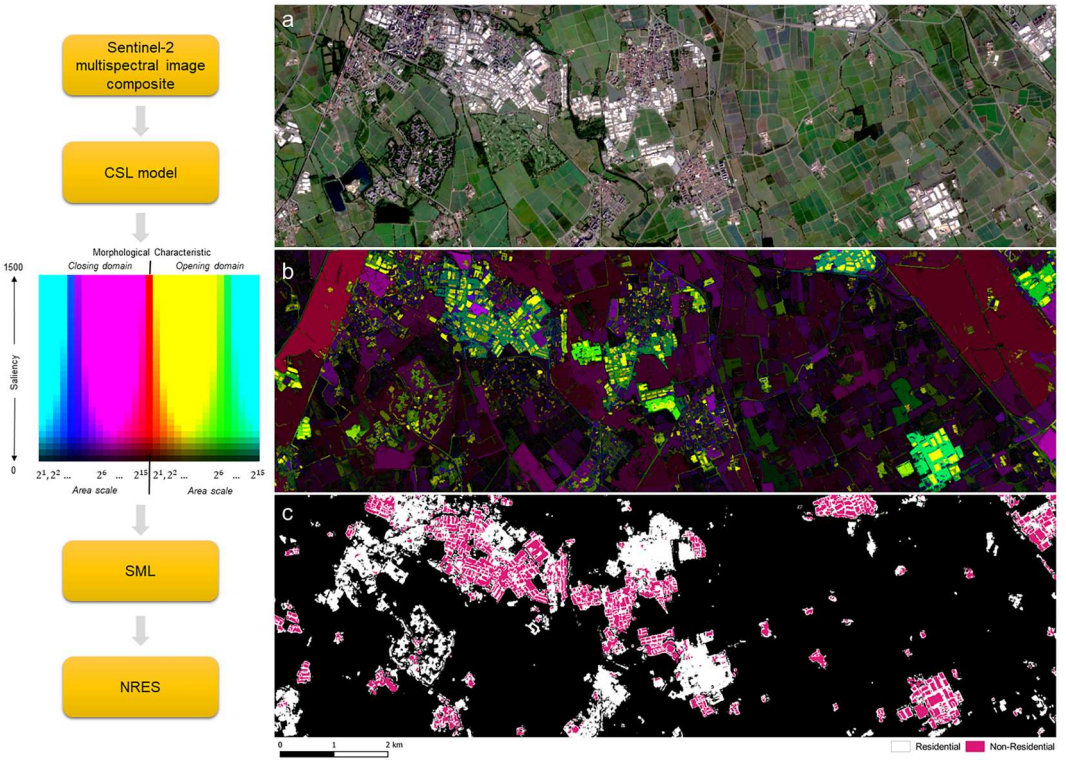

Figure 14. Illustrating the production of the NRES non-residential data. (a) sentinel-2 image composite, (b) derived multi-scale morphological decomposition of luminance by the CSL model, and (c) extracted non-residential built-up areas for a region south of Milan, Italy. The 'characteristic' and 'saliency' parts of the CSL response are mapped to the 'Hue' and 'Intensity, respectively, of the HIS color space for visualization purposes. Note that the NRES areas are a combination of image connected components with specific morphological characteristics.

4.3.1. Building height

Figure 15 shows the workflow of the BU_H module as a general multiple-objective ensemble model design. The main input data are two public global DEMs at 1 arcsec spatial resolution and the S2 image composite at 10 m resolution. The two DEMs are: optical-based Advanced Land Observing Satellite World 3D (AW3D30) (Tadono et al. 2014) and the radar-based Shuttle Radar Topography Mission (SRTM30) (Rabus et al. 2003). The reference years are 2000 for SRTM30, 2006-2011 for AW3D30, and 2018 for the S2CMP. Additionally, predictions of independent GHSL modules for the year 2018: fBU, fWATER, multi-temporal built-up surface changes 1975-2020 (BU-S MT), were used in various parts of the ensemble model.

The adopted solution for building height estimation leverages on the analytical relations between the Average of the Net Building Height (ANBH), the Average of the Gross Building Height (AGBH), the total building volume (BUVOL), and the fBU, as introduced in Pesaresi et al. (2021), and was organized in four parts. First, we predicted $ANBH_{DEM}$, $AGBH_{DEM}$ and $BUVOL_{DEM}$ with independent univariate regression models, built using a specific composite of morphological features extracted from the DEM data. The selection of the best morphological filter as predictor and the univariate regression coefficients were estimated based on experiments in six cities: Hong Kong, London, New York, San Francisco, Sao Paulo, and Toronto (Pesaresi et al. 2021). These parameters were kept constant at the global scale. Second, using the built-up surface predicted from the independent fBU, we reduced the simultaneous predictions of $ANBH_{DEM}$, $AGBH_{DEM}$ and $BUVOL_{DEM}$ by maximizing the single ANBH prediction, valid for the year 2010 (ANBH 2010) corresponding to the DEM source date.

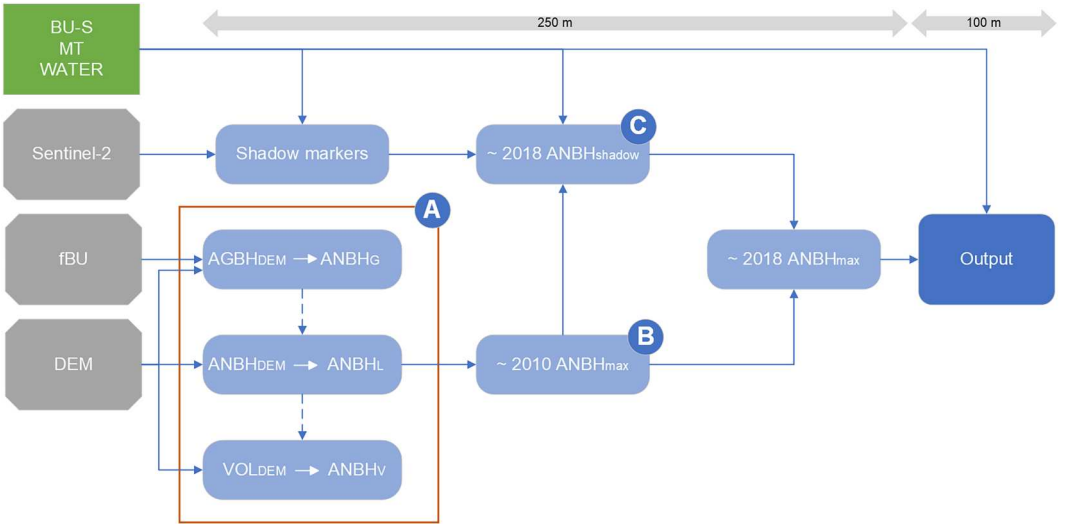

Figure 15. Schematic diagram of building height estimation.

Third, shadow markers used to predict the ANBH valid for the year 2018 (ANBH 2018) were extracted from the Sentinel-2 composite using radiometric and morphological filtering under the assumptions that shadows (i) are darker than the surrounding image connected components (thus detected by morphological area closing top hat), (ii) have high reflectance in the blue spectral range, relative to the luminance (Hollstein et al. 2016), and (iii) fWATER = 0 (Figure 16). The ANBH 2018 was estimated by linear regression: the coefficients were estimated locally in data tiles of 100 × 100 km, using the ANBH 2010 prediction as learning set, in the data domain considered stable after 2010, as derived from the BU-S MT module. The local estimation of regression coefficients allowed adjustment for the different illumination conditions at different latitudes, locally establishing associations between the size of the shadows and the height of the buildings. The above steps were employed at a spatial resolution of 250 m. Finally, the ANBH 2010 and the ANBH 2018 were fused by maximization and resampled to the 100 m grid, consistent with GHS-BUILT-H R2023 using lanczos2 interpolation method (Lanczos 1988). The maximization of the ANBH predictions as described above was carried out under the assumption of dominant negative bias in the ANBH predictions – an effect of using the low-resolution estimators from available input data (Goch et al. 2023; Pesaresi et al. 2021). A visual comparative example of urban expansion in Maoming city, China, post-2010, characterized by the emergence of high-rise buildings, is presented in the Appendix section L.3, titled 'On the ANBH model'.

Details of the methods used for ANBH production are described in the Appendix section E 'Building height (BU_H)'.

4.3.2. Multi-temporal built-up surfaces and volumes

The Multi-Temporal (MT) inferential engine of the GHSL framework it is made by two key components, namely MT_A, 'observation and interpolation', and MT_B, 'future extrapolation'.

MT_A is designed to predict a temporal persistence factor β^t of built-up surface with respect to the temporal endpoint, nominally $BU_S^t = \beta^t \cdot BU_S^{t=2020}$. β^t is predicted for each temporal point 't' of the GHSL at a 100 m spatial resolution. This prediction is based on the observation of the semantic Φ, extracted by SML from historical satellite images at various spatial resolutions (30, 80 m) and summarized at the same 100 m.

At the 100 m sample, the built-up volume BU_V^t is assumed to change proportionally to the observed change in β^t: $BU_V^t = \beta^t \cdot BU_V^{t=2020}$. The underlying assumption is that the Average Net

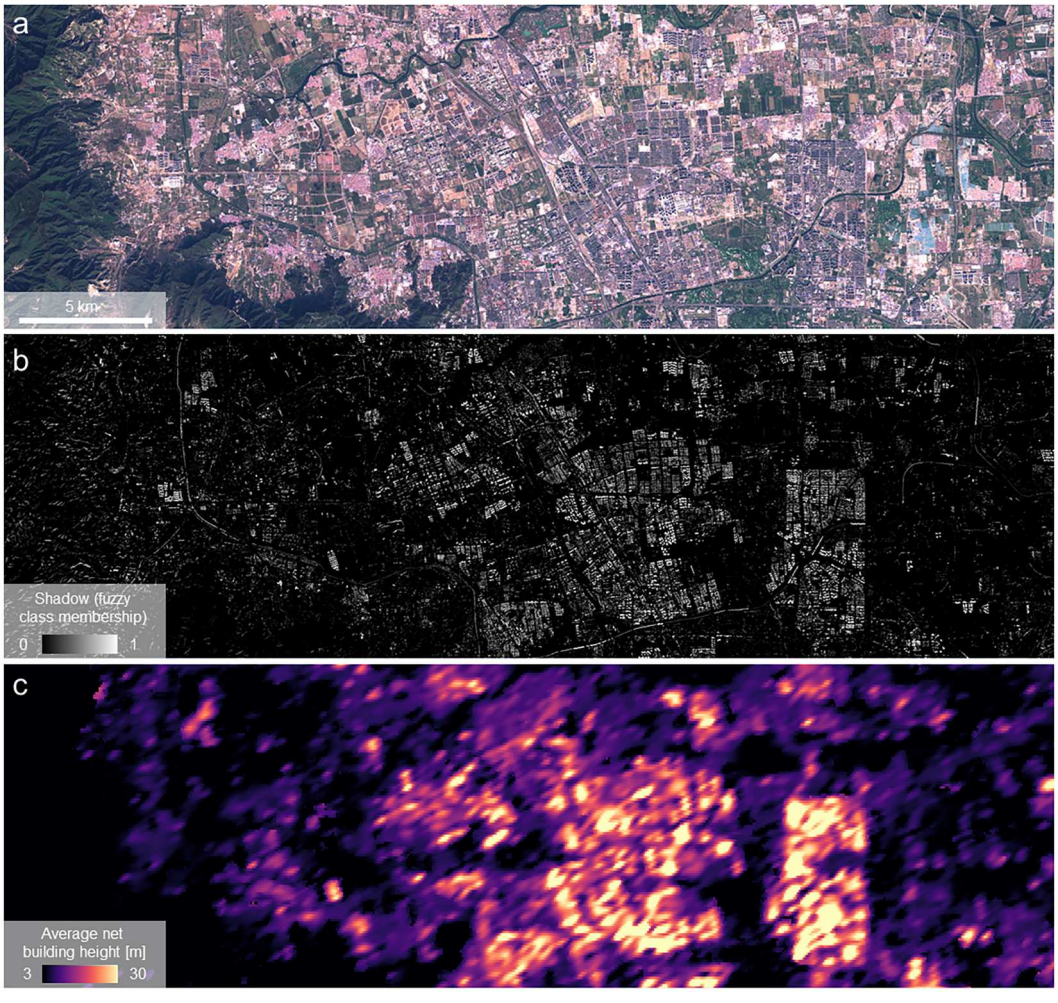

Figure 16. Illustrating the production of the GHSL building height information, show for a region in the north of Beijing, China. (a) sentinel-2 image composite, (b) shadow markers extracted from Sentinel-2 data, and (c) ANBH predicted at 100 m resolution.

Building Height (ANBH) in the 100 m sample remains constant over time. The logic applied to total built-up surface and volume was also applied to the non-residential component of built-up surface and volume. In this case, the assumption was that the share of RES vs NRES class in the 100 m sample remains constant over time.

MT_B was designed for directly predicting BU_S^t and BU_V^t for the near-future $t = \{2025, 2030\}$, independently for the built-up residential and non-residential components. The solution includes spatial rank-optimization and spatial pattern generative techniques to select the most probable samples to change state in the future by observation of past trends at the spatial grid level (100 m resolution) and at the processing data tile level (100×100 km) (Pesaresi et al. 2024).

The first GHSL MT_A internal prototype was developed in 2021 and designed as an unsupervised binary classifier, similar to previous β^t-based decision of BU switch-off was executed for all samples where $\Phi NBU > \Phi BU$, implying that the hypothesis that the sample belongs to the non-built-up background has more empirical support than the decision to maintain it in the built-up class. This prototype led to the GHSL R2022 release. Subsequent tests against independent data showed that this unsupervised mechanism generated an overestimate of change rates in scattered rural areas where the new Sentinel sensor was providing more thematic sensitivity compared

to the historical Landsat sensors. This shortcoming led to a new model development that resulted in the GHS-BUILT-S R2023 and GHS-BUILT-V R2023 releases.

The new BU-S MT model introduces two important innovations: (i) the continuous surface change prediction β^t and (ii) the integration of the Copernicus EO data at 10 m resolution in the information production system, facilitating gap filling, continuity, and repeatability of the proposed approach. The core of the method is an object-oriented image processing framework that implements a stratified multiple decision support approach to evaluate an ensemble of univariate linear regression predictions (Pesaresi et al. 2024). Those predictions are based on SML Φ semantics that are used to test the BU vs. NBU hypothesis and maximized along the time domain defined by the various satellite images collected since the 1975. The multiple-scene maximization of the Φ semantic allowed to minimize the influence of non-stationary noise in the image from cloud and other atmospheric noise/obstructions preventing the need of any other upstream cloud detector model and related parameters. The adopted design contributes to the robustness and stability of the proposed model, capable of handling scarce and spatially and temporally varying multiple-sensor input data. The resulting 100 m resolution spatial grids GHS-BUILT-S R2023, GHS-BUILT-V R2023 represent an unprecedented, continuous estimation of built-up surfaces and volumes between 1975 and 2030, in 5-year intervals, also distinguishing non-residential functional uses (GHS-BUILT-S-NRES R2023, GHS-BUILT-V-NRES R2023). The process for the new GHSL R2023 multi-temporal (MT) model development including extrapolation to 2025 and 2030 is described in (Pesaresi et al. 2024) and is summarized in the Appendix section F.

4.3.3. Multi-temporal population distribution grids

The GHS-POP R2023 are a spatial–temporal refinements of the geospatial population data originally collected and harmonized by CIESIN/SEDAC to produce the Gridded Population of the World layer, version 4.11 (GPWv4.11) (Center For International Earth Science Information Network - CIESIN - Columbia University 2018). CIESIN census data were used to estimate population time series by refining the population estimate model and revised through a set of control procedures. The resulting grids were assessed against official census gridded data (1 km) to compare the performance with previous GHS-POP products and other available global population products (see section 5.10).

The population time series estimates are based on census data and growth rates from the GPWv4.11. They incorporate multi-temporal information at country and city levels of the UN World Population Prospect (UN WPP 2022) and UN World Urbanization Prospect (UN WUP 2018) respectively, to improve local population hind cast. The model developed mitigates biases due to extreme or volatile growth rates by converging to the upper administrative level by 1950 and 2030, and to the WPP 2022 country growth rate in 100 years from census dates. The estimates were uniformly rescaled to match the total population at local 'city' level from the WUP 2018 and at country level from the WPP 2022. Local rescales were made by estimating WUP 2018 'city' boundaries from provided and revised point locations. The model merged adjacent administrative units to match the total population of the 'city' in the available census year (Schiavina, Melchiorri, and Freire 2023). The units within the estimated 'city' boundaries were rescaled according to WUP 2018 population figures, while all other units were rescaled to align the total country population with those reported in the WPP 2022. The estimated city boundaries matching WUP 2018 were released in the GHS P2023 data package. The performance of this approach was tested against available reference data (see Appendix section K.10).

Prior to downscaling, controls were enhanced to utilize EO information from GHSL (Freire et al. 2020). Census units' coastlines were adjusted to align with mapped built-up areas, and 'unpopulated' units were reassessed, leading to corrections in 269 units across 31 countries. This involved visual inspection of significant built-up surfaces in 2020 and, if residential built-up was confirmed, an automated method adjusted polygon geometry based on geographical proximity. The GHS-POP R2023 grids were created by downscaling resident population estimates per revised census unit,

informed by built-up layers (Freire et al. 2016). Several built-up layers were tested to determine the best predictor of population presence. Official population statistics from six countries were aggregated and downscaled to grids using different built-up layers (see Appendix section G). The residential built-up volume layer BU_V^{RES} was selected as the most suitable target layer for population downscaling, by assuming:

$$BU_V^{RES} = BU_V^{TOT} - BU_V^{NRES}$$

with BU_V^{TOT}: GHS-BUILT-V and BU_V^{NRES}: GHS-BUILT-V-NRES.

Each year, total resident population within each census unit was distributed to residential built-up cells, proportionally to the residential built-up volume share in the unit. This method is suitable for policy support due to its clarity, reproducibility, and improved representation of resident population. For methodological details see Appendix section G. Visual comparative examples of GHS-POP are provided in the Appendix section L.4, for the following regions: rural Africa (L.4.1), rural Brazil (L.4.2), urban China (L.4.3), and a region East of Al-Mafreq, Jordan (L.4.4).

4.4. Human settlements classification

The GHSL spatial taxonomies (Tambassi 2018) serve as a tool to distill complex human settlement information from various sources. This process transforms the raw data into a more manageable and understandable semantic schema. This simplification makes the data more accessible and enhances its interpretability, thereby facilitating its application across a range of contexts. The Morphological Settlement Zone (MSZ), the Built Type classification, (BUTYPE), and the settlement model (SMOD) implementing the Degree of Urbanization (DEGURBA) classification are placed in the lower, intermediate, and top level, respectively, of the GHSL HAMM (Figure 4). It is important to highlight that the GHSL taxonomies are produced by applying static rules to the baseline GHSL data. This process explicitly reveals the assumptions inherent in these taxonomies. Therefore, the approach here is fundamentally deductive, with no inductive inference applied.

4.4.1. Morphological settlement zone

The Morphological Settlement Zone (MSZ) concept uses the salient points of the fBU function or 'markers' (M_{BU}) and integrates various GHSL data (Figure 17). M_{BU} are defined as the local

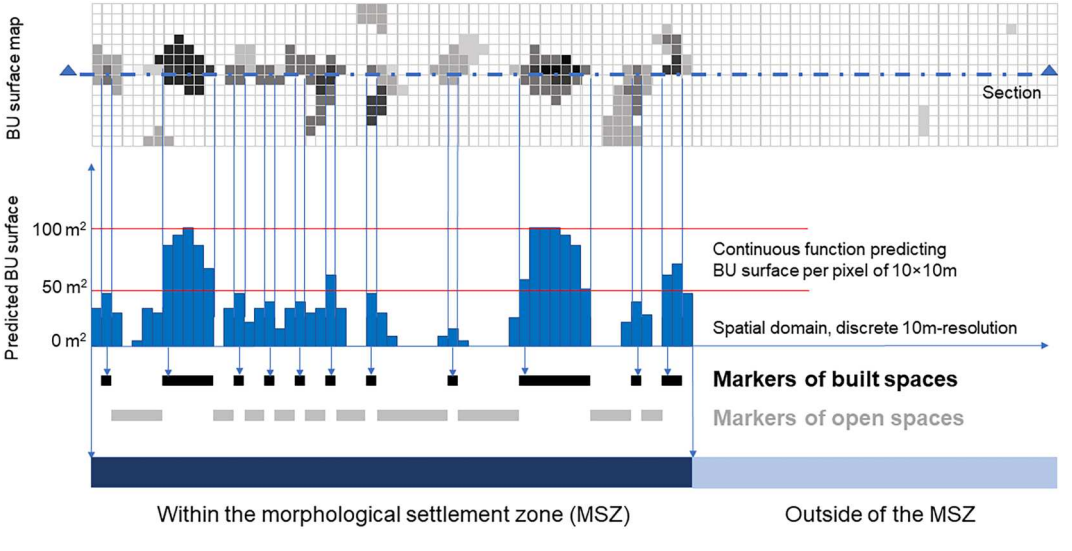

Figure 17. Schematic diagram of the concept of the Morphological Settlement Zone.

Figure 18. Delineation of the MSZ in the region of Padova and Venice (Italy) by the union of 'compact' or 'sparse' settlement domains. (a) the 10 m resolution fBU function extracted from Sentinel2 imagery, and (b) the fBU-derived discrimination between 'compact' vs. 'sparse' settlement patterns supporting the MSZ. Only the compact settlements were gap-filled.

maxima of the fBU function or samples where fBU > 50%. A 10 m resolution MSZ is achieved by applying morphological filtering to the fBU function markers, guided by deductive inference and an unsupervised classification process. The goal is to aggregate nearby built-up structures, including open spaces within the MSZ, while avoiding large unbuilt areas in sparse settlements. The process distinguishes between 'compact' and 'sparse' settlement patterns, filling gaps only in compact settlements (Figure 18). After delineation, a hierarchical approach characterizes the MSZ, prioritizing markers associated with built-up (M_{BU}), open space (M_{NBU}), and water surfaces. M_{BU} is characterized by merging FUN and BU-H modules, using NRES classification and ANBH values. Open spaces are classified using GHS-LAND R2022 land surface information, MAX-NDVI from Sentinel-2 image data, and OSM highway surfaces. A hierarchical per-pixel approach is adopted for MNBU domain classification, considering highway set, land surface dominance, and water surfaces. The resulting MSZ taxonomy (Figure 19) includes a nomenclature describing open and built-up spaces (Table 3).

4.4.2. Built typology

The BUTYPE classification process uses three input modules: land vs. water fraction (fWATER), functional classification (FUN), and building height (ANBH) from the BU-H module, aligned with Sentinel-2 image data. The process includes defining a built domain (fBU > 0), classifying it into RES and NRES categories, estimating the number of floors by rounding the ratio of ANBH to 3, categorizing them, and classifying samples outside the built domain. The goal is to summarize characteristics like construction technology, invested capital, urban density, and living conditions. Single-family homes, typically one or two stories high, are prevalent in suburban areas and informal settlements, often owner-built and occupied. Multi-family homes, three or more stories high, are categorized into walk-up apartments (3-7 floors class) and high-rise buildings (8 + floors class). These require financing, are not self-built, and often built for rental. The key difference lies in

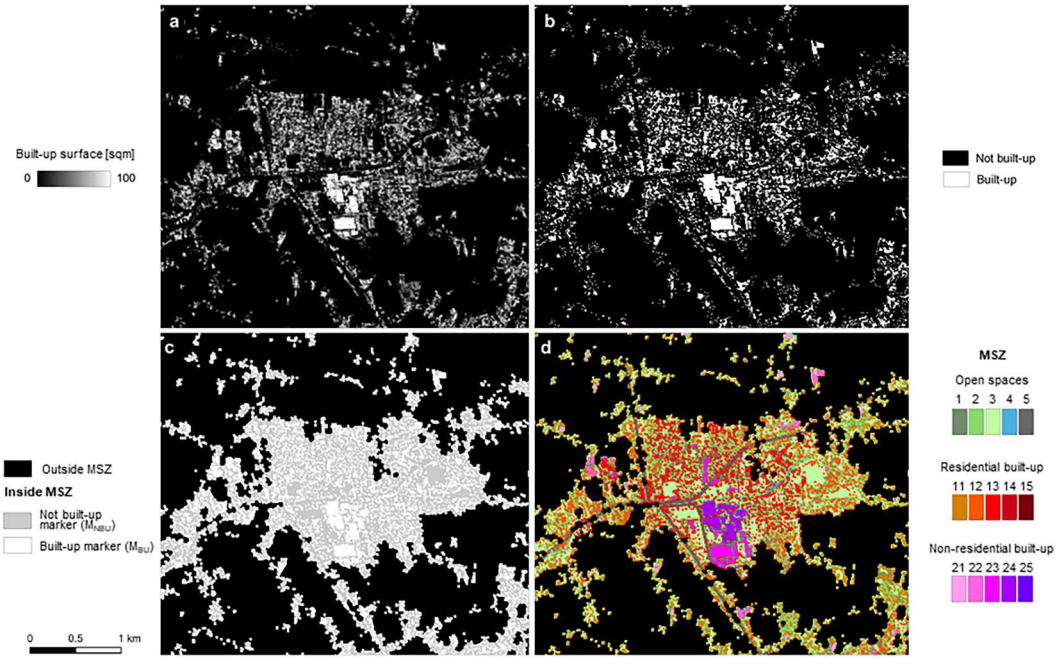

Figure 19. Anatomy of the MSZ taxonomy in the town of Mira (Venice, Italy). (a) the fBU extracted from Sentinel-2 imagery, (b) the salient BU markers (M_{BU}) extracted from the continuous fBU, (c) the delineation of the MSZ by spatial generalization of the M_{BU} using open-closing alternate morphological filtering and gap filling of compact settlements, (d) characterization of the MSZ inner domain by integrating various GHSL information. The legend of the MSZ taxonomy is the same as in the Figure 6.

Table 3. Morphological Settlement Zone taxonomy.

MSZ code	Taxonomy
00	Outside the MSZ domain
01	MSZ, open spaces, low vegetation surfaces NDVI $\leq$ 0.3
02	MSZ, open spaces, medium vegetation surfaces 0.3 < NDVI $\leq$ 0.5
03	MSZ, open spaces, high vegetation surfaces NDVI > 0.5
04	MSZ, open spaces, water surfaces LAND < 0.5
05	MSZ, open spaces, road surfaces
11	MSZ, built spaces, residential, building height $\leq$ 3 m
12	MSZ, built spaces, residential, 3 m < building height $\leq$ 6 m
13	MSZ, built spaces, residential, 6 m < building height $\leq$ 15 m
14	MSZ, built spaces, residential, 15 m < building height $\leq$ 30 m
15	MSZ, built spaces, residential, building height > 30 m
21	MSZ, built spaces, non-residential, building height $\leq$ 3 m
22	MSZ, built spaces, non-residential, 3 m < building height $\leq$ 6 m
23	MSZ, built spaces, non-residential, 6 m < building height $\leq$ 15 m
24	MSZ, built spaces, non-residential, 15 m < building height $\leq$ 30 m
25	MSZ, built spaces, non-residential, building height > 30 m

their construction, ownership, and purpose. Table 4 presents the final BUTYPE class abstraction list (Figure 20).

4.4.3. The settlement model and the degree of urbanization

The GHS Settlement Model (SMOD) and Degree of Urbanization Classification (DUC) implement the two-stage DEGURBA method within the GHSL framework (see Appendix section J). GHS-SMOD identifies settlement classes using population density grids, while GHS-DUC characterizes territorial units by their urbanization degree. GHS-SMOD is at the apex of the GHSL HAMM for

Table 4. Built Typology classification.

BUTYPE class	Taxonomy
00	outside the BU > 0 domain and WATER surface dominant
01	outside the BU > 0 domain and LAND surface dominant
11	residential or mix prevalent 1-2 floors
12	residential or mix prevalent 3-7 floors
13	residential or mix prevalent 8 + floors
21	exclusive non-residential prevalent 1-2 floors
22	exclusive non-residential prevalent 3-7 floors
23	exclusive non-residential prevalent 8 + floors

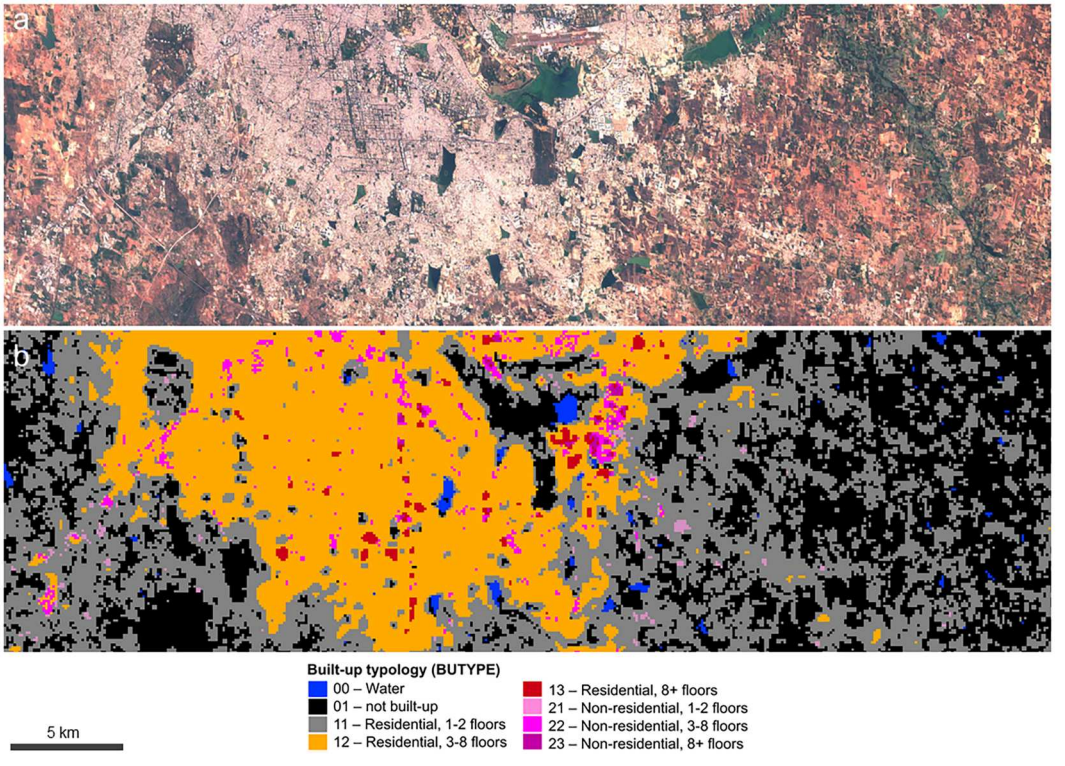

Figure 20. BUTYPE taxonomy for a region in the East of Bengaluru, India. (a) sentinel-2 image composite, and (b) derived BUTYPE taxonomy.

spatial information production and was produced at the largest spatial aggregation of the GHSL raster data (1 km resolution). The rural-urban continuum classes are defined using a combination of resident population density or built fabric density observed at 1 km resolution, along with the population size of the settlement (Dijkstra et al. 2021). GHS-DUC classifies territorial units by applying DEGURBA second stage based on GHS-SMOD for each GHSL epoch (see Appendix section J.3). The resulting classification and statistics (GHS-DUC R2023) assist in disaggregating several indicators by DEGURBA, such as Sustainable Development Goals (SDGs), Gallup World Poll, and similar monitoring efforts available by administrative level. SMOD produces boundaries of urban centers for each GHSL epoch, linked over time with the Multi-Temporal dynamics of the Urban Centers (MTUC, see Appendix section J.2). MTUC aids in studying city evolution, demographic shifts, and socio-economic factors. It tracks population changes and the spatial dynamics of city boundaries, identifying entities that grow, shrink, split, merge, or appear/disappear over

time. This allows for a detailed analysis of urban growth and contraction, offering valuable insights into urban development patterns.

5. Validation and comparative assessment

In this section, we validate the low and medium abstraction levels of GHSL information. Our approach is multifaceted (Table 5), involving different types of reference data:

- Human Visual Inspection of imagery (HVI_REF): This involves extensive visual inspection of EO imagery (Figure 21, Figure 22);
- Vector Building Footprint reference data (BF_REF): This is an ensemble of vector building footprint data generated from various sources, organized in data blocks of 25 km. It is partially enriched with information about the year of construction and height of buildings, extracted from propriety data and/or cadastral data (Figure 23, Figure 24);
- Authoritative Gridded Population Counts (POP_REF): These are detailed population counts released by official sources.

These reference data were not used or did not exist during the production of the GHSL R2023A, were independently compiled, and were assumed to be more accurate than the GHSL data, with some limitations.

Besides validation, we also carried out a comparative assessment of the GHS-POP and GHS-BUILT. The assessment includes the following models and their outputs: GHS-POP R2023, GHS-POP R2022, GHS-POP R2019 (GHS-POP versions released in 2023, 2022, 2019), WPC – 'WorldPop UN adjusted constrained' – (Bondarenko et al. 2020), and WPU – 'WorldPop UN adjusted unconstrained' - (WorldPop 2018). The comparative assessment of GHS-BUILT targets alternative global models/products that derive similar information from Earth Observation (EO) data and comply with a policy of complete transparency and unrestricted access (Table 5). Despite its relevance, the Global Urban Footprint (Esch et al. 2013) was excluded from the test due to the lack of agreement between the data producer and JRC. To track the progress of GHSL developments over time, we included internal GHSL prototypes.

5.1. Reference data and test sampling schema

5.1.1. Human visual inspection of imagery

Human visual inspection reference data (HVI-REF) comprises two sources: the HVI-REF_S2 and the HVI_REF_VHR. The first is an extensive visual inspection of the same Sentinel-2 images used in the GHSL production process (Figure 21). This inspection was conducted by independent professional photo interpreters from a team of nine in a three-fold assessment of a globally-representative set of one million samples as part of the Copernicus Emergency Management validation services (Melchiorri 2024). The second was created by visually inspecting a globally-representative set of 50 000 samples of Very High Resolution,VHR, images in an open crowd-sourcing framework (See et al. 2022). Both sources employ distinct sampling and visual interpretation schemas, making them complementary. The HVI_REF_S2 sampling was conducted using a spatially uniform, equalized random procedure (see Appendix section K.1.1). This aimed to identify an equal number of 10 m resolution test samples in each class, on the exact spatial grid that supports Sentinel-2 data. Four classes were considered: non-built-up land (NBU_LAND), non-built-up water (NBU_WATER), built-up residential (BU_RES), and built-up non-residential (BU_NRES). These classes were obtained from the dominant surface component of the GHSL continuous surface predictions. Each test location was inspected by three randomly chosen photo- interpreters, to minimize interpreter-induced systematic bias. HVI_REF_VHR (see Appendix section K.1.2) was sampled

Table 5. The comparative model set in EO-derived information assessment, in alphabetical order, with indication of the performed test. 'C 10 m' is the test on categorical land use / land cover class at 10 m resolution, 'BU_S 10 m' is the test on continuous sub-pixel surface fraction at 10 m resolution, and 'BU_S 80 m/100 m' is the test on the continuous built-up surface at 80 or 100 m resolution. The 'BU_S MT 100 m' is the test on the multi-temporal, continuous built-up surface at 100 m resolution, while the 'BU_H 100 m' is the test on average building height at 100 m resolution. The label 'X' indicates that the given model/product was included in the specific test.

Model	Reference	C 10 m	BU_S 10 m	BU_S 80 m / 100 m	BU_S MT 100 m	BU_H 100 m
ALOS_30 m (2023)	(He et al. 2023)					×
CGLC (2020)	Copernicus Global Land Cover (Buchhorn et al. 2020)			×		
DYNAMICWORLD (2022)	(Brown et al. 2022)	×		×		
ESRI (2018)	(Karra et al. 2021)			×		
ESRI (2020)	(Karra et al. 2021)			×		
FROM_GLC10 (2019)	(Gong et al. 2019)			×		
FROM_GLC30 (2013)	(Gong et al. 2013)			×		
GAIA (2020)	(Gong et al. 2020)			×	×	
GAUD (2020)	(Gong et al. 2020; Liu et al. 2020)			×	×	
GHS-BUILT (2017)	(Corbane et al. 2017)			×		
GHS-BUILT R2016	Public GHSL release (Pesaresi et al. 2016b)			×	×	
GHS-BUILT R2019	Public GHSL release (Corbane et al. 2019)			×	×	
GHS-BUILT-M (2015)	Internal GHSL prototype 2015, documented in (Pesaresi et al. 2016b)			×		
GHS-BUILT-*P* (2015)	Internal GHSL prototype, documented in (Pesaresi et al. 2016b)			×		
GHS-BUILT-*P* (2019)	Internal prototype supporting the GHSL R2022 and R2023 model development, documented in this manuscript		×	×		
GHS-BUILT-*P* (2020)	(Corbane et al. 2021)		×	×		
GHS-BUILT-H R2023	Public GHSL release (Pesaresi and Politis 2023b)					×
GHS-BUILT-S R2023 E1975-2020	Public GHSL release (Pesaresi and Politis 2023b)				×	
GHS-BUILT-S R2023 E2015	Public GHSL release (Pesaresi and Politis 2023b)			×		
GHS-BUILT-S R2023 E2018	Public GHSL release (Pesaresi and Politis 2023b)	×	×			
GHS-LAND-S R2022 E2018	Public GHSL release (Pesaresi and Politis 2022)	×				
GHS-BUILT-S R2023 E2020	Public GHSL release (Pesaresi and Politis 2023b)			×		
GHSL (2016)	Internal prototype documented in (Pesaresi et al. 2016b)					×
GHSL (2021)	Internal prototype documented in (Pesaresi et al. 2021)					×
GISA10 (2022)	(Huang et al. 2022b)	×		×		
GISAv1 (2021)	(Huang et al. 2021)			×		
GISAv2 (2022)	(Huang et al. 2022a)			×		
GISD (2022)	(Zhang et al. 2022)			×	×	
$GLOBE_{LAND30}$ (2014)	(National Geomatics Center of China 2014)			×		
MODIS (2010)	(Schneider, Friedl, and Potere 2010)			×		
S1_1 km (2022)	(Li et al. 2022)					×
S1_500 m (2022)	(Zhou et al. 2022)					×
WORLDCOVER (2021)	(Zanaga et al. 2022)			×		
WSF2015v1 (2020)	(Marconcini et al. 2020)	×		×		
WSF2015v2 (2023)	(German Aerospace Center (DLR) 2023)	×		×		
WSF2019 (2021)	(Marconcini et al. 2021)	×		×		
WSF3D (2022)	(Esch et al. 2022)					×
WSFEVO (2021)	(Marconcini et al. 2021)			×	×	

using a globally representative set of 50 000 test locations (Figure 22), collected using a stratified uniform random schema and was designed to facilitate comparison across different model predictions (See et al. 2022). The test data were crowdsourced, using multiple VHR image data available in

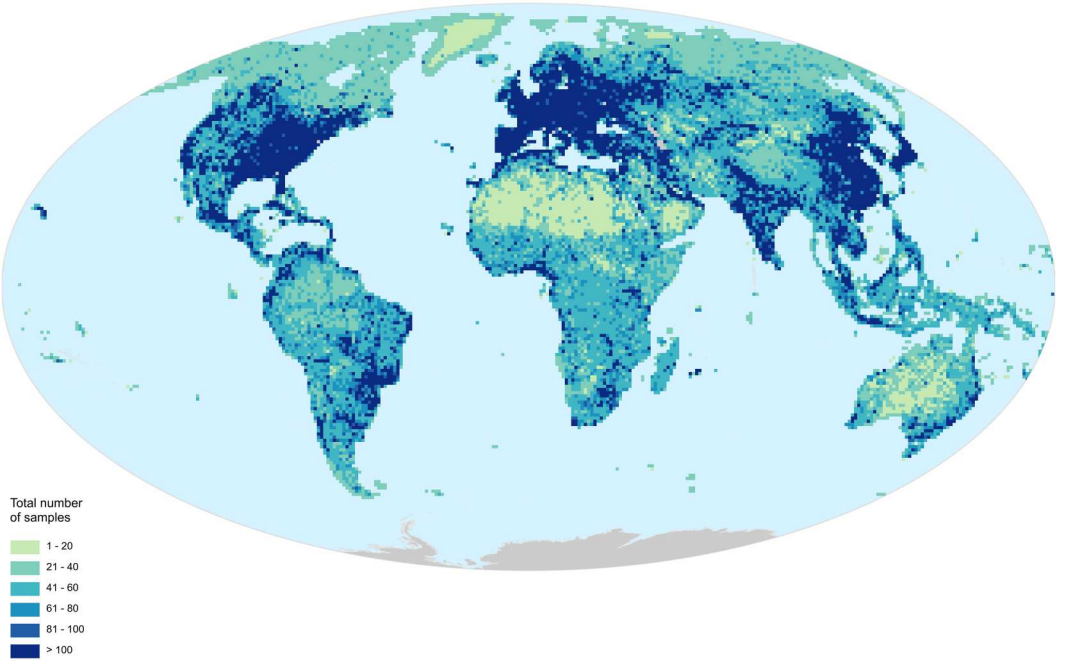

Figure 21. Geographical distribution of total test samples collected in the HVI_REF_S2 in the four classes NBU_LAND, NBU_WATER, BU_RES, BU_NRES, per each sentinel-2 data tile of 100 × 100 km.

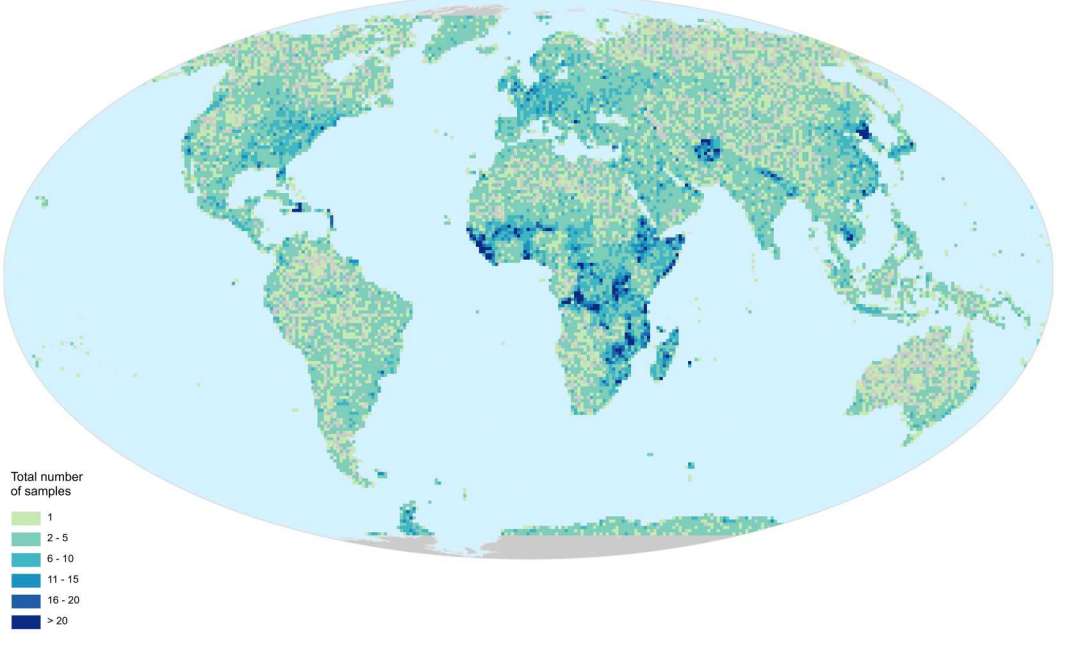

Figure 22. Geographical distribution of 'box' test samples from the HVI_REF_VHR dataset for each 100 × 100 km Sentinel-2 data tile. Each 80 × 80 m 'box' sample comprises 64 sub-samples, each measuring 10 × 10 m of spatial resolution.

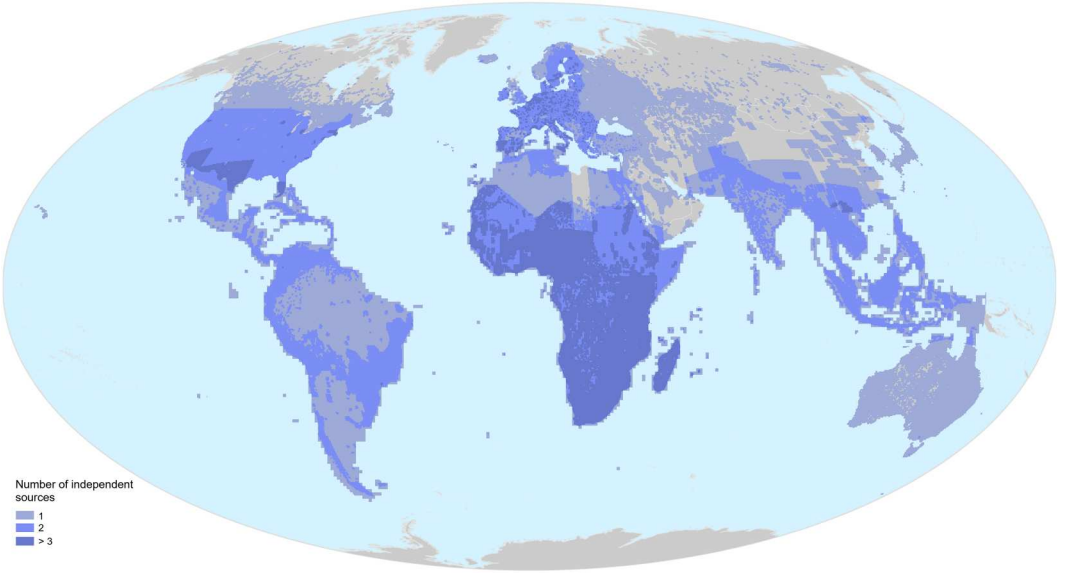

Figure 23. Representation of the BF_REF data universe, encoded by the number of independent sources available per 25 km data block.

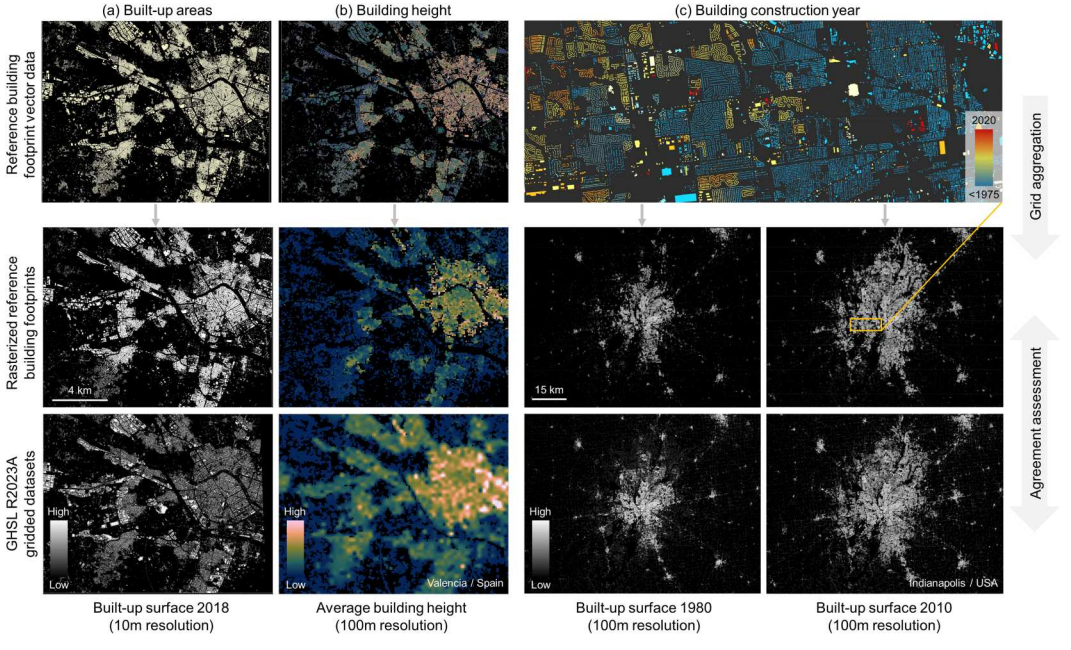

Figure 24. Illustrating the validation concept of the GHSL data products using attributed, automatically generated or cadastral building footprint data BF_REF, providing accurate estimates of (a) built-up surface, and attributed with (b) building heights, and (c) construction year information, for evaluation built-up surface, height, and built-up surface over time, respectively. Left, the city of Valencia (Spain) and right, the city of Indianapolis (USA).

Bing or Google as a reference. To address spatial inconsistency and parallax distortion in VHR images, a sample size of 80 × 80 m in the local UTM grid geometry was established. For each sample, the interpreter filled a matrix of 64 sub-samples, each measuring 10 × 10 m, answering 'yes' or 'no' to

the question: 'Is the sub-sample built or not?' The result is a quasi-continuous test data set with 65 possible values (0-64), quantifying the composite sum of built-up (BU) sub-samples.

5.1.2. Vector building footprint data

Building footprint reference data (BF_REF) includes vector data exported by GIS services of national or local administrations (see Appendix section K.1.3). It also predominantly includes data derived from the automatic vectorization of VHR images or machine-learning building footprints (MLBF), recently produced by Google[13], Microsoft[14], or the Gates Foundation.[15] BF_REF was enriched by integrating other sources that assess the year of construction, as in the case of the Microsoft-ZTRAX integrated data made for the US by the co-authors (Uhl and Leyk 2022c). To control the spatial variability of the accuracy measures, the BF_REF data was prepared in blocks of 25 × 25 km size, using the same GHSL grid geometry. Thus, the BF_REF block is the basic unit of the test. If more than one reference source assess the same test block, then each source supports an independent test (Figure 23). First and second-order statistics were derived from the distribution of the block-level tested accuracy performances. Therefore, the ensemble of the different sources supporting BF_REF contributes to the final assessment discussed here (see Appendix sections K.5, K.6, and K.7). While the correctness of the BF_REF is assumed to be high (Gonzales 2023) as compared to the information derived form 10 m resolution imagery, the completeness, semantic consistency, spatial accuracy, spatial agreement with the GHSL baseline raster grid, and temporal alignment are often unknown. Therefore, we implemented mitigation measures to reduce potential biases, inaccuracies, and uncertainties in the test. In the BF_REF assessment, the spatial domain of the test is defined as: $TD^t = (A \cap C^t) \cup B$, with A being the generalized reference built-up positive domain where the BF_REF > 0 in a spatial neighborhood of 100 meters size, and B being the agreement zero domain defined as the domain where the majority of the models under test predict zero built-up surface. The temporally bounded C^t is the domain, where the built-up surface is constant after the year 't' as derived by the GHSL prediction $BU_S^{2020} - BU_S^t = 0$. The above formulation limits the influence of the BF_REF incompleteness and unknown precise update in the 100 m neighboring area, including a positive evidence in the reference data. When $t < 2020$, an additional requirement regarding the temporal stability of the built-up surface under test is enforced. Finally, only samples with complete and valid data were included in the BF_REF test. Furthermore, BF_REF blocks, with a minimum support of 1 000 valid samples, were incorporated into the assessment to ensure that the test is representative. In this study, both the HVI_REF and the BF_REF have been stratified to facilitate a more comprehensive understanding of error and accuracy patterns. Specifically, we stratified by world region and by income classification. These classifications are derived from the UN Sustainable Development Goals region[16] (UN-SDG-Region) and the World Bank income classification[17] (WB-Income), respectively.

Table 6 shows the distribution of the 10 m resolution samples in the HVI_REF_S2, categorized by sampled class and by WB-income class. The total number of samples per WB-income region approximates the surface area of the regions, a result of the spatially uniform random sampling schema applied. The total number of samples in each class remains constant, a characteristic of the equalized sampling approach used.

Table 7 presents the number of HVI_REF_VHR samples collected via crowd sourcing, categorized by WB-Income class. These samples fall into two classes: BU = 0 and BU > 0. Their relative

Table 6. Number of 10 × 10 m samples supporting the HVI_REF_S2 by sampled class and WB-Income class.

WB-income class	BU_NRES		BU_RES		NBU_LAND		NBU_WATER		Total	
High Income	96162	38.5%	63564	25.4%	76124	30.4%	42541	17.0%	278391	27.8%
Upper Middle	106570	42.6%	104032	41.6%	101187	40.5%	82940	33.2%	394729	39.5%
Lower Middle	39005	15.6%	53419	21.4%	45599	18.2%	26812	10.7%	164835	16.5%
Low Income	6433	2.6%	27358	10.9%	23294	9.3%	14846	5.9%	71931	7.2%
N/A	1830	0.7%	1627	0.7%	3796	1.5%	82861	33.1%	90114	9.0%
Total	250000	100.0%	250000	100.0%	250000	100.0%	250000	100.0%	1000000	100.0%

Table 7. Number of 80 × 80 m samples supporting the HVI_REF_VHR by sampled class and WB-Income class.

WB-income class	BU = 0		BU > 0		Total	
High Income	10031	22.2%	1505	32.8%	11536	23.2%
Upper Middle	11931	26.9%	1208	25.6%	13139	26.8%
Lower Middle	5295	11.7%	648	14.1%	5943	11.9%
Low Income	12157	26.4%	1178	26.3%	13335	26.4%
N/A	5821	12.9%	54	1.2%	5875	11.8%
Total	45235	100.0%	4593	100.0%	49828	100.0%

Table 8. Distribution of BF_REF 25 km data blocks across World Bank income classes, utilized in various tests.

WB-income class	BF_REF		TEST: BU_S 10 m		TEST: BU_S 100 m		TEST: BU_S MT 100 m		TEST: BU_H 100 m	
High Income	72866	24.0%	14972	15.7%	16354	19.9%	7748	99.9%	15499	96.1%
Upper Middle	95366	31.4%	30745	32.3%	24737	30.0%	6	0.1%	606	3.8%
Lower Middle	73839	24.3%	29894	31.4%	26570	32.3%	N/A	0.0%	23	0.1%
Low Income	61686	20.3%	19464	20.5%	14659	17.8%	N/A	0.0%	N/A	0.0%
Total	303757	100.0%	95075	100.0%	82320	100.0%	7754	100.0%	16128	100.0%

occurrence is determined by the expected land cover probability, based on prior information (See et al. 2022).

Table 8 presents the volume of BF_REF data used, sorted by WB-income regions. The data is further broken down for each supported test. Specifically, the static built-up surface tests at 10 and 100 m resolutions ('BU_S 10 m' and 'BU_S 100 m', respectively), the multi-temporal built-up surface test at 100 m resolution ('BU_S MT 100 m'), and the average building height test at 100 m resolution ('BU_H 100 m') are detailed separately. Different tests impose varying requirements on the valid data domain, leading to a reduction in the total availability of BF_REF. Section 5.5 provides a detailed description of the 'BU_S 10 m' test, which is elaborated in Section 5.7. Further, the 'BU_S MT 100 m' and 'BU_H 100 m' tests are discussed in Sections 5.8 and 5.9, respectively. It should be noted that due to the uneven availability of BF_REF attributes, such as building height and construction epoch, the 'BU_S 10 m' and 'BU_S 100 m' tests offer a more geographically balanced representation. In contrast, the 'BU_S MT 100 m' and 'BU_H 100 m' tests mostly cover high-income countries.

5.1.3. Authoritative gridded population counts

The POP_REF data are organized into seven test cases (see Appendix section K.1.4): 1. Brazil, 2. Ecuador, 3. a subset of 18 European countries within the GEOSTAT grid, 4. Finland, 5. Japan, 6. Mexico, and 7. Korea. The test data consist of 1 km vector grids reporting the total resident population, produced by National Statistical Institutes, used to benchmark modeled grids. Table 9 shows the characteristics of the POP_REF data supporting the GHS-POP validation.

5.2. Accuracy measures

The accuracy measures adopted in this study are the Jaccard similarity index (Jaccard 1901) and the Ružička similarity index (Ružička 1958), R-accuracy, applied to evaluate the discrete and the continuous raster domains, respectively (Krasnodębska et al. 2024). In addition to the R-accuracy measure, we assessed the mean absolute error (MAE) and Root Mean Square Error (RMSE) at pixel level, and the Total Allocation Accuracy percentage (%TAA) (Batista e Silva et al. 2020) was applied for the evaluation of population grids.

5.3. Comparative assessment

Results of the comparative assessment show that the GHS-BUILT R2023 model excels in differentiating between built-up and non-built-up areas (Figure 25a), and notably in distinguishing between land

Table 9. GHS-POP R2023 grid (CIESIN/SEDAC input polygons) and reference layers (gridded census data for 24 countries). PwArea refers to the population weighted area. EU18 is a subset of 18 countries in the GEOSTAT grid, where reference data do not have privacy control (see Appendix section K.1.4).

	GHS-POP input data				Reference data		
Country	Census year	Admin (Admin level)	Populated units	PwArea (km^2)	Census years	Units	Cell size (km^2)
Brazil	2010	Sector (5)	310 046	17.3	2010	8 860 553	1
Ecuador	2010	Town (3)	1 047	582.5	2010	516 555	1
EU18	2009-2014	Varying	322,029	140.8	2011, 2021	3 255 93	1
Finland	2011	Municipality (2)	320	978.8	2005-2020 5yrs	352 885	1
Japan	2010	Municipality (2)	1 750	308.3	1995-2020 5yrs	501 600	1
Mexico	2010	AGEB (3)	68 476	25.2	2020	1 966 93	1
Republic of Korea	2010	District (2)	251	251.2	2000-2020 10yrs	107 661	1

and water (Figure 25b) at a 10 m resolution. It is the most accurate predictor of continuous built-up surfaces at a 100 m resolution in the static test domain, $TD^{t=2010}$ (Figure 25c), and in the full multi-temporal domain (Figure 25d). Finally, it excels in predicting the average height of buildings at a 100 m resolution, both in the static test domain, $TD^{t=2010}$ and the entire test domain $TD^{t=2020}$.

5.4. Evaluating the categorical land use / land cover classes at 10 m resolution

The 'C 10 m' test is based on 442 292 test locations extracted from the HVI_REF_S2, corresponding to the samples where both full agreement and high confidence were reported by the interpreters. In the 'C 10 m' test, the GHSL yields a mean IoU of 0.87 across all four classes[18] an IoU of 0.92 for distinguishing between built-up and non-built-up, an IoU of 0.8 to predict residential and non-residential built-up classes, and an IoU of 0.98 in separating water from land. In the 'urban' stratum, as

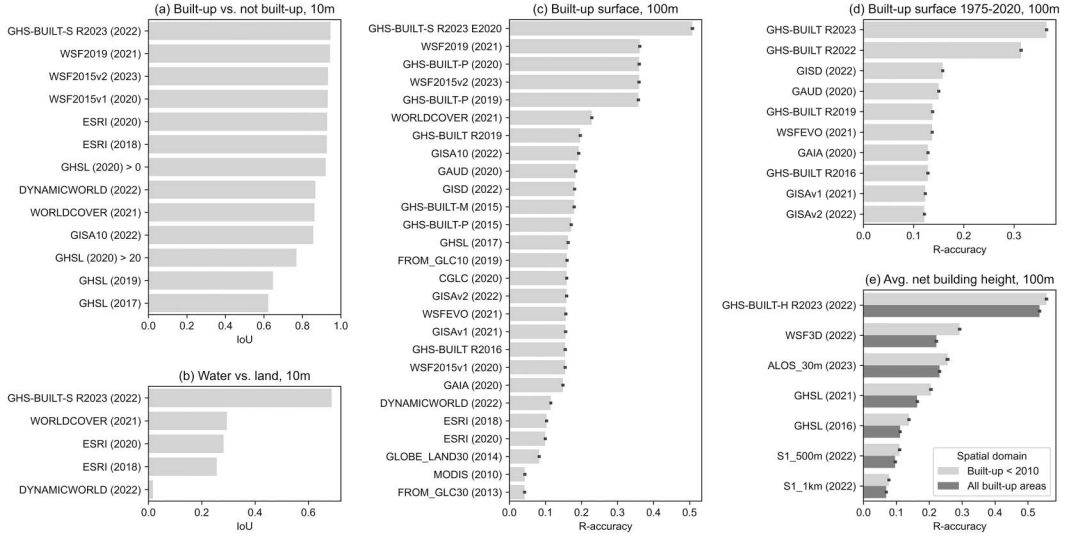

Figure 25. Summary of the comparative accuracy assessment on the EO-derived GHSL information. Jaccard similarity or Intersection over Union (IoU) of categorical BU vs. NBU (a) and WATER vs. LAND (b) classification in the URBAN stratum defined by the Copernicus Global Land Cover at 100 m resolution. R-accuracy in predicting the quantity of built-up surface at 100 m resolution, in (c) static and (d) multi-temporal assessment. (e) R-accuracy in predicting average of the net building heights at 100 m resolution in two temporal strata: stable 2010 domain (built-up < 2010), and all the built-up domain.

defined by the 100 m resolution Copernicus Global Land Cover, the GHSL improves the discrimination of the built-up vs. non-built-up class among the seven best available layers considered in the test. It is over twice as accurate in the land vs. water discrimination, compared to the best performer, WORLDCOVER (2021). This latter achievement is very important, as the detection of water surfaces in the urban environment it is a known issue that limits the applications of EO in disaster management (see Appendix section K.4)

5.5. Evaluating 10 m resolution sub-pixel built-up surface fraction

The 'BU_S 10 m' test, based on 95 210 BF_REF data blocks, was co-registered with Sentinel-2 image data globally (Table 8). Co-registration operated only on the spatially uniform domain, ignoring non-stationary grid misalignment due to parallax distortion, relevant in urban environments with high-rise buildings. Post co-registration, the average residual spatial disagreement between satellite and REF data was half a pixel (4.9 meters), explaining the reduced R-accuracy performance. Analysis of spatial misalignment between BF_REF and satellite imagery, while relevant for accuracy measures, is beyond the scope of this study. The comparative assessment included only global continuous models predicting built-up surfaces at a 10 m resolution. The built-up class probability was tested for GHS-BUILT-P (2020), GHS-BUILT-P (2019), and DYNAMICWORLD (2022), see Table 10.

In the 'BU_S 10 m' test, GHS-BUILT-S R2023 yields the highest R-accuracy in each WB-income region, with an overall R-accuracy of 0.23 and a Mean Absolute Error (MAE) at the grid cell level of 7.1 m^2. The receiving-operator-curve (ROC) analysis revealed that the best cut-off value maximizing the IoU for predicting $fBU_{REF} > 0.5$ is $BU_S > 41$ at 10 m resolution. These overall findings vary across regions and income levels (see Appendix section K.5).

5.6. Evaluation of built-up surface vs. crowd-sourced reference data

The 'BU_S 80 m' test was supported by the HVI_REF_VHR data. The total built-up surface measured by global models, within 48 884 valid blocks of 8×8 grid cells (10 m) was compared to crowd-sourced reference data by Spearman rank correlation (Table 11). WSF2015v2 (2023), WSF2019 (2021), and GHS-BUILT-S R2023 E2018 provides similar results, with the latter top-ranking scoring 0.85 of correlation. Notable increase of the correlation (+27%) can be observed from the previous GHS-BUILT R2019 (0.67) to the current R2023. When testing the capacity to predict the $BU > 0$ Boolean domain, the GHS-BUILT-S R2023 demonstrates an overall accuracy of 0.99, accompanied by an IoU of 0.9, a precision of 0.93 and a recall of 0.97 (Table 12).

5.7. Evaluating 100 m resolution built-up surface layers

In the 'BU_S 100 m' test, we evaluate the ability to predict the quantity of built-up surface area, measured in square meters, within a spatial sample of 100×100 m. We use the BF_REF vector data as a reference and bound the test in the domain stable after 2010, with $TD^{t=2010}$. This was done for two reasons: to facilitate comparability across various models developed after 2010

Table 10. R-accuracy in the BU_S 10 m test of different models by World Bank income level class.

Model	High Income	Upper Middle	Lower Middle	Low Income	Total
GHS-BUILT-S R2023 E2018	0.268	0.240	0.240	0.195	0.235
GHS-BUILT-*P* (2020)	0.233	0.202	0.188	0.132	0.188
GHS-BUILT-*P* (2019)	0.216	0.181	0.183	0.101	0.171
DYNAMICWORLD (2022)	0.130	0.139	0.139	0.099	0.129

Table 11. Correlation of total built-up surface measured by global models with crowd-sourced reference data (See et al. 2022). The table is sorted by descending Spearman rank correlation coefficient.

No	Model	Spearman	No	Model	Spearman
1	GHS-BUILT-S R2023 E2018	0.8565	14	GHS-BUILT-*P* (2020)	0.7091
2	WSF2019 (2021)	0.8502	15	GHS-BUILT R2019	0.6725
3	WSF2015v2 (2023)	0.8251	16	GAUD (2020)	0.6566
4	DYNAMICWORLD (2022)	0.7989	17	GHS-BUILT (2017)	0.6427
5	ESRI (2020)	0.7811	18	GISAv2 (2022)	0.6316
6	ESRI (2018)	0.7778	19	GISAv1 (2021)	0.6229
7	WSF2015v1 (2020)	0.7574	20	GAIA (2020)	0.6128
8	WSFEVO (2021)	0.7573	21	FROM_GLC10 (2019)	0.5923
9	GHS-BUILT-*P* (2019)	0.7561	22	GHS-BUILT R2016	0.5875
10	WORLDCOVER (2021)	0.7544	23	MODIS (2010)	0.3712
11	CGLC (2020)	0.7177	24	FROM_GLC30 (2013)	0.3474
12	GISD (2022)	0.7123	25	GLOBE_LAND30 (2014)	0.3103
13	GISA10 (2022)	0.7110			

Table 12. Accuracy measures derived from the HVI_REF_VHR for the GHS-BUILT R2023 in the BU > 0 test.

TP	TN	FP	FN	N	Overall Accuracy	IoU	Precision	Recall
4008	44460	297	119	48884	0.991	0.906	0.931	0.971

using different image data inputs, and to minimize the issue of an unknown exact update of the imagery supporting the BF_REF vector data. The 100 m resolution corresponds to the medium abstraction level of the GHSL, where data from various sources are integrated. This is a strategically relevant piece of GHSL information to be tested. It is worth noting that the size of the spatial units in the test is larger than most of the models considered, except for MODIS (2010), which also facilitates comparability. Lastly, it's important to note that the inherent spatial disagreement between the BF_REF and the various model outputs considered is assumed to be at most half the size of the spatial sample of the test (Pesaresi et al. 2013; See et al. 2022), thereby allowing for comparative assessment.

Figure 26 presents the R-accuracy of various models that predict the BF_REF data, which are sorted by production year and accuracy scores. GHS-BUILT R2023 emerges as the most accurate model, more than doubling the R-accuracy of the benchmark CGLC (2020) 'urban cover fraction' from the Copernicus Land Monitoring Service. The GHS-BUILT R2023 model for the E2015 epoch scores slightly better than the E2020 epoch, indicating that the temporal barycentre of the BF_REF ensemble is closer to 2015 than to 2020. A clear trend of gradual improvement in accuracy from past to recent models is observable, attributable to improved data and methodologies, also observed by Uhl et al. (2020) and Uhl and Leyk (2023).

Since its inception, GHSL has consistently led in providing the best accuracy for each specific year. The SML, using available thematic prior knowledge, has released the most accurate results. Over the past decade, the SML has demonstrated its ability to enhance pre-classification knowledge on built-up areas, enabling the discovery of new information and improved performance in out-of-sample classification exercises. An important observation is the superior performance of continuous models over categorical ones, despite their absence in the past public releases due to a lack of supporting reference data for global validation. However, with the availability of new test data, the decadal R&D investment in the design of continuous surface prediction can now be deployed in GHSL R2023. This supports the technical specifications of future GHSL releases within the Copernicus Emergency Management Services framework. Figure 27 displays the R-accuracy and MAE of various models, stratified by UN-SDG-Region and WB-Income. The GHS-BUILT R2023 model provides the most accurate predictions and the lowest MAE for built-up surface area across the considered strata, thereby confirming the overall observation. When stratified by built-up density quantiles along the urban-rural

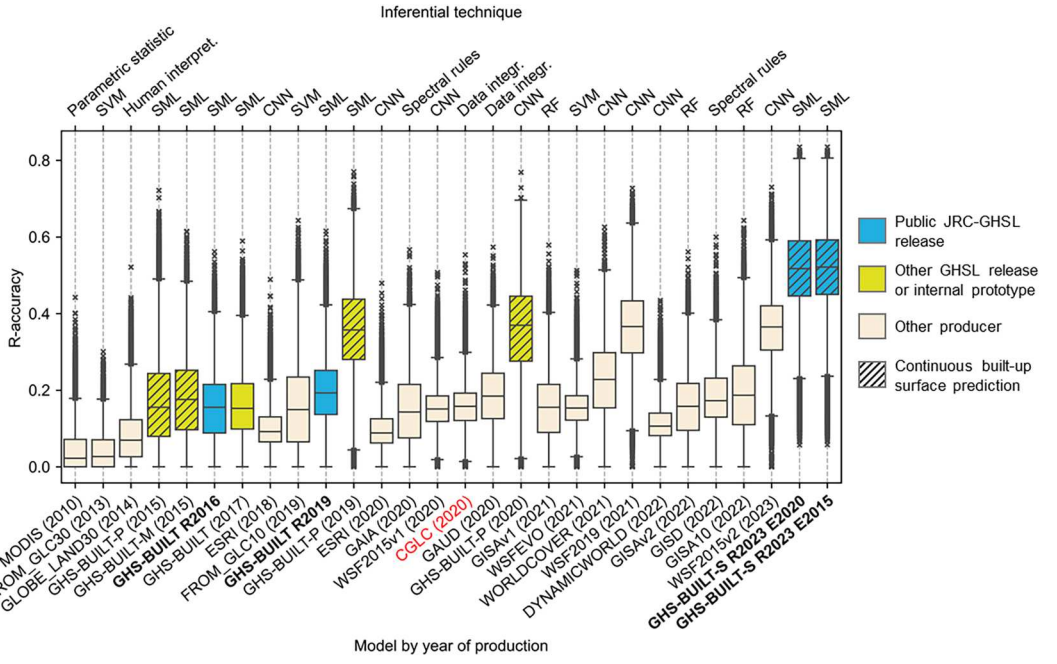

Figure 26. Comparative assessment of R-accuracy in predicting the total built-up surface at 100 m resolution. Tests, supported by the entire BF_REF, were conducted in the domain $TD^{t=2010}$. Datasets produced by the GHSL project are shown in light blue (public full releases) or yellow (other releases or internal prototypes), benchmark CGLC (2020) is labeled in red. Continuous models are represented in specific dash pattern.

continuum (cf. Leyk et al. 2018), the superiority of the GHS-BUILT R2023 model is further confirmed (Uhl et al. 2024).

The new GHS-BUILT-S R2023 data significantly improves the assessment of built-up surfaces in vulnerable areas that play a crucial role in disaster management (Adger 2006; Benevolenza and DeRigne 2019; Hunter et al. 2021), overcoming limitations of existing remote sensing technologies. These technologies often struggle with accurately assessing informal settlements, excluding vulnerable populations from crucial policy information (Van Den Hoek and Friedrich 2021). The R2023 data emerges as the most effective predictor in low-income countries and refugee camps, marking a significant advancement. A systematic 'income bias' is evident in remote sensing-derived measurements, with lower income levels associated with lower accuracy performances (see Figure 27, R-accuracy in low-income stratum). However, GHS-BUILT-S R2023 outperforms other sources, achieving 55.56% higher performance compared to the best non-GHSL option. It also proves to be the best predictor of built-up surface area in the refugee camp strata, achieving 45.8% higher performance than the second best and 400% higher than the previous GHS-BUILT R2019 release (Table 13). Here the stratum is defined by a global set of 345 UNHCR-managed refugee camps[19], in the 297 test cases (86.1% of the total) where BF_REF data was available (see Appendix section K.1.5).

5.8. Evaluation of 100 m resolution multi-temporal built-up dynamics

The 'BU_S MT 100 m' test utilized 7 754 BF_REF data blocks where the year of construction was available (Table 8). It is important to note that in the BF_REF data, buildings that were dismantled and subsequently rebuilt only retain the most recent year of construction. This overlooks the fact that the same location had previously been built upon. This oversight implicitly inflates the error

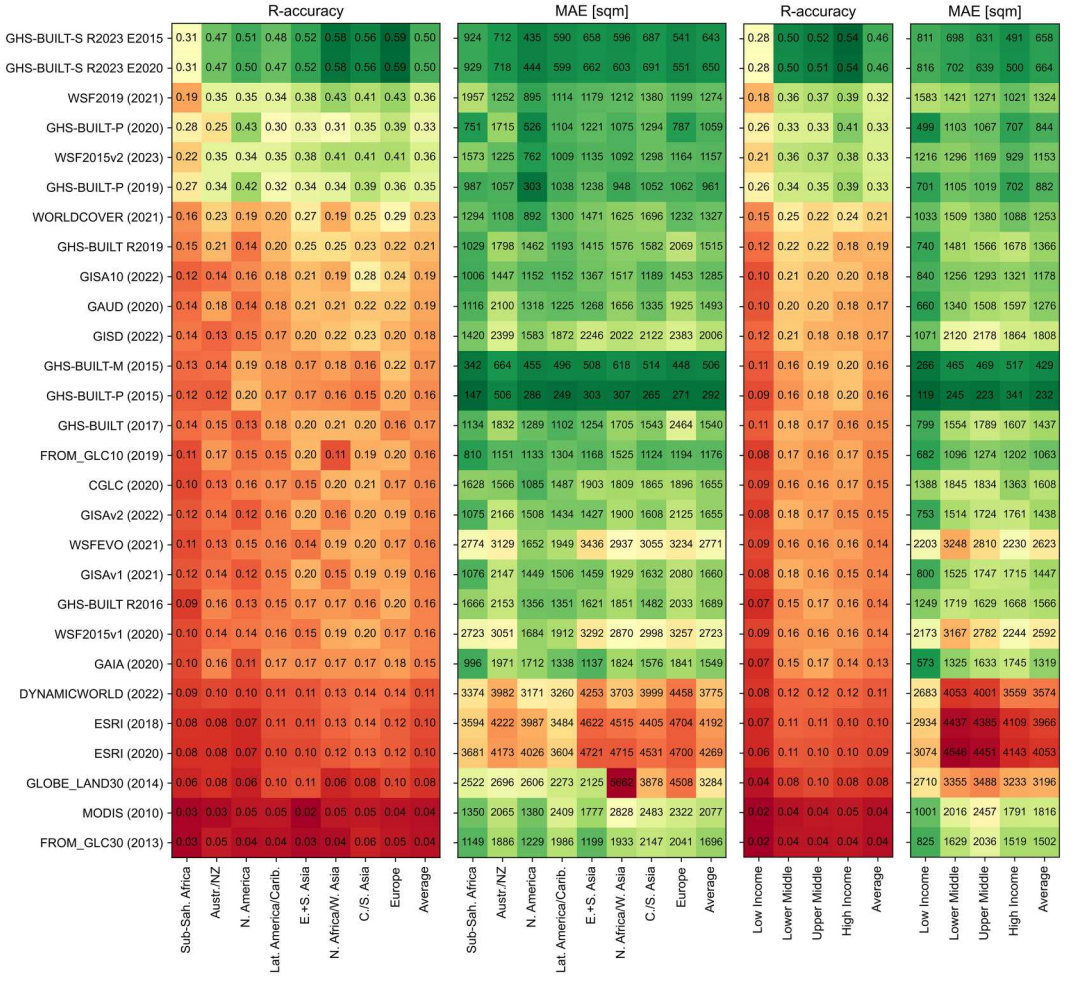

Figure 27. R-accuracy and MAE of various models by UN-SDG-Region and by WB-Income classification. Heat maps are sorted vertically by the average R-accuracy per model across all strata (descending), and horizontally by the strata-averages across all models.

rates reported in the study, as satellite data logically document built-up surfaces both before and after the building alterations.

The study demonstrates an increase in accuracy from 0.25 (1975) to 0.43 (2020) in GHSL data, a trend which is in line with previous research (Leyk et al. 2018; Uhl and Leyk 2022a; 2022b). (Table 14), attributed to the improved quality of Landsat imagery and the accumulation of temporal error induced by the BF_REF. RMSE and MAE slightly increase as built-up surface expands, but remain stable, suggesting a constant bias useful for determining change rates. High standard deviations of RMSE and MAE indicate significant error variation across tiles. GHS-BUILT-S R2023 outperforms other models in predicting built-up surfaces at 100 m resolution over time, with an average R-accuracy of 0.36 across all epochs, 125% better than GISD30 and 157.14% better than GHSL R2019. It shows a 16.13% improvement over the R2022 version, particularly in early epochs. The trend of increasing MAE over time is consistent with other models, while the bias remains stable (Figure 28).

Table 13. R-accuracy in prediction of built-up surfaces in refugee camps by different global models, and by UN-SDG-region, sorted by average R-accuracy.

Model	Central and Southern Asia	Eastern and Southern Asia	Northern Africa and Western Asia	Sub-Saharan Africa	Average
GHS-BUILT-S R2023 E2020	0.57	0.53	0.46	0.30	0.35
WSF2015v2 (2023)	0.25	0.41	0.26	0.23	0.24
GHS-BUILT-*P* (2019)	0.27	0.36	0.20	0.21	0.22
WORLDCOVER (2021)	0.37	0.35	0.25	0.19	0.22
WSF2019 (2021)	0.30	0.41	0.35	0.16	0.21
GISA10 (2022)	0.22	0.40	0.22	0.16	0.18
GHS-BUILT-*P* (2020)	0.26	0.15	0.14	0.17	0.17
GISD (2022)	0.28	0.25	0.22	0.12	0.15
FROM_GLC10 (2019)	0.19	0.16	0.24	0.13	0.15
CGLC (2020)	0.17	0.27	0.16	0.10	0.13
GHS-BUILT-*P* (2015)	0.15	0.08	0.08	0.10	0.10
WSF2015v1 (2020)	0.15	0.23	0.13	0.08	0.10
GHS-BUILT-M (2015)	0.12	0.04	0.10	0.10	0.10
DYNAMICWORLD (2022)	0.20	0.17	0.08	0.08	0.10
WSFEVO (2021)	0.15	0.22	0.14	0.07	0.09
ESRI (2018)	0.18	0.14	0.13	0.07	0.09
ESRI (2020)	0.16	0.19	0.14	0.06	0.09
GHS-BUILT (2017)	0.08	0.08	0.09	0.07	0.08
GHS-BUILT R2019	0.13	0.10	0.10	0.06	0.08
GHS-BUILT R2016	0.06	0.04	0.07	0.05	0.05
GISAv1 (2021)	0.11	0.13	0.02	0.05	0.05
GISAv2 (2022)	0.11	0.12	0.01	0.05	0.05
GLOBE_LAND30 (2014)	0.11	0.08	0.07	0.04	0.05
GAUD (2020)	0.07	0.03	0.07	0.04	0.05
GAIA (2020)	0.02	0.001	0.03	0.01	0.02
MODIS (2010)	0.03	0.00	0.00	0.01	0.01
FROM_GLC30 (2013)	0.005	0.00	0.00	0.003	0.002

Table 14. Agreement of the GHS-BUILT-S R2023 built-up surface estimates at 100 m spatial resolution with a reference database of building footprint data attributed with construction year information. Shown are averages of agreement measures calculated at the tile level for a global set of 7754 tiles of 25 km × 25 km.

Year	R-accuracy	RMSE	MAE
1975	0.249 ± 0.054	213.903 ± 119.728	64.242 ± 71.2665
1980	0.312 ± 0.053	206.876 ± 111.0905	61.999 ± 66.827
1985	0.308 ± 0.054	216.864 ± 114.906	65.783 ± 70.5705
1990	0.35 ± 0.053	212.385 ± 108.9245	64.026 ± 68.843
1995	0.344 ± 0.0525	229.909 ± 116.124	71.019 ± 73.5085
2000	0.397 ± 0.049	230.855 ± 115.6905	71.127 ± 73.4275
2005	0.393 ± 0.049	241.371 ± 117.477	75.883 ± 75.4025
2010	0.438 ± 0.0495	234.871 ± 112.3635	73.91 ± 72.6845
2015	0.429 ± 0.049	247.858 ± 115.677	79.059 ± 75.407
2020	0.426 ± 0.0495	253.934 ± 116.868	81.385 ± 76.476
All	0.3646 ± 0.0513	228.8826 ± 114.8849	70.8433 ± 72.4413

5.9. Evaluating 100 m resolution average height of built-up structures

The 'BU_H 100 m' test utilized 16128 BF_REF data blocks where the building heights were available from cadastral data or proprietary data (Table 8). Figure 29 shows the predicted vs. BF_REF observed ANBH in the cities of Sao Paulo (Brazil), Soul (South Korea), Milan (Italy), Washington, (US), Melbourne (Australia) and Warsaw (Poland). Building height reported by the BF_REF does not necessarily align with the definition applied by the GHSL (Table 1). Undefined terms can be implicit in the available BF_REF, including different points in the roof area and in the terrain of the building footprint to be taken as reference (min, max, or median elevation). This fact alone

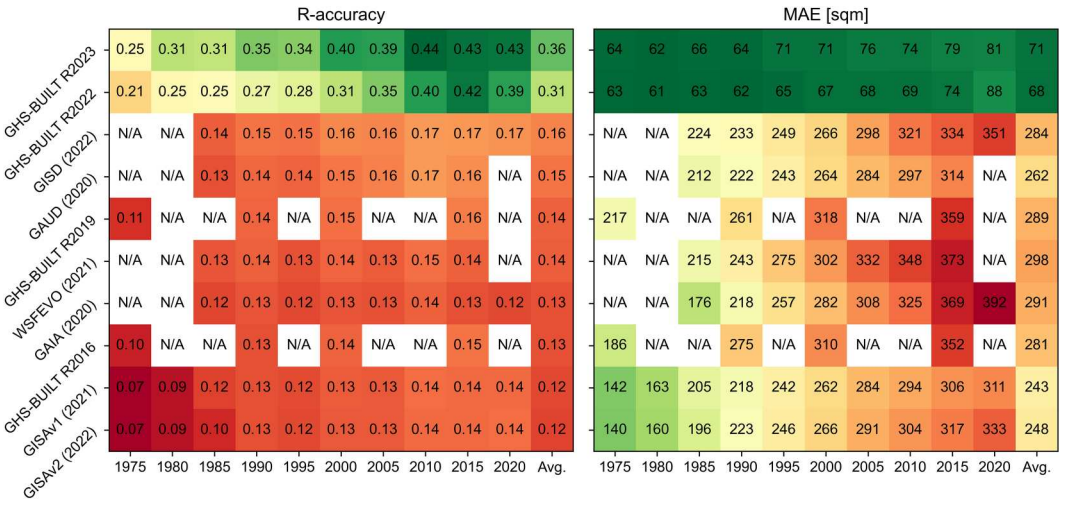

Figure 28. Agreement of the GHSL R2023A built-up surface estimates, and a range of related global datasets, at 100 m spatial resolution with a reference database of building footprint data attributed with construction year information. Shown are averages of agreement measures calculated at the tile level for a global set of 7754 tiles of 25 km × 25 km.

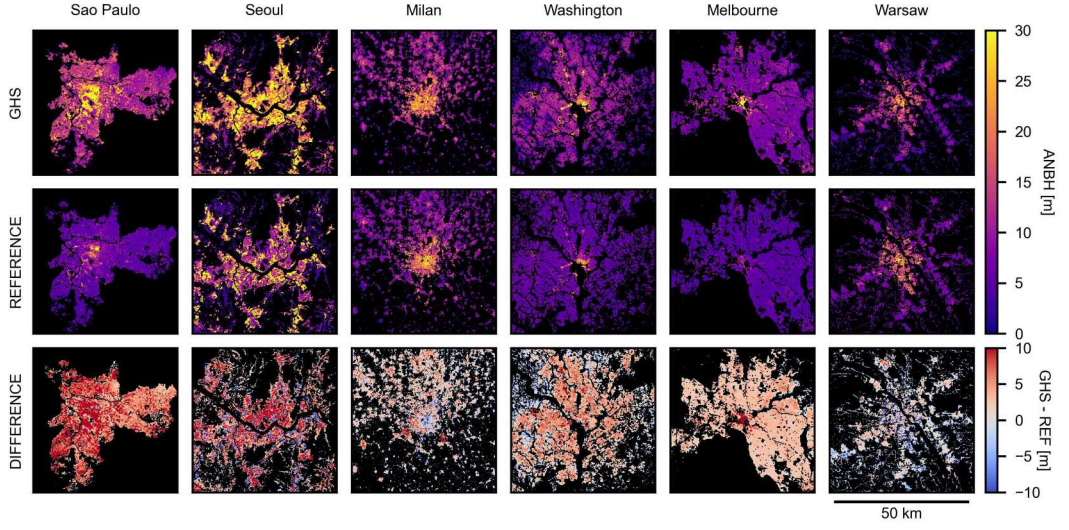

Figure 29. Predicted GHS-BUILT-H R2023 (top row) and reference (middle row) ANBH values at 100 m resolution for six test areas (50 × 50 km), from left to right: Sao Paulo (Brazil), Seoul (South Korea), Milan (Italy), Washington, (US), Melbourne (Australia) and Warsaw (Poland). Bottom row shows absolute difference between the predicted and the reference ANBH values, with blue color indicating underestimation of ANBH, red color indicating overestimation of ANBH and white color indicating agreement between the predicted and the reference values.

injects an expected uncertainty of 2-3 meters in the analysis. Additionally, some BF_REF sources may include speculative building height information derived from the declared number of floors, thus implicitly assuming flat roof and flat terrain. All these factors artificially inflate the error rates and contribute to a decrease in the accuracy estimation.

The study was conducted by stratifying the BF_REF data based on the temporal characteristics of the built-up surface corresponding to the dominant reference year of the DEMs that support the various models (i.e. 'Stable_BU2010' vs. 'New_BU2020') and by the UN-SDG-region.

Table 15. Aggregated performances of the various models in all the BF_REF available data.

Model	Avg. R-accuracy	Avg. MAE	Avg. RMSE
GHS-BUILT-H R2023	0.56	2.27	3.31
WSF3D (2022)	0.43	2.38	3.68
GHSL (2021)	0.35	4.59	5.72
GHSL (2016)	0.24	3.32	4.24
ALOS_30 m (2023)	0.22	3.91	4.88
S1_1 km (2022)	0.18	4.05	4.62
S1_500 m (2022)	0.11	6.34	9.13

Table 15 presents the R-accuracy, MAE, and RMSE obtained by various models using the entire BF_REF dataset. Overall, GHS-BUILT-H R2023 outperforms the considered alternatives in predicting the average building height at a 100 m resolution, achieving R-accuracy of 0.56. This is significantly higher than the best alternative, WSF3D (2022), which provides an R-accuracy of 0.43. The GHS-BUILT-H R2023 model has an average MAE and RMSE of 2.27 m and 3.31 m, respectively. If observed by UN-SDG-region and by temporal strata, GHS-BUILT-H R2023 consistently outperforms all the alternatives in predicting the Stable_BU2010 domain (R-accuracy of 0.58 for all regions), except for the few BF_REF data falling in Latin America (Figure 30, left). However, due to the scarcity of available BF_REF data, we cannot generalize this observation to the entire region. In predicting the New_BU2020 domain, the GHS-BUILT-H R2023 largely outperforms all the alternatives, in all the available UN-SDG-regions (Figure 30, right) with an average scoring of 0.53 as compared to the second best ALOS_30 m (2023) scoring 0.18, and a very low scoring close to zero of the only models using updated Sentinel-1 data: S1_500 m (2022) and S1_1 km (2022). This clearly indicates the added value of processing updated Sentinel-2 data, as included in the GHS-BUILT-H R2023 model.

5.10. Evaluating population distribution grids

Performance metrics are calculated by aggregating GHS-POP 100 m data to the native reference vector grids, as reported in the authoritative sources of POP_REF, and by comparing the modeled population counts with the reference counts. This method differs from common practices that

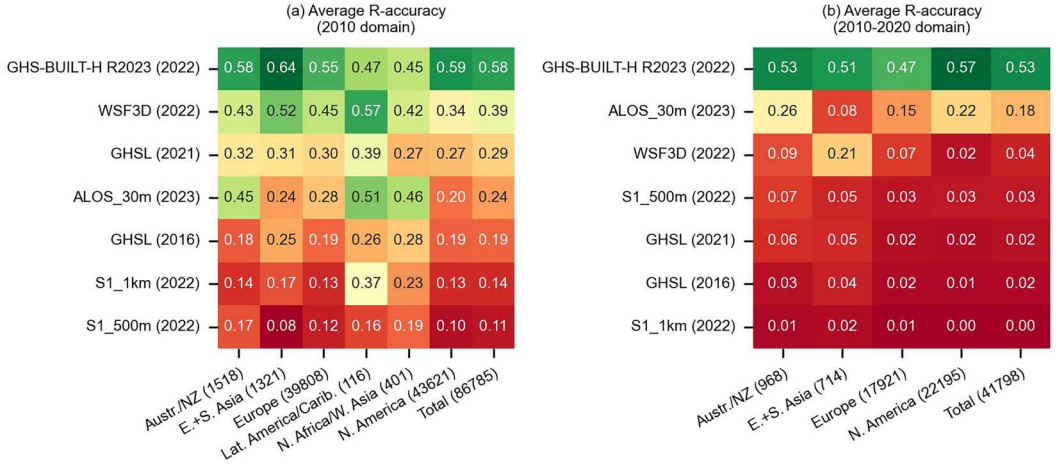

Figure 30. Average R-accuracy of all tested models, categorized by UN-SDG-region. The left side represents the Stable_BU2010 domain, while the right side represents the New_BU2020 domain. The number of available BF_REF data tiles for each region is indicated in brackets.

Table 16. R-accuracy and %TAA (in brackets) for each population grid (WPC: WorldPop UN adjusted constrained; WPU: WorldPop UN adjusted unconstrained) for each reference year available (census grids). Aggregated and RMSE columns refer to data for all available epochs aggregated.

	1995	2000	2005	2010	2015	2020	Aggregated	RMSE
GHS-POP R2023	0.71 (83%)	0.69 (82%)	0.73 (85%)	0.73 (84%)	0.74 (85%)	0.68 (81%)	0.71 (83%)	45.4
GHS-POP R2022	0.69 (82%)	0.65 (79%)	0.70 (83%)	0.69 (82%)	0.69 (82%)	0.61 (76%)	0.66 (80%)	55.4
GHS-POP R2019	-	0.61 (76%)	-	-	0.64 (78%)	-	0.62 (77%)	590.9
WPC	-	-	-	-	-	0.59 (74%)	0.59 (74%)	205.6
WPU	-	0.53 (70%)	0.58 (73%)	0.57 (72%)	0.61 (76%)	0.55 (71%)	0.56 (72%)	62.7

primarily focus on comparing different modeling methods, a process known as internal validation (Stevens et al. 2020; Xu et al. 2021). However, external validation, which is detailed in Appendix section K.9 and involves comparison with compatible, reliable, detailed, and complete data (Table 9), offers the most comprehensive accuracy depiction for data users (Archila Bustos et al. 2020; Freire et al. 2016; Leyk et al. 2019).

Table 16 shows that GHS-POP R2023 performs best in each year and across all metrics, followed closely by R2022. The improvements in R2023 over R2022 can be attributed to the use of residential BU volume as a disaggregation covariate. On the other hand, WPU displays the lowest accuracy among the tested grids, with WPC performing better in 2020. The accuracy tends to increase over time up to 2015, primarily due to changes in the approaches used to calculate growth rates, with R2022 using a fixed growth rate.

Identifying unpopulated areas is a crucial feature of gridded population data (Archila Bustos et al. 2020), and we have assessed their accuracy by the main population density classes (see Table K-11 in Appendix). In most countries, R2022 is the best at representing unpopulated areas ($d = 0$), but this could be due to the omission of BU detection. Accuracy tends to increase with increasing population density. However, densely populated areas are often represented by smaller census units, which reduces the need for disaggregation. This observation is confirmed by Brazil (BRA), the country with the smallest census units (PwArea).

6. Thematic results

Here, we present some key findings from the newly integrated GHSL R2023 information. Section 6.1 addresses the global inner characterization of the human settlements for the GHSL nominal year 2020 by joint observation of the BUTYPE, BU-S, BU-V, POP, and SMOD layers. The close-range dynamics of built-up areas and population from 1975-2020 are discussed in Section 6.2. Lastly, Section 6.3 focuses on how the new GHSL aligns with the existing global long-range predictions of built-up surfaces up to the year 2100.

6.1. Adjustment factor of total built-up surface

A systematic comparison with BF_REF reveals the multiplicative gains or adjustment factors required to align the models predicted built-up surface with BF_REF assessment. This alignment is in terms of the aggregated sum of built-up surfaces in large areas such as cities, countries, or regions. Table 17 presents the adjustment factors of the GHS-BUILT R2019 and R2023 predictions

Table 17. Average Adjustment Factors for GHS-BUILT-S model predictions for $TD^{t=2010}$ by the World Bank income level.

	GHS-BUILT R2019 f	GHS-BUILT R2023 f	R2019 f / R2023 f
High Income	0.254	0.637	0.40
Upper Middle	0.418	0.711	0.59
Lower Middle	0.499	0.762	0.65
Low Income	0.514	0.493	1.04
Total BF_REF	0.365	0.689	0.53

calculated for $TD^{t=2010}$. These factors are further subdivided by WB-Income regions. We assume that $\Sigma X' = f \cdot \Sigma X$, where f is the adjustment factor used to translate the sum of built-up surface ΣX predicted by the model into the sum of built-up surface $\Sigma X'$ observed in BU_REF. The factor (f) for R2023 is 0.68, compared to 0.36 for R2019. Both models tend to overestimate the total built-up surface, but R2023 significantly reduces this overestimation, yielding aggregated surface estimates half of those from R2019. Notably, f for R2023 is lower in low-income regions, suggesting that R2023 predictions overestimate the built-up surface more than the norm in these areas. Global quantitative models including aggregate built-up surfaces should consider these regional disparities. However, further research is needed to understand the temporal projection of these adjustment factors, considering the spatial–temporal bias of the GHS-BUILT MT data. This topic falls outside the scope of the study discussed here.

6.2. Global characteristics of the human settlements

According to the GHSL empirical findings, taller buildings are far more prevalent in cities (assumed here as the DEGURBA 'urban centres') than in rural areas (see Figure 31). On average, 91% of the building volume in rural areas belongs to one- or two-story buildings, compared to only 22% in cities. The abundant amount of land in rural areas and the benefits of being close to the city center help to explain why buildings in cities are significantly taller than in rural areas. The income of a country reinforces this pattern. For example, in low-income countries, 99% of building volume in rural areas is in low-rise buildings compared to 86% in high-income countries. In cities of low-income countries, the building volume in low-rise buildings is 45% and drops to 18% in high-income countries.

Cities in low-income countries tend to be smaller than cities in higher income countries (OECD and European Commission 2020), which explains part of the higher prevalence of low-rise buildings in low-income cities. When grouping cities by population size, however, cities in low-income countries continue to have the highest share of low-rise buildings in each of the four city size classes: those shares are typically double than those in cities of high-income countries (Figure 32).

Larger cities tend to have more mid- and high-rise buildings than smaller ones because being close to the center provides more benefits in a large city and the costs of travel to that center are

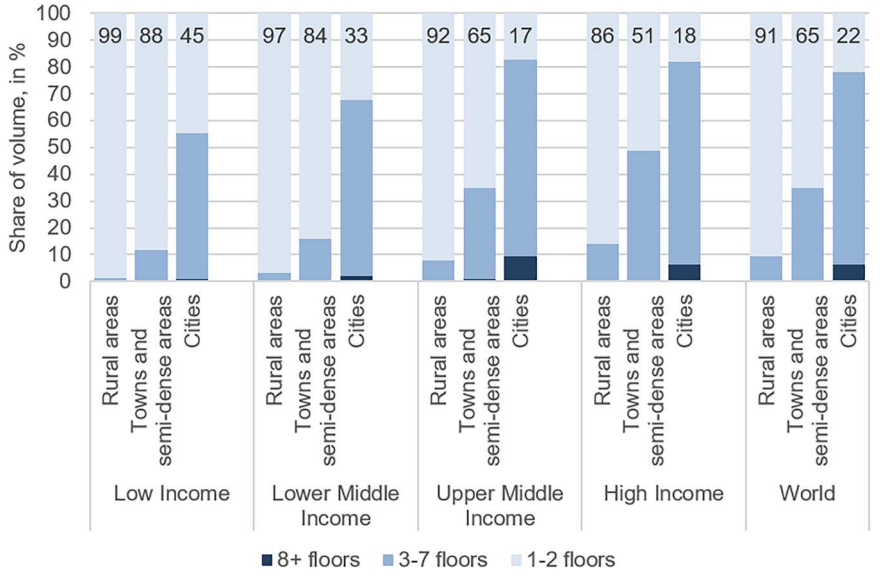

Figure 31. Building volume by number of floors, Degree of Urbanization and income group, 2020.

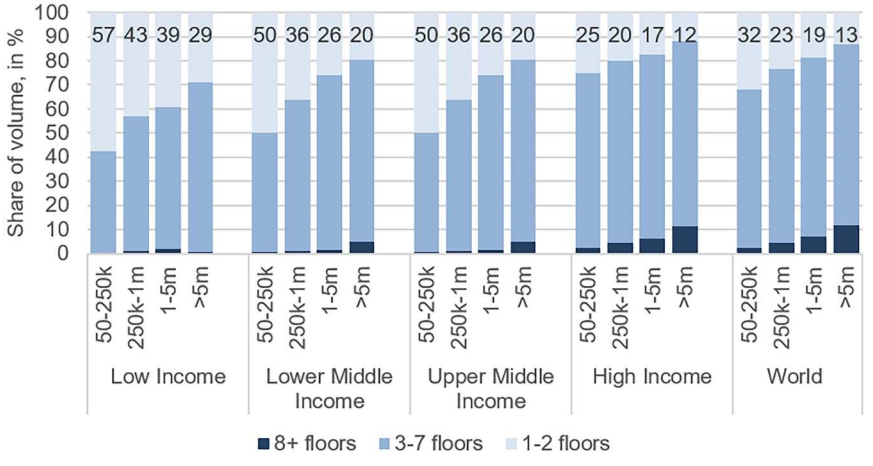

Figure 32. Building volume by number of floors, city size and income group, 2020.

higher. Buildings with at least 8 stories provide 10% of the building volume in high-income cities of at least 5 million inhabitants, while the share is much lower in smaller cities and cities in lower income countries.

Tall buildings can alleviate city overcrowding by offering more floor space within the same land area. Overcrowding remains a significant issue in cities within low and lower-middle-income countries, which have half the building volume per capita compared to cities in upper-middle-income countries, and a fifth compared to cities in high-income countries (Figure 33). These statistics highlight the potential for these cities to expand both vertically and horizontally (Lall et al. 2021). The country's income has the most substantial impact on the building volume per capita, but the size of the city also influences it. In high-income countries, and to a lesser extent in upper-middle-income countries, an increase in city size tends to decrease the building volume per capita. In contrast, in low-income and lower-middle-income countries, the building volume per capita initially increases with city size, then declines for cities with at least 5 million inhabitants. This pattern suggests that as city size increases, the income effect surpasses the cost effect. In other words, in cities with populations exceeding 250 000, the incomes are sufficiently high to offset the

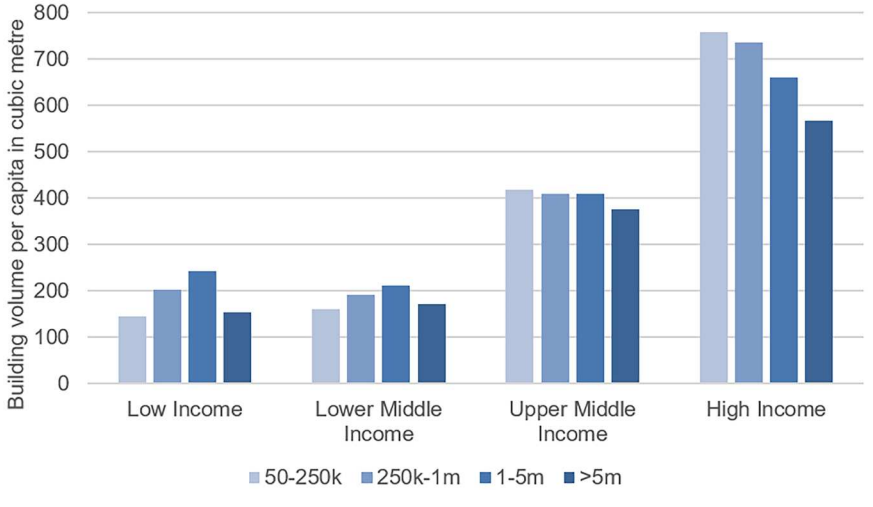

Figure 33. Building volume per capita by city size and income group, 2020.

Table 18. Share of Built-Up Surface Area Pre-existing 1975, Measured in 2020, Categorized by UN-SDG Region.

UN-SDG-region	BU_S 1975/2020 share
Europe	53.3%
Northern America	52.9%
Oceania	51.5%
Australia and New Zealand	46.2%
Latin America and the Caribbean	44.3%
Northern Africa and Western Asia	41.5%
* World barycentre	37.4%
Eastern and Southern Asia	26.8%
Central and Southern Asia	25.7%
Sub-Saharan Africa	24.8%

increased land and construction costs compared to smaller cities. Consequently, the building volume per capita rises with city size and only slightly decreases for cities with at least five million inhabitants.

Among other socio-economic factors, the temporal characteristics of the built stock influence the construction technology and energy efficiency. The longevity, or inertial component, of the built-up stock exhibits significant regional diversity. The proportion of the built-up surface from before 1975, relative to the surface measured in 2020, is highest in Europe (53.3%). In contrast, it is lowest in sub-Saharan Africa (24.8%), with a global average of 37.4% (Table 18).

6.3. Global and regional dynamics

6.3.1. Close-range dynamics 1975-2030

From 1975 to 2020, the global population size doubled from 4 billion to 8 billion, according to UN WPP 2022. This demographic shift corresponded to a sevenfold increase in the global built-up surface area, as per the latest GHSL data. Figure 34 provides a summary of the increase in built-up per capita,

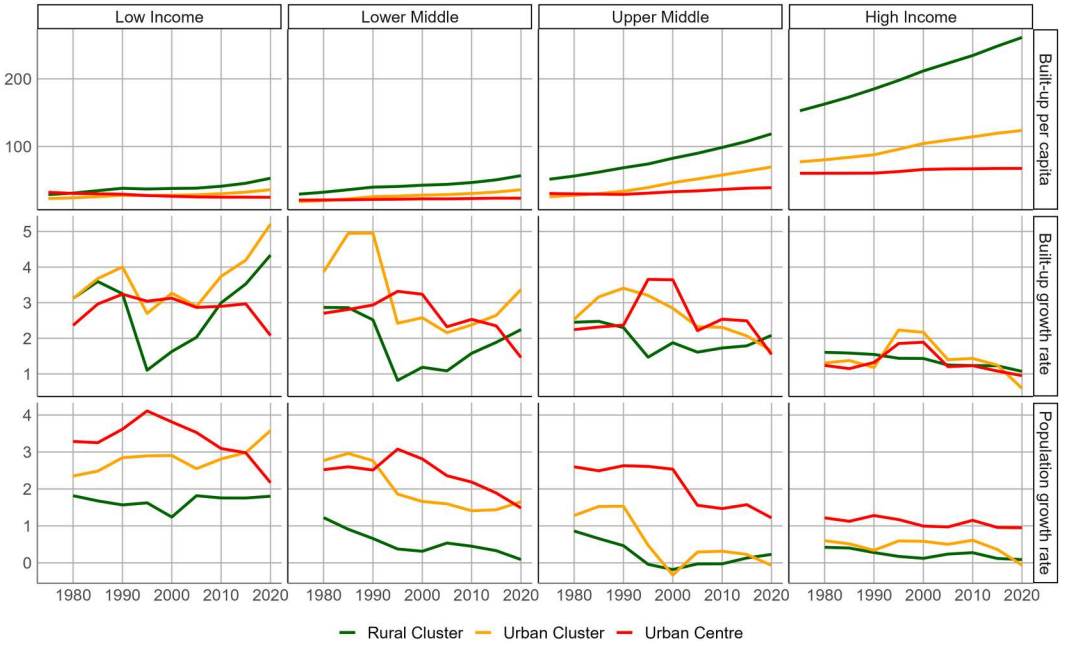

Figure 34. Built-up surface per capita (m^2), built-up surface percentage increase and population percentage increase by World Bank income classes and SMOD categories between 1975 and 2020.

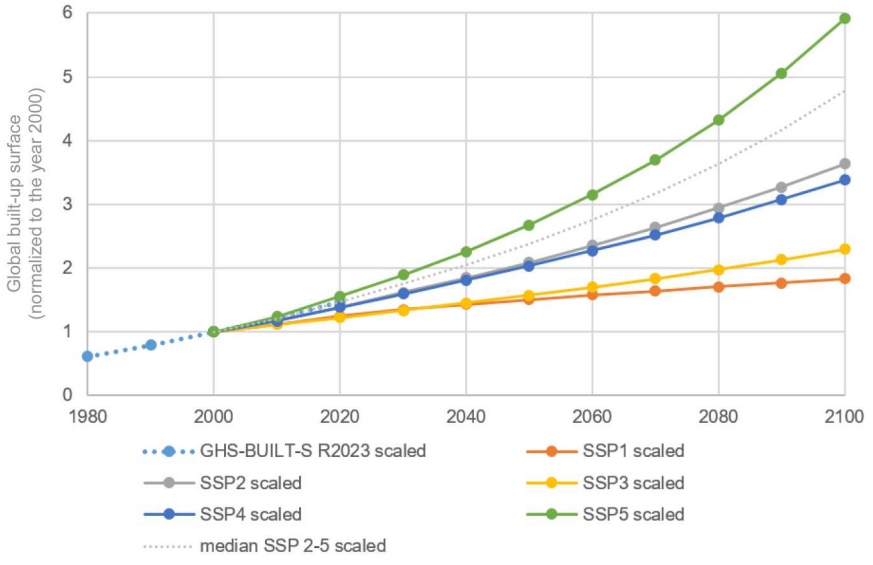

Figure 35. Global built-up surface trends (normalized to the year 2000) in the GHSL R2023 and SSPs projections.

built-up surface, and population respectively. Each indicator is disaggregated by income and degree of urbanization classes, differentiating between urban centers and rural areas. Middle-income countries are the primary drivers of both population and total built-up surface increase, accounting for 76% of the total world population. Despite this, high-income countries still possess the majority of built-up surface per capita, even though only 16% of the total world population resides there. These stark differences are at the core of the 2030 Agenda for Sustainable Development, which aims to end poverty, reduce inequality, address climate change, and preserve oceans and forests. The GHSL data provides a comprehensive dataset that can be used to address interdisciplinary topics across various fields. The implementation of the MTUC module assessed over 50 000 urban center (UC) pairs to track their evolution over time. This revealed that half of the 11 000 UCs in 2020 did not exist in 1975, a phenomenon known as city morphogenesis. It also showed that most large UCs were formed by merging smaller ones. Around 1% of 2020s UCs originated from past splits, a trend potentially increasing with population decrease.

6.3.2. Long range dynamics to 2100

In this section, we examine the alignment of the new GHSL data with existing global projections of built-up areas for the year 2100. Spatially explicit projections of the built-up surface were generated under urbanization scenarios that are consistent with the Shared Socioeconomic Pathways (SSPs), covering the period from 2000 to 2100 (J. Gao and O'Neill 2020). These were later downscaled to a 1 km resolution (J. Gao and Pesaresi 2021), both based on GHSL R2019 data. When comparing built-up surface observations from GHSL R2023 with SSP-consistent projections, we standardize each time series to focus on relative change rates. The rate of change in the global total amount of built-up surface falls between the SSP2 and SSP5 projections, deviating from the sustainability pathway (SSP1). The median trajectory, which lies between SSP2 (middle of the road) and SSP5 (fossil fueled), aligns with the newly observed GHSL data from 2000 to 2020 (Figure 35). If this trend continues, the global total amount of built-up surface in 2100 is projected to be 4.7 times the amount in 2000.

7. Limitations

This section succinctly enumerates the design constraints of the GHSL R2023 data.

1. *Monotonic Built-up Growth Assumption*: This assumption is imposed in the 100 m resolution spatial unit. As a result, the GHSL becomes ineffective for monitoring the deconstruction and reconstruction processes associated with disasters or the dismantling of settlement parts, due to redevelopment and conversion. It assumes a unidirectional growth of built-up areas. The lack of comprehensive reference data for assessing the demolition of individual buildings necessitates this assumption. Typically, only the construction epoch is reported, which complicates the calibration of models designed to assess deconstruction processes.
2. *Backward Constant Functional NRES (2020) Class Share Assumption*: This assumption is imposed in the 100 m resolution spatial unit. Due to the lack of reference data on changing functional destinations for NRES buildings, it is challenging to evaluate the empirical bias induced by this assumption. The GHSL, therefore, is not suitable for assessing the reconversion of industrial buildings to parks or residential complexes, for example.
3. *Backward Constant Average Building Height (2020) Assumption:* This assumption is imposed in the 100 m resolution spatial unit. It is necessary due to limitations in EO data and the absence of reference data to assess the change of building height over time. Depending on local construction conditions and trends, this assumption may inflate BU-V MT volume estimates in the epochs before 2020.
4. *Undisputed Country Territorial Authority Assumption*: This assumption is inherent in the top-down GHSL POP information production. It surmises that a census accurately enumerates the residents in a specific area. However, factors such as occupied territories, conflicts, territorial disputes, nomadic communities, ethnic segregation, and large refugee flows can introduce substantial distortions in the baseline input data and in the resulting population estimates.
5. *Residential Population Assumption*: This assumption limits the suitability of the GHS-POP for estimating daytime population concentration in leisure, commercial, or working places. It is designed to estimate residential populations, not transient or daytime populations.
6. *Unused Building Stock = 0 Assumption*: This can also be expressed as the 'infinite market efficiency assumption'. It assumes that all the BU surfaces observed from EO imagery are used, thus ignoring abandoned or unused building stock in the populated units, or imposing population in confirmed BU surface allocated in unpopulated units. Depending on local market and population conditions (demography, migration), this may generate inflation of the built-up per capita indicators.

8. Conclusions

The GHSL R2023 introduces revolutionary new methodologies and data availability at global scale, significantly enhancing the accuracy of the information extracted from EO data, particularly Sentinel-2 imagery. The globally available data is the first of its kind: it offers 10 m resolution sub-pixel built-up surface, it provides the first globally available residential and non-residential classification, as well as the first global building height database supported by Sentinel-2 imagery. Moreover, the new GHSL provides the first global multi-temporal built-up information product integrating multi-platform EO data collected by Landsat and Sentinel sensors.

Enhanced information from Sentinel-2 data and advanced spatio-temporal modeling, which incorporates city WUP data has greatly improved residential population estimates, time-series population predictions, and spatial resolution.

The GHSL R2023 data underwent validation using three primary independent reference sources: visual interpretation of Sentinel-2 imagery by professional photo-interpreters (one million samples), crowdsourced VHR imagery from Bing and Google (50 000 samples), and a quasi-global set of vector data delineating building footprints. Accuracy measures demonstrate GHSL R2023 high performance over all other considered data sources in providing global land cover and land

use information on human settlements. At a 10 m resolution, it has a 92% accuracy for distinguishing between built-up and non-built-up classes, and a 99% OA for discerning between residential and non-residential built-up. Notably, IoU scores over double in identifying water surfaces in urban environments, compared to the second-best, WORLDCOVER (2021). In the continuous 100 m resolution, GHSL R2023 excels globally in predicting built-up surface for both a fixed year (2010) assessment and a multi-temporal assessment for 1975-2020. It also stands out in predicting average building height, particularly in areas constructed after 2010, the approximate year when the available global DEMs were last updated.

Vulnerable areas such as low-income countries and refugee camps are where there is need for reliable and consistent information. In low-income countries, the accuracy of the GHS-BUILT R2023 outperforms the second-best WSF2019 (2021) by 35% and the last R2019 release by 57%, whereas in refugee camps, it surpasses the second-best WSF2015v2 (2023) by 39% and the last R2019 release by 96%. It is worth noting that these achievements were made possible using computationally simple yet effective modeling as linear regression and SML. According to these findings, SML can either discover new, 'out-of-the-sample' human settlements information with high accuracy, or significantly improve the ones available.

GHS-POP R2023 also outperforms other available data sources. Indeed, it is the best available source of resident population, producing a 38.1% lower RMSE compared to the best non-GHSL model (WPC).

The GHSL data products spanning from 1975 to 2020 allow to appreciate the global population surge from 4 to 8 billion, which has triggered a sevenfold expansion in built-up surfaces and a consistent upward trend in per capita footprint, with stark disparities evident between high-income and low-income countries. The built-up surface change rate for 2000-2020 observed in the new GHSL aligns with median SSP2 and SSP5 projections, diverging from the sustainability pathway (SSP1). If this trend persists, the built-up surface in 2100 will be 4.7 times larger than that of 2000, raising sustainability concerns.

Three noteworthy points emerge from our discussion. First, even though we GHSL R2023 has made significant progress and introduced substantial innovations, there are numerous challenges that must be addressed in the future. For instance, innovative concepts such as fBU and NRES have been introduced, many important aspects are a prototype that needs further development. Two important examples are related to GHSL applications for disaster and crisis management: the ability to generate distinct fine-scale population predictions for day- and night-time (Freire, Florczyk, and Ferri 2015), and the capability to predict infrastructural damage and estimate refugee populations using integrated open EO data analytics (Corbane et al. 2016).

Second, the emergence of new near-global vector data delineating building footprints from VHR could revolutionize GHSL. These data could soon be harnessed for future model enhancements, significantly improving accuracy. Furthermore, they could catalyse a change in the GHSL information paradigm, from a multi-resolution and multi-temporal raster data cube system to a hybrid raster-vector system design.

Finally, the accuracy and effective international decision support of GHSL could attract the interest of scientists and policymakers. The methodological solutions of GHSL could serve as a blueprint for AI designs to foster transparent human dialogue and consensus. This approach, advocating for open science, stands in contrast with the enforcement of black box technological solutions and is key in tackling complex human-related problems.

Notes

1. Group on Earth Observations (GEO) GEOSS Data Sharing Principles post 2015.
2. Directive (EU) 2019/1024 of the European Parliament and of the Council of 20 June 2019 on open data and the re-use of public sector information PE/28/2019/REV/1.
3. '*Repeatability* of measurements' here refers to the ability to repeat measurements made on the same subject under identical conditions, and shall be distinguished from the '*reproducibility* of the experiment' concept common in scientific literature. In case of measurements supported by a supervised classification,

repeatability implies that the same input data (images, training set) and same inferential system should produce always, e.g., the *exact same* built-up surface estimates. By construction, this propriety is not fully satisfied by classification methods requiring stochastic iterative processes for convergence to a given inferential solution.

4. The urban environment is connoted by high mixture of impervious heterogeneous materials (clay, stone, concrete, asphalt, metal, plastic, and glass among many), vegetation, soil, and shadow/water low spectral reflectance components at a global mean scale of 10 meters as measured by spatial autocorrelation techniques from VHR data (Small 2003).
5. CORINE land cover, Part One – Methodology https://www.eea.europa.eu/publications/COR0-part1/download
6. With 30×30 m = 900 m^2 change resolution.
7. Quantized to 1 m^2 change resolution.
8. The International Seminar on Urban Form (ISUF) glossary 'Morphotope' https://www.urbanmorphology.org/glossary.html
9. The European Union, the Food and Agriculture Organization, the International Labour Organization, the Organisation for Economic Co-operation and Development, the United Nations Human Settlements Programme, and the World Bank.
10. Blue, green, red, and near-infrared.
11. They are one closing top-hat with structuring element (SE) of 30×30 m size, and three opening top-hat of increasing size of the structuring element: 30×30 m, 50×50 m, and 100×100 m.
12. Established cultural practices in Asia associate the blue component of the roof to non-residential use of the buildings.
13. Google open buildings, 2023. URL: https://sites.research.google/open-buildings/
14. Microsoft global machine learning footprints, 2023. URL: https://github.com/microsoft/GlobalMLBuildingFootprints
15. Ecopia.AI and Maxar Technologies. 2020. Digitize Africa data. URL: http://digitizeafrica.ai
16. United Nations, The Sustainable Development Goals Report (2019), regional groupings https://unstats.un.org/sdgs/report/2019/regional-groups/
17. World Bank Country and Lending Groups (2021-2022) https://datahelpdesk.worldbank.org/knowledgebase/articles/906519-world-bank-country-and-lending-groups
18. Namely: non-built-up land (NBU_LAND), non-built-up water (NBU_WATER), built-up residential (BU_RES), and built-up non-residential (BU_NRES).
19. UNHCR, 2023. Geoservices. https://data.unhcr.org/en/geoservices/ Accessed: 1 May 2023.
20. Derived from The Construction Wiki, 'Building Height'.
21. Derived from the Infrastructure for Spatial Information in Europe (INSPIRE) 'Residential use' definition.
22. Derived by EMN from Art. 2(d) of Regulation (EC) No 763/2008 (Population and Housing Censuses Regulation).
23. Art. 2(1) of Regulation (EC) No 862/2007 (Migration Statistics Regulation).
24. Derived from B.1.463 'Concepts related to place of residence' Principles and Recommendations for Population and Housing Censuses (Revision 2). United Nations Department of Economic and Social Affairs, Statistics Division. 2008.
25. The Degree of Urbanisation, a new global definition of cities, urban and rural areas: https://ghsl.jrc.ec.europa.eu/degurba.php
26. this is the place for Figure 1 related to Q1

Acknowledgments

We would like to express our profound gratitude to Professor Shlomo Angel for his invaluable support to the GHSL, particularly in the discussions and consolidation of both theoretical background and empirical findings. We especially acknowledge his assistance in defining the BUTYPE concept and its underlying rationale.

We express our gratitude to Patrick Gerland and UNDESA for sharing the extended UN World Urbanization Prospect (WUP) dataset. This fundamental contribution has significantly enhanced the accuracy of the GHS-POP estimates.

We acknowledge INEC (Ecuador), INEGI (Mexico) and KOSTAT (Korea) for sharing their national grids. The availability of these authoritative data strongly enhanced the GHS-POP validation process.

We acknowledge Dr. Duncan Smith of CASA UCL for introducing the color palette and the classification schema used to visualize the GHS-POP gridded data.

We thank Kytt MacManus and CIESIN for providing access to the harmonized census data and support in their analysis.

We express our heartfelt gratitude to Vincent Seaman (BMGF) and Ecopia AI for providing the building footprint data for Africa. This data has been instrumental in significantly improving our capacity to test the GHS-BUILT in areas with low income and vulnerable populations.

We would like to thank Ju Young Kim from the Delegation of the European Union to the Republic of Korea for providing the building footprint data from the Korean National Spatial Information Portal.

Disclosure statement

No potential conflict of interest was reported by the author(s).

Funding

The manuscript displays work that is supported by the European Commission's Joint Research Centre (EC-JRC) institutional research program 2020-2025. This work is part of the 'Global Human Settlement Trends and Characteristics' project [grant no 32161], and includes related scientific collaboration activities such as the 'Human Planet Initiative' (HPI). The HPI falls under the Group on Earth Observations (GEO) Strategic Plan 2016-2025. In addition, the activities have been funded by the European Commission's Directorate-General for Regional and Urban Policy (DG REGIO) [grant no 35864]. Further funding has been provided by the European Commission's Directorate-General for Defence Industry and Space (DG DEFIS) as part of the European Space programme Copernicus. This includes the implementation of the Emergency Management Service [grant no 35803].

Data availability statement

The data that support the findings of this study are openly available in Joint Research Center Data Catalogue, at Global Human Settlement Layer collection: https://data.jrc.ec.europa.eu/collection/ghsl

The data supporting the validation part of this study derived from the resources available in the public domain are listed in Appendix section K.

The data introduced in this manuscript (products of BUTYPE and MTUC modules, see Table 2) are available from the corresponding author, MP, upon reasonable request.

ORCID

Martino Pesaresi http://orcid.org/0000-0003-0620-439X
Marcello Schiavina http://orcid.org/0000-0003-3399-3400
Panagiotis Politis http://orcid.org/0000-0001-6417-1587
Sergio Freire http://orcid.org/0000-0003-2282-701X
Katarzyna Krasnodębska http://orcid.org/0000-0002-1398-9095
Johannes H. Uhl http://orcid.org/0000-0002-4861-5915
Alessandra Carioli http://orcid.org/0000-0002-8345-5400
Christina Corbane http://orcid.org/0000-0002-2670-1302
Lewis Dijkstra http://orcid.org/0000-0002-4077-8250
Pietro Florio http://orcid.org/0000-0001-7866-7401
Hannah K. Friedrich http://orcid.org/0000-0002-5661-615X
Jing Gao http://orcid.org/0000-0003-1778-8909
Stefan Leyk http://orcid.org/0000-0001-9180-4853
Linlin Lu http://orcid.org/0000-0003-1647-1950
Ines Mari-Rivero http://orcid.org/0000-0003-1821-0420
Michele Melchiorri http://orcid.org/0000-0002-3009-8868
Vasileios Syrris http://orcid.org/0000-0002-2262-0580
Jamon Van Den Hoek http://orcid.org/0000-0001-8074-0022
Thomas Kemper http://orcid.org/0000-0002-3446-8301

References

Adger, W. Neil. 2006. "Vulnerability." *Global Environmental Change* 16 (3): 268–281.

Angel, Shlomo, and Patrick Lamson-Hall. 2020. "Anatomy of Density II: A Comprehensive Strategy for Making Room for City Densification." *August*, https://doi.org/10.2139/ssrn.3744466.

Angel, Shlomo, Patrick Lamson-Hall, Alejandro Blei, Sharad Shingade, and Suman Kumar. 2021. "Densify and Expand: A Global Analysis of Recent Urban Growth." *Sustainability* 13 (7): 3835. https://doi.org/10.3390/su13073835.

Archila Bustos, Maria Francisca, Ola Hall, Thomas Niedomysl, and Ulf Ernstson. 2020. "A Pixel Level Evaluation of Five Multitemporal Global Gridded Population Datasets: A Case Study in Sweden, 1990–2015." *Population and Environment* 42 (2): 255–277. https://doi.org/10.1007/s11111-020-00360-8.

Balsamo, Gianpaolo, Anna Agusti-Panareda, Clement Albergel, Gabriele Arduini, Anton Beljaars, Jean Bidlot, Nicolas Bousserez, et al. 2018. "Satellite and in Situ Observations for Advancing Global Earth Surface Modelling: A Review." *Remote Sensing* 10 (12): 2038.

Batista e Silva, Filipe, Sérgio Freire, Marcello Schiavina, Konštantín Rosina, Mario Alberto Marín-Herrera, Lukasz Ziemba, Massimo Craglia, Eric Koomen, and Carlo Lavalle. 2020. "Uncovering Temporal Changes in Europe's Population Density Patterns Using a Data Fusion Approach." *Nature Communications* 11 (1): 4631. https://doi.org/10.1038/s41467-020-18344-5.

Bechtel, Benjamin, Martino Pesaresi, Aneta J. Florczyk, and Gerald Mills. 2018. "Beyond Built-up: The Internal Makeup of Urban Areas." In *Urban Remote Sensing*, edited by Qihao Weng, Dale Quattrochi, and Paolo Gamba, 83–124. CRC Press.

Benevolenza, Mia A., and LeaAnne DeRigne. 2019. "The Impact of Climate Change and Natural Disasters on Vulnerable Populations: A Systematic Review of Literature." *Journal of Human Behavior in the Social Environment* 29 (2): 266–281. https://doi.org/10.1080/10911359.2018.1527739.

Bettencourt, Luís M. A. 2021. *Introduction to Urban Science: Evidence and Theory of Cities as Complex Systems*. Cambridge, MA and London, England: The MIT Press.

Beucher, Serge, and Fernand Meyer. 2018. "The Morphological Approach to Segmentation: The Watershed Transformation." In *Mathematical Morphology in Image Processing*, edited by Edward R. Dougherty, 433–481. Boca Raton: CRC Press.

Bo, George E. P. 1976. "Science and Statistics." *Journal of the American Statistical Association* 71 (356): 791–799. https://doi.org/10.2307/2286841.

Boden, Margaret A. 2008. *Mind as Machine: A History of Cognitive Science*. New York: Oxford University Press.

Bondarenko, Maksym, David Kerr, Alessandro Sorichetta, and Andrew Tatem. 2020. "Census/Projection-Disaggregated Gridded Population Datasets, Adjusted to Match the Corresponding UNPD 2020 Estimates, for 183 Countries in 2020 Using Built-Settlement Growth Model (BSGM) Outputs." University of Southampton. https://doi.org/10.5258/SOTON/WP00685.

Brown, Christopher F., Steven P. Brumby, Brookie Guzder-Williams, Tanya Birch, Samantha Brooks Hyde, Joseph Mazzariello, Wanda Czerwinski, et al. 2022. "Dynamic World, Near Real-Time Global 10 m Land Use Land Cover Mapping." *Scientific Data* 9 (1): 251. https://doi.org/10.1038/s41597-022-01307-4.

Buchhorn, Marcel, Bruno Smets, Luc Bertels, Bert De Roo, Myroslava Lesiv, Nandin-Erdene Tsendbazar, Martin Herold, and Steffen Fritz. 2020. "Copernicus Global Land Service: Land Cover 100m: Collection 3: Epoch 2019: Globe." Zenodo. https://doi.org/10.5281/ZENODO.3939050.

Center For International Earth Science Information Network - CIESIN - Columbia University. 2018. *"Gridded Population of the World, Version 4 (GPWv4): Population Count, Revision 11." Palisades*. NY: NASA Socioeconomic Data and Applications Center (SEDAC). https://doi.org/10.7927/H4JW8BX5.

Conzen, Michael Robert Gunter. 1960. "Alnwick, Northumberland: A Study in Town-Plan Analysis." *Transactions and Papers (Institute of British Geographers)* 27:iii–122.

Corbane, Christina, Thomas Kemper, Sergio Freire, Christophe Louvrier, and Martino Pesaresi. 2016. "Monitoring the Syrian Humanitarian Crisis with the JRC's Global Human Settlement Layer and Night-Time Satellite Data." JRC101733. Luxembourg (Luxembourg): Publications Office of the European Union. https://publications.jrc.ec.europa.eu/repository/handle/JRC101733.

Corbane, Christina, Martino Pesaresi, Thomas Kemper, Panagiotis Politis, Aneta J. Florczyk, Vasileios Syrris, Michele Melchiorri, Filip Sabo, and Pierre Soille. 2019. "Automated Global Delineation of Human Settlements from 40 Years of Landsat Satellite Data Archives." *Big Earth Data* 3 (2): 140–169. https://doi.org/10.1080/20964471.2019.1625528.

Corbane, Christina, Martino Pesaresi, Panagiotis Politis, Vasileios Syrris, Aneta Jadwiga Florczyk, Pierre Soille, Luca Maffenini, et al. 2017. "Mass Processing of Sentinel-1 and Landsat Data for Mapping Human Settlements at Global Level." *In Proc. of the BiDS* 17:52–55. https://doi.org/10.2760/383579.

Corbane, Christina, and Panagiotis Politis. 2020. "GHS-Composite-S2 R2020A - Sentinel-2 Global Pixel Based Image Composite from L1C Data for the Period 2017-2018." *European Commission, Joint Research Centre (JRC)*, https://doi.org/10.2905/0BD1DFAB-E311-4046-8911-C54A8750DF79.

Corbane, Christina, Panagiotis Politis, Pieter Kempeneers, Dario Simonetti, Pierre Soille, Armin Burger, Martino Pesaresi, Silip Sabo, Vasileios Syrris, and Thomas Kemper. 2020a. "A Global Cloud Free Pixel- Based Image Composite from Sentinel-2 Data." *Data in Brief* 31 (August): 105737. https://doi.org/10.1016/j.dib.2020.105737.

Corbane, Christina, Filip Sabo, Vassilis Syrris, Thomas Kemper, Panagiotis Politis, Martino Pesaresi, Pierre Soille, and Kenji Ose. 2020b. "Application of the Symbolic Machine Learning to Copernicus VHR Imagery: The European Settlement Map." *IEEE Geoscience and Remote Sensing Letters* 17 (7): 1153–1157. https://doi.org/10.1109/LGRS.2019.2942131.

Corbane, Christina, Vasileios Syrris, Filip Sabo, Panagiotis Politis, Michele Melchiorri, Martino Pesaresi, Pierre Soille, and Thomas Kemper. 2021. "Convolutional Neural Networks for Global Human Settlements Mapping from Sentinel-2 Satellite Imagery." *Neural Computing and Applications* 33 (12): 6697–6720. https://doi.org/10.1007/s00521-020-05449-7.

Craglia, Max, Kees de Bie, Davina Jackson, Martino Pesaresi, Gábor Remetey-Fülöpp, Changlin Wang, Alessandro Annoni, et al. 2012. "Digital Earth 2020: Towards the Vision for the next Decade." *International Journal of Digital Earth* 5 (1): 4–21. https://doi.org/10.1080/17538947.2011.638500.

Dijkstra, Lewis, Aneta J. Florczyk, Sergio Freire, Thomas Kemper, Michele Melchiorri, Martino Pesaresi, and Marcello Schiavina. 2021. "Applying the Degree of Urbanisation to the Globe: A New Harmonised Definition Reveals a Different Picture of Global Urbanisation." *Journal of Urban Economics* 125:103312. https://doi.org/10.1016/j.jue.2020.103312.

Doxiadis, Constantinos A. 1970. "Ekistics, the Science of Human Settlements: Ekistics Starts with the Premise That Human Settlements Are Susceptible of Systematic Investigation." *Science* 170 (3956): 393–404.

Esch, Thomas, Elisabeth Brzoska, Stefan Dech, Benjamin Leutner, Daniela Palacios-Lopez, Annekatrin Metz-Marconcini, Mattia Marconcini, Achim Roth, and Julian Zeidler. 2022. "World Settlement Footprint 3D - A First Three-Dimensional Survey of the Global Building Stock." *Remote Sensing of Environment* 270 (March): 112877. https://doi.org/10.1016/j.rse.2021.112877.

Esch, Thomas, Mattia Marconcini, Andreas Felbier, Achim Roth, Wieke Heldens, Martin Huber, Maximilian Schwinger, H. Taubenbock, Andreas Muller, and Stefan Dech. 2013. "Urban Footprint Processor—Fully Automated Processing Chain Generating Settlement Masks From Global Data of the TanDEM-X Mission." *IEEE Geoscience and Remote Sensing Letters* 10 (6): 1617–1621. https://doi.org/10.1109/LGRS.2013.2272953.

European Commission. Joint Research Centre. 2023. *GHSL Data Package 2023*. LU: Publications Office. https://data.europa.eu/doi/10.2760098587.

European Commission. Statistical Office of the European Union. 2021. "Applying the Degree of Urbanisation: A Methodological Manual to Define Cities, Towns and Rural Areas for International Comparisons : 2021 Edition." LU: Publications Office of the European Union. https://data.europa.eu/doi/10.2785706535.

European Space Agency and Airbus. 2022. "Copernicus DEM." European Space Agency. https://doi.org/10.5270/ESA-c5d3d65.

Freire, Sergio. 2010. "Modeling of Spatiotemporal Distribution of Urban Population at High Resolution–Value for Risk Assessment and Emergency Management." In *Geographic Information and Cartography for Risk and Crisis Management*, edited by Milan Konecny, Sisi Zlatanova, and Temenoujka L. Bandrova, 53–67. Berlin, Heidelberg: Springer.

Freire, Sergio, Aneta J. Florczyk, and Stefano Ferri. 2015. "Modeling Day-and Night-Time Population Exposure at High Resolution: Application to Volcanic Risk Assessment in Campi Flegrei." *Proceedings of the Twelfth International Conference on Information Systems for Crisis Response and Management. Kristiansand, Norway*.

Freire, Sergio, Kytt MacManus, Martino Pesaresi, Erin Doxsey-Whitfield, and Jane Mills. 2016. "Development of New Open and Free Multi-Temporal Global Population Grids at 250 m Resolution." *Proc. of the 19th AGILE Conference on Geographic Information Science. Vol. 250. Helsinki, Finland 14–17 June: AGILE*.

Freire, Sergio, Marcello Schiavina, Aneta J. Florczyk, Kytt MacManus, Martino Pesaresi, Christina Corbane, Olena Borkovska, et al. 2020. "Enhanced Data and Methods for Improving Open and Free Global Population Grids: Putting 'Leaving No One behind' into Practice." *International Journal of Digital Earth* 13 (1): 61–77. https://doi.org/10.1080/17538947.2018.1548656.

Gao, Jing, and Brian C. O'Neill. 2020. "Mapping Global Urban Land for the 21st Century with Data-Driven Simulations and Shared Socioeconomic Pathways." *Nature Communications* 11 (1): 2302. https://doi.org/10.1038/s41467-020-15788-7.

Gao, Jing, and Martino Pesaresi. 2021. "Downscaling SSP-Consistent Global Spatial Urban Land Projections from 1/8-Degree to 1-Km Resolution 2000–2100." *Scientific Data* 8 (1): 281. https://doi.org/10.1038/s41597-021-01052-0.

Gao, Bingbo, Jinfeng Wang, Alfred Stein, and Ziyue Chen. 2022. "Causal Inference in Spatial Statistics." *Spatial Statistics* 50 (August): 100621. https://doi.org/10.1016/j.spasta.2022.100621.

German Aerospace Center (DLR). 2023. "World Settlement Footprint (WSF) 2015 v2 - Landsat-8/Sentinel-1 - Global." 2023. https://download.geoservice.dlr.de/WSF2015/.

Ghanbari, Hamid, Masoud Mahdianpari, Saeid Homayouni, and Fariba Mohammadimanesh. 2021. "A Meta-Analysis of Convolutional Neural Networks for Remote Sensing Applications." *IEEE Journal of Selected Topics in Applied Earth Observations and Remote Sensing* 14:3602–3613. https://doi.org/10.1109/JSTARS.2021.3065569.

Goch, Katarzyna, Martino Pesaresi, Christina Corbane, Panagiotis Politis, and Thomas Kemper. 2023. "Multiple Regression Model for Estimating Vertical Characteristics of Built-up Areas at 100 m Resolution from Open and Global Digital Elevation Models." In *2023 Joint Urban Remote Sensing Event (JURSE)*, edited by Nektarios Chrysoulakis, Giorgos Somarakis, Hannes Taubenböck, Monika Kuffer, and Clément Mallet, 1–4. Heraklion, Greece: IEEE. https://doi.org/10.1109/JURSE57346.2023.10144185.

Gong, Peng, Le Yu Jie Wang, Yongchao Zhao, Yuanyuan Zhao, Lu Liang, Zhenguo Niu, et al. 2013. "Finer Resolution Observation and Monitoring of Global Land Cover: First Mapping Results with Landsat TM and ETM+ Data." *International Journal of Remote Sensing* 34 (7): 2607–2654. https://doi.org/10.1080/01431161.2012.748992.

Gong, Peng, Xuecao Li, Jie Wang, Yuqi Bai, Bin Chen, Tengyun Hu, Xiaoping Liu, et al. 2020. "Annual Maps of Global Artificial Impervious Area (GAIA) between 1985 and 2018." *Remote Sensing of Environment* 236 (January): 111510. https://doi.org/10.1016/j.rse.2019.111510.

Gong, Peng, Han Liu, Meinan Zhang, Congcong Li, Jie Wang, Huabing Huang, Nicholas Clinton, et al. 2019. "Stable Classification with Limited Sample: Transferring a 30-m Resolution Sample Set Collected in 2015 to Mapping 10-m Resolution Global Land Cover in 2017." *Science Bulletin* 64 (6): 370–373.

Gonzales, Jack Joseph. 2023. "Building-Level Comparison of Microsoft and Google Open Building Footprints Datasets (Short Paper)." *12th International Conference on Geographic Information Science (GIScience 2023)*. Schloss-Dagstuhl-Leibniz Zentrum für Informatik.

Gueguen, Lionel, and Maruno Pesaresi. 2014. "Interscale Learning and Classification for Global HR/VHR Image Information Extraction." In *2014 IEEE Geoscience and Remote Sensing Symposium*, 1481–1484. Quebec City, QC: IEEE. https://doi.org/10.1109/IGARSS.2014.6946717.

Gueguen, Lionel, Pierre Soille, and Martino Pesaresi. 2012. "A New Built-up Presence Index Based on Density of Corners." In *2012 IEEE International Geoscience and Remote Sensing Symposium*, 5398–5401. Munich, Germany: IEEE. https://doi.org/10.1109/IGARSS.2012.6352386.

He, Tingting, Kechao Wang, Wu Xiao, Suchen Xu, Mengmeng Li, Runjia Yang, and Wenze Yue. 2023. "Global 30 Meters Spatiotemporal 3D Urban Expansion Dataset from 1990 to 2010." *Scientific Data* 10 (1): 321.

Hollstein, André, Karl Segl, Luis Guanter, Maximilian Brell, and Marta Enesco. 2016. "Ready-to-Use Methods for the Detection of Clouds, Cirrus, Snow, Shadow, Water and Clear Sky Pixels in Sentinel-2 MSI Images." *Remote Sensing* 8 (8): 666. https://doi.org/10.3390/rs8080666.

Huang, Xin, Jiayi Li, Jie Yang, Zhen Zhang, Dongrui Li, and Xiaoping Liu. 2021. "30 m Global Impervious Surface Area Dynamics and Urban Expansion Pattern Observed by Landsat Satellites: From 1972 to 2019." *Science China Earth Sciences* 64 (11): 1922–1933. https://doi.org/10.1007/s11430-020-9797-9.

Huang, Xin, Yihong Song, Jie Yang, Wenrui Wang, Huiqun Ren, Mengjie Dong, Yujin Feng, Haidan Yin, and Jiayi Li. 2022a. "Toward Accurate Mapping of 30-m Time-Series Global Impervious Surface Area (GISA)." *International Journal of Applied Earth Observation and Geoinformation* 109:102787.

Huang, Xin, Jie Yang, Wenrui Wang, and Zhengrong Liu. 2022b. "Mapping 10 m Global Impervious Surface Area (GISA-10 m) Using Multi-Source Geospatial Data." *Earth System Science Data* 14 (8): 3649–3672. https://doi.org/10.5194/essd-14-3649-2022.

Huang, Huanchun, Yingxia Yun, Jiangang Xu, Rong Huang, Jing Fu, and Kaidi Huang. 2017. "Scale Response of Summer Urban Heat Island to Building Plot Ratio and Its Warning Parameter." *Tehnicki Vjesnik - Technical Gazette* 24 (3): 877–886. https://doi.org/10.17559/TV-20170508154351.

Hunter, Lori M, Stephanie Koning, Elizabeth Fussell, Brian King, Andrea Rishworth, Alexis Merdjanoff, Raya Muttarak, et al. 2021. "Scales and Sensitivities in Climate Vulnerability, Displacement, and Health." *Population and Environment* 43:61–81.

Ichoku, Charles, and Arnon Karnieli. 1996. "A Review of Mixture Modeling Techniques for Sub-Pixel Land Cover Estimation." *Remote Sensing Reviews* 13 (3–4): 161–186.

Isard, Walter. 1949. "The General Theory of Location and Space-Economy." *The Quarterly Journal of Economics* 63 (4): 476–506.

Jaccard, Paul. 1901. "Étude Comparative de La Distribution Florale Dans Une Portion Des Alpes et Des Jura." *Bull Soc Vaudoise Sci Nat* 37:547–579.

Karra, Krishna, Caitlin Kontgis, Zoe Statman-Weil, Joseph C. Mazzariello, Mark Mathis, and Steven P. Brumby. 2021. "Global Land Use / Land Cover with Sentinel 2 and Deep Learning." In *2021 IEEE International Geoscience and Remote Sensing Symposium IGARSS*, 4704–4707. Brussels, Belgium: IEEE. https://doi.org/10.1109/IGARSS47720.2021.9553499.

Krasnodębska, Katarzyna, Wojciech Goch, Johannes H. Uhl, Judith A. Verstegen, and Martino Pesaresi. 2024. "Advancing Precision, Recall, F-Score, and Jaccard Index: An Approach for Continuous Gridded Data." *Recall, F-Score, and Jaccard Index: An Approach for Continuous Gridded Data*, https://doi.org/10.2139/ssrn.4865121.

Kropf, Karl. 2018. *The Handbook of Urban Morphology*. Chichester, West Sussex: John Wiley & Sons.

Lall, Somik, Mathilde Lebrand, Hogeun Park, Daniel Sturm, and Anthony Venables. 2021. *Pancakes to Pyramids: City Form to Promote Sustainable Growth*. Washington, DC: World Bank. http://hdl.handle.net/10986/35684.

Lanczos, Cornelius. 1988. *Applied Analysis*. New York: Courier Corporation.

Leyk, Stefan, Andrea E. Gaughan, Susana B. Adamo, Alex De Sherbinin, Deborah Balk, Sergio Freire, Amy Rose, et al. 2019. "The Spatial Allocation of Population: A Review of Large-Scale Gridded Population Data Products and Their Fitness for Use." *Earth System Science Data* 11 (3): 1385–1409. https://doi.org/10.5194/essd-11-1385-2019.

Leyk, Stefan, Johannes H. Uhl, Deborah Balk, and Bryan Jones. 2018. "Assessing the Accuracy of Multi-Temporal Built-up Land Layers across Rural-Urban Trajectories in the United States." *Remote Sensing of Environment* 204 (January): 898–917. https://doi.org/10.1016/j.rse.2017.08.035.

Li, Mengmeng, Yuan Wang, Job F. Rosier, Peter H. Verburg, and Jasper van Vliet. 2022. "Global Maps of 3D Built-up Patterns for Urban Morphological Analysis." *International Journal of Applied Earth Observation and Geoinformation* 114 (November): 103048. https://doi.org/10.1016/j.jag.2022.103048.

Liu, Xiaoping, Yinghuai Huang, Xiaocong Xu, Xuecao Li, Xia Li, Philippe Ciais, Peirong Lin, et al. 2020. "High-Spatiotemporal-Resolution Mapping of Global Urban Change from 1985 to 2015." *Nature Sustainability* 3 (7): 564–570. https://doi.org/10.1038/s41893-020-0521-x.

Mach, Katharine J, Maria Carmen Lemos, Alison M Meadow, Carina Wyborn, Nicole Klenk, James C Arnott, Nicole M Ardoin, et al. 2020. "Actionable Knowledge and the Art of Engagement." *Current Opinion in Environmental Sustainability* 42 (February): 30–37. https://doi.org/10.1016/j.cosust.2020.01.002.

Maragos, Petros, and Lúcio FC Pessoa. 1999. "Morphological Filtering for Image Enhancement and Detection." *The Image and Video Processing Handbook*, 135–156.

Marconcini, Mattia, Annekatrin Metz-Marconcini, Thomas Esch, and Noel Gorelick. 2021. "Understanding Current Trends in Global Urbanisation-the World Settlement Footprint Suite." *GI_Forum* 9 (1): 33–38.

Marconcini, Mattia, Annekatrin Metz-Marconcini, Soner Üreyen, Daniela Palacios-Lopez, Wiebke Hanke, Felix Bachofer, Julian Zeidler, et al. 2020. "Outlining Where Humans Live, the World Settlement Footprint 2015." *Scientific Data* 7 (1): 242. https://doi.org/10.1038/s41597-020-00580-5.

Melchiorri, Michele., Marco Broglia, Fermín Ros, Espe Amezqueta, Isabel Goñi, Panagiotis Politis, Martino Pesaresi, and Thomas Kemper. 2024. *Human Expert Interpretation of One Million Sentinel 2 Records for Built-up Land and Water Discrimination for the Copernicus Exposure Mapping Component*. Luxembourg: Publications Office of the European Union.

Melchiorri, Michele, and Thomas Kemper. 2023. "Establishing an Operational and Continuous Monitoring of Global Built-up Surfaces with the Copernicus Global Human Settlement Layer." In *2023 Joint Urban Remote Sensing Event (JURSE)*, edited by Nektarios Chrysoulakis, Giorgos Somarakis, Hannes Taubenböck, Monika Kuffer, and Clément Mallet, 1–4. Heraklion, Greece: IEEE. https://doi.org/10.1109/JURSE57346.2023.10144201.

Meyer, Fernand. 1994. "Topographic Distance and Watershed Lines." *Signal Processing* 38 (1): 113–125. https://doi.org/10.1016/0165-1684(94)90060-4.

National Geomatics Center of China. 2014. "30-Meter Global Land Cover Dataset (GlobeLand30) - Product Discribtion." National Geomatics Center of China.

National Institute for Standards and Technology. 2007. "Guidelines for Evaluating and Expressing the Uncertainty of NIST Measurement Results." http://physics.nist.gov/Pubs/guidelines/contents.html.

OECD and European Commission. 2020. *Cities in the World: A New Perspective on Urbanisation*. OECD Urban Studies. OECD. https://doi.org/10.1787/d0efcbda-en.

Oliveira, Vítor. 2019. *JWR Whitehand and the Historico-Geographical Approach to Urban Morphology*. Cham, Switzerland: Springer.

Pekel, Jean-François, Andrew Cottam, Noel Gorelick, and Alan S. Belward. 2016. "High-Resolution Mapping of Global Surface Water and Its Long-Term Changes." *Nature* 540 (7633): 418–422. https://doi.org/10.1038/nature20584.

Pesaresi, Martino. 2018. "Principles and Applications of the Global Human Settlement Layer." *IGARSS 2018 - 2018 IEEE International Geoscience and Remote Sensing Symposium*, 2047–2050. Valencia: IEEE. https://doi.org/10.1109/IGARSS.2018.8519155.

Pesaresi, Martino, and Jón Atli Benediktsson. 2001. "A New Approach for the Morphological Segmentation of High-Resolution Satellite Imagery." *IEEE Transactions on Geoscience and Remote Sensing* 39 (2): 309–320. https://doi.org/10.1109/36.905239.

Pesaresi, Martino, Christina Corbane, Andreea Julea, Aneta Florczyk, Vasileios Syrris, and Pierre Soille. 2016a. "Assessment of the Added-Value of Sentinel-2 for Detecting Built-up Areas." *Remote Sensing* 8 (4): 299. https://doi.org/10.3390/rs8040299.

Pesaresi, Martino, Christina Corbane, Chao Ren, and Ng Edward. 2021. "Generalized Vertical Components of Built-up Areas from Global Digital Elevation Models by Multi-Scale Linear Regression Modelling." *Edited by Guy J-P. Schumann. PLoS One* 16 (2): e0244478. https://doi.org/10.1371/journal.pone.0244478.

Pesaresi, Martino, and Daniele Ehrlich. 2009. "A Methodology to Quantify Built-up Structures from Optical VHR Imagery." In *Global Mapping of Human Settlement Experiences, Datasets, and Prospects*, edited by Paolo Gamba, and Martin Herold, 27–58. Boca Raton: CRC Press.

Pesaresi, Martino, Daniele Ehrlich, Stefano Ferri, Aneta J. Florczyk, Sergio Freire, Fernand Haag, Matina Halkia, Andreea Julea, Thomas Kemper, and Pierre Soille. 2015a. "Global Human Settlement Analysis for Disaster Risk Reduction." *The International Archives of the Photogrammetry, Remote Sensing and Spatial Information Sciences* XL-7/W3 (April): 837–843. https://doi.org/10.5194/isprsarchives-XL-7-W3-837-2015.

Pesaresi, Martino, Daniele Ehrlich, Stefano Ferri, Aneta J. Florczyk, Sergio Freire, Matina Halkia, Andreea Julea, Thomas Kemper, Pierre Soille, and Vasileios Syrris. 2016b. "Operating Procedure for the Production of the Global Human Settlement Layer from Landsat Data of the Epochs 1975, 1990, 2000, and 2014." JRC Technical Report EUR 27741. JRC Technical Report. Luxembourg (Luxembourg): Publications Office of the European Union. https://doi.org/10.2788/253582.

Pesaresi, Martino, Andrea Gerhardinger, and FranÇois Kayitakire. 2008. "A Robust Built-Up Area Presence Index by Anisotropic Rotation-Invariant Textural Measure." *IEEE Journal of Selected Topics in Applied Earth Observations and Remote Sensing* 1 (3): 180–192. https://doi.org/10.1109/JSTARS.2008.2002869.

Pesaresi, Martino, Guo Huadong, Xavier Blaes, Daniele Ehrlich, Stefano Ferri, Lionel Gueguen, Matina Halkia, et al. 2013. "A Global Human Settlement Layer from Optical HR/VHR RS Data: Concept and First Results." *IEEE Journal of Selected Topics in Applied Earth Observations and Remote Sensing* 6 (5): 2102–2131. https://doi.org/10.1109/JSTARS.2013.2271445.

Pesaresi, Martino, Georgios K. Ouzounis, and Lionel Gueguen. 2012. "A New Compact Representation of Morphological Profiles: Report on First Massive VHR Image Processing at the JRC." In *SPIE Defense, Security, and Sensing*, edited by Sylvia S. Shen, and Paul E. Lewis, 839025–839026. Baltimore, Maryland: SPIE. https://doi.org/10.1117/12.920291.

Pesaresi, Martino, and Panagiotis Politis. 2022. "GHS-LAND R2022A - Land Fraction as Derived from Sentinel2 Image Composite (2018) and OSM Data." European Commission, Joint Research Centre (JRC). https://doi.org/10.2905/AB7AD451-5ED5-44A6-A4D0-9F7A4E848CEE.

Pesaresi, Martino, and Panagiotis Politis. 2023a. "GHS-BUILT-C R2023A - GHS Settlement Characteristics, Derived from Sentinel2 Composite (2018) and Other GHS R2023A Data." European Commission, Joint Research Centre (JRC). https://doi.org/10.2905/3C60DDF6-0586-4190-854B-F6AA0EDC2A30.

Pesaresi, Martino, and Panagiotis Politis. 2023b. "GHS-BUILT-S R2023A - GHS Built-up Surface Grid, Derived from Sentinel2 Composite and Landsat, Multitemporal (1975-2030)." European Commission, Joint Research Centre (JRC). https://doi.org/10.2905/9F06F36F-4B11-47EC-ABB0-4F8B7B1D72EA.

Pesaresi, Martino, Panagiotis Politis, Katarzyna Goch, and Thomas Kemper. 2024. "Operational Procedure for Multi-Temporal Assessment of Built-up Surfaces and Volumes in the Global Human Settlement Layer R2023A." JRC Technical Report EUR 31811 EN. JRC Technical Report. Luxembourg (Luxembourg): Publications Office of the European Union. https://doi.org/10.2760/664949.

Pesaresi, Martino, Vasileios Syrris, and Andreea Julea. 2015b. "Benchmarking of the Symbolic Machine Learning Classifier with State of the Art Image Classification Methods - Application to Remote Sensing Imagery, EUR 27518." JRC Technical Report EUR 27518. JRC Technical Report. Luxembourg: Publications Office of the European Union. https://doi.org/10.2788/638672.

Pesaresi, Martino, Vasileios Syrris, and Andreea Julea. 2016a. "A New Method for Earth Observation Data Analytics Based on Symbolic Machine Learning." *Remote Sensing* 8 (5): 399. https://doi.org/10.3390/rs8050399.

Pesaresi, Martino, Vasileios Syrris, and Andreea Julea. 2016b. "Analyzing Big Remote Sensing Data via Symbolic Machine Learning." Proceedings of the 2016 Conference on Big Data from Space (BiDS'16), Santa Cruz de Tenerife (Spain) March 2016156–159. https://doi.org/10.2788/854791.

Rabus, Bernhard, Michael Eineder, Achim Roth, and Richard Bamler. 2003. "The Shuttle Radar Topography Mission —a New Class of Digital Elevation Models Acquired by Spaceborne Radar." *ISPRS Journal of Photogrammetry and Remote Sensing* 57 (4): 241–262. https://doi.org/10.1016/S0924-2716(02)00124-7.

Ratti, Carlo, Nick Baker, and Koen Steemers. 2005. "Energy Consumption and Urban Texture." *Energy and Buildings* 37 (7): 762–776. https://doi.org/10.1016/j.enbuild.2004.10.010.

Ratti, Carlo, S. Di Sabatino, R. Britter, M. Brown, F. Caton, and S. Burian. 2002. "Analysis of 3-D Urban Databases with Respect to Pollution Dispersion for a Number of European and American Cities." *Water, Air and Soil Pollution: Focus* 2 (5): 459–469. https://doi.org/10.1023/A:1021380611553.

Ružička, M. 1958. "Anwendung Mathematisch-Statistischer Methoden in Der Geobotanik (Synthetische Bearbeitung von Aufnahmen)." *Biologia, Bratislava* 13:647–661.

Salat, Serge. 2011. *Cities and Forms: On Sustainable Urbanism*. Paris: CSTB Urban Morphology Laboratory.

Salembier, Philippe, and Jean Serra. 1995. "Flat Zones Filtering, Connected Operators, and Filters by Reconstruction." *IEEE Transactions on Image Processing* 4 (8): 1153–1160. https://doi.org/10.1109/83.403422.

Schiavina, Marcello, Michele Melchiorri, and Sérgio Freire. 2023. "A Smart and Flexible Approach for Aggregation of Adjacent Polygons to Meet a Minimum Target Area or Attribute Value." *Scientific Reports* 13 (1): 4367. https://doi.org/10.1038/s41598-023-31253-z.

Schneider, Annemarie, Mark A. Friedl, and David Potere. 2010. "Mapping Global Urban Areas Using MODIS 500-m Data: New Methods and Datasets Based on 'Urban Ecoregions.'" *Remote Sensing of Environment* 114 (8): 1733–1746. https://doi.org/10.1016/j.rse.2010.03.003.

See, Linda, Ivelina Georgieva, Martina Duerauer, Thomas Kemper, Christina Corbane, Luca Maffenini, Javier Gallego, et al. 2022. "A Crowdsourced Global Data Set for Validating Built-up Surface Layers." *Scientific Data* 9 (1): 13. https://doi.org/10.1038/s41597-021-01105-4.

Serra, Jean. 1982. "Morphology for Grey-Tone Functions." *Image Analysis and Mathematical Morphology* 1:424–478.

Small, Christopher. 2003. "High Spatial Resolution Spectral Mixture Analysis of Urban Reflectance." *Remote Sensing of Environment* 88 (1–2): 170–186. https://doi.org/10.1016/j.rse.2003.04.008.

Soille, Pierre, and Martino Pesaresi. 2002. "Advances in Mathematical Morphology Applied to Geoscience and Remote Sensing." *IEEE Transactions on Geoscience and Remote Sensing* 40 (9): 2042–2055. https://doi.org/10.1109/TGRS.2002.804618.

Stevens, Forrest R., Andrea E. Gaughan, Jeremiah J. Nieves, Adam King, Alessandro Sorichetta, Catherine Linard, and Andrew J. Tatem. 2020. "Comparisons of Two Global Built Area Land Cover Datasets in Methods to Disaggregate Human Population in Eleven Countries from the Global South." *International Journal of Digital Earth* 13 (1): 78–100. https://doi.org/10.1080/17538947.2019.1633424.

Stone, Kirk H. 1965. "The Development of a Focus for the Geography of Settlement." *Economic Geography* 41 (4): 346. https://doi.org/10.2307/141945.

Tadono, Takeo, Hirotsugu Ishida, Fumiko Oda, Sei Naito, Kazunari Minakawa, and Hiroshi Iwamoto. 2014. "Precise Global DEM Generation by ALOS PRISM." *ISPRS Annals of the Photogrammetry, Remote Sensing and Spatial Information Sciences* II–4 (April): 71–76. https://doi.org/10.5194/isprsannals-II-4-71-2014.

Tambassi, Timothy. 2018. "From a Geographical Perspective: Spatial Turn, Taxonomies and Geo-Ontologies." In *The Philosophy of Geo-Ontologies*, edited by Timothy Tambassi, 27–36. Cham: Springer International Publishing.

Uhl, Johannes H., and Stefan Leyk. 2022a. "A Scale-Sensitive Framework for the Spatially Explicit Accuracy Assessment of Binary Built-up Surface Layers." *Remote Sensing of Environment* 279 (September): 113117. https://doi.org/10.1016/j.rse.2022.113117.

Uhl, Johannes H., and Stefan Leyk. 2022b. "Assessing the Relationship between Morphology and Mapping Accuracy of Built-up Areas Derived from Global Human Settlement Data." *GIScience & Remote Sensing* 59 (1): 1722–1748. https://doi.org/10.1080/15481603.2022.2131192.

Uhl, Johannes H., and Stefan Leyk. 2022c. "MTBF-33: A Multi-Temporal Building Footprint Dataset for 33 Counties in the United States (1900–2015)." *Data in Brief* 43 (August): 108369. https://doi.org/10.1016/j.dib.2022.108369.

Uhl, Johannes H., and Stefan Leyk. 2023. "Spatially Explicit Accuracy Assessment of Deep Learning-Based, Fine-Resolution Built-up Land Data in the United States." *International Journal of Applied Earth Observation and Geoinformation* 123 (September): 103469. https://doi.org/10.1016/j.jag.2023.103469.

Uhl, Johannes H., Martino Pesaresi, Panagiotis Politis, Katarzyna Goch, Michele Melchiorri, and Thomas Kemper. 2024. "Towards a Quasi-Global Accuracy Assessment of Built-up Surface Estimates Derived from Sentinel-2 Multispectral Data." In *IGARSS 2024*. Athens, Greece. https://doi.org/10.1109/IGARSS53475.2024.10641573.

Uhl, Johannes H., Hamidreza Zoraghein, Stefan Leyk, Deborah Balk, Christina Corbane, Vasileios Syrris, and Aneta J. Florczyk. 2020. "Exposing the Urban Continuum: Implications and Cross-Comparison from an Interdisciplinary Perspective." *International Journal of Digital Earth* 13 (1): 22–44. https://doi.org/10.1080/17538947.2018.1550120.

United Nations, Department of Economic and Social Affairs, Population Division. 2022. "World Population Prospects 2022: Data Sources." https://population.un.org/wpp/Download/Documentation/Documentation/.

UN. Statistical Commission (UNSC). 2020. "Report on the Fifty-First Session (3-6 March 2020)." Supplement No. 4 E/2020/24-E/CN.3/2020/37. New York: Economic and Social Council, Official Records.

Van Den Hoek, Jamon, and Hannah K. Friedrich. 2021. "Satellite-Based Human Settlement Datasets Inadequately Detect Refugee Settlements: A Critical Assessment at Thirty Refugee Settlements in Uganda." *Remote Sensing* 13 (18): 3574. https://doi.org/10.3390/rs13183574.

Wilkinson, Mark D., Michel Dumontier, Ijsbrand Jan Aalbersberg, Gabrielle Appleton, Myles Axton, Arie Baak, Niklas Blomberg, et al. 2016. "The FAIR Guiding Principles for Scientific Data Management and Stewardship." *Scientific Data* 3 (1): 160018. https://doi.org/10.1038/sdata.2016.18.

WorldPop. 2018. "Global High Resolution Population Denominators Project." *Funded by The Bill Melinda Gates Foundation (OPP1134076) Sch. Geogr. Environ. Sci. Univ. Southampton; Dep. Geogr. Geosci. Univ. Louisville; Departement de Geogr. Univ. de Namur) Cent. for Int. Earth Sci. Inf. Netw.(CIESIN), Columbia Univ*.

Wynsberghe, Aimee van. 2021. "Sustainable AI: AI for Sustainability and the Sustainability of AI." *AI and Ethics* 1 (3): 213–218. https://doi.org/10.1007/s43681-021-00043-6.

Xu, Yong, Yimeng Song, Jixuan Cai, and Hong Zhu. 2021. "Population Mapping in China with Tencent Social User and Remote Sensing Data." *Applied Geography* 130 (May): 102450. https://doi.org/10.1016/j.apgeog.2021.102450.

Zanaga, Daniele, Ruben Van De Kerchove, Dirk Daems, Wanda De Keersmaecker, Carsten Brockmann, Grit Kirches, Jan Wevers, et al. 2022. "ESA WorldCover 10 m 2021 V200." Zenodo. https://doi.org/10.5281/ZENODO.7254221.

Zanaga, Daniele, Ruben Van De Kerchove, Wanda De Keersmaecker, Niels Souverijns, Carsten Brockmann, Ralf Quast, Jan Wevers, et al. 2021. "ESA WorldCover 10 m 2020 V100." Zenodo. https://doi.org/10.5281/ZENODO.5571935.

Zhang, Xiao, Liangyun Liu, Tingting Zhao, Yuan Gao, Xidong Chen, and Jun Mi. 2022. "GISD30: Global 30 m Impervious-Surface Dynamic Dataset from 1985 to 2020 Using Time-Series Landsat Imagery on the Google Earth Engine Platform." *Earth System Science Data* 14 (4): 1831–1856.

Zhou, Yuyu, Xuecao Li, Wei Chen, Lin Meng, Qiusheng Wu, Peng Gong, and Karen C. Seto. 2022. "Satellite Mapping of Urban Built-up Heights Reveals Extreme Infrastructure Gaps and Inequalities in the Global South." *Proceedings of the National Academy of Sciences* 119 (46): e2214813119. https://doi.org/10.1073/pnas.2214813119.